Dissertation
submitted to the
Combined Faculty of Natural Sciences and Mathematics
of Heidelberg University, Germany
for the degree of
Doctor of Natural Sciences

Put forward by
Matteo Mazzarini
born in: Jesi, Italy
Oral examination: 4 November 2020

A numerical investigation of the Milky Way and of the satellite tidal debris in the Galactic environment

Referees:

apl. Prof. Dr. Andreas Just

Priv.-Doz. Dr. Andreas Koch

Zusammenfassung

Ich befasse mich mit der Verteilung von Satellitengalaxien-Überresten in der Milchstraßen-Umgebung mit Hilfe von N-body-Simulationen durch die Kombinierung vollständiger N-body-Milchstraßen-Modelle mit realistischen, hochauflösenden N-body-Satelliten und kosmologisch motivierten Anfangsbedingungen. Für die Wahl des Codes führe ich einen Benchmark-Test für frühere N-body-Simulationen der Milchstraßen-Umgebung durch, um zu beweisen, dass GADGET-2 mit moderneren Codes vergleichbar ist, sowie, dass GADGET-4 eine verbesserte Impulserhaltung gegenüber GADGET-2 bietet. Anschließend simuliere ich mit GADGET-4 die Verteilung von Satelliten-Überresten in der Milchstraßen-Umgebung. Sterne werden weniger effizient aus den Satelliten herausgerissen als Dunkle Materie (DM), und es finden sich größere Anteile stellarer Überreste in den Milchstraßen-Zentralregionen, wo stellare und DM-Überreste unterschiedliche Ausrichtungen haben und sie nicht signifikant ändern, wenn die Scheibe der Milchstraße anfänglich gekippt ist. Daraus schließe ich, dass die Anfangsbedingungen für die Satelliten mehr Einfluss auf die Ausrichtung der lokalen Überreste haben als die Scheibe, und dass die DM- und stellaren Überreste räumlich nicht korreliert sind. Zum Schluss präsentiere ich eine Untersuchung des Balkens in einem N-body-Milchstraßen-Model, das den Beobachtungsbedingungen unserer Galaxie entspricht. Der in dieser Simulation gebildete starke Balken ist ein langsamer Rotator, der die Kinematik und Dynamik der lokalen Scheibe beeinflusst und keine signifikante Wölbung aufweist.

Summary

I address the satellite debris distribution in the Milky Way (MW) environment by means of N-body simulations, combining full N-body MW models with realistic high-resolution N-body satellites and cosmologically motivated initial conditions. For the choice of the code, I perform a benchmark on previous N-body simulations of the MW environment, proving that GADGET-2 performs similar to more modern codes, and that GADGET-4 offers an improved momentum conservation compared to GADGET-2. Then, with GADGET-4 I simulate the satellite debris distribution in the MW environment. Stars are stripped less efficiently than dark matter (DM) from the satellites and larger fractions of stellar debris are found in the MW central regions, where the stellar and DM debris have different orientations and do not change them significantly if the MW disc is initially tilted. I conclude that the satellite initial conditions have more impact than the disc on the local debris orientation, and that the DM and stellar debris are spatially uncorrelated. Finally, I present a study of the bar in an N-body MW model that matches the observational constraints of the Galaxy. The strong bar formed in this simulation is a slow rotator that influences the local disc kinematics and dynamics and does not present significant buckling.

Contents

Chapter 1

Introduction: the Milky Way and the satellite streams in a cosmological context

1.1 Milky Way Galaxy: history of observations

The **Milky Way Galaxy** (hereafter MW), also referred to as *the Galaxy*, is the large system of stars and gas that hosts the Solar system and our planet, the Earth.

Observations of the MW and discussions around its nature are dated old in our history. Already in the IV century B.C., in his work *Meteorologica*, Aristotle (384 B.C. - 323 B.C.) reported the theory of Democritus (c.a. 460 B.C. - c.a. 370 B.C.) and Anaxagoras (c.a. 500 B.C. - c.a. 428 B.C.): they interpreted the MW as a collection of stars, visible from the Earth in the night sky. Aristotle himself was against this theory. Based on geometrical considerations about the shadow of the Earth projected on these stars, he claimed that they would not be otherwise always visible at the same position as they were, because of the Earth shadowing different regions of the sky from the Sun, during the orbital revolution of the Sun in a year. Let us remember that at that time the Earth was thought to be at the centre of the Universe, and the Sun was thought to revolve around it. In the Middle Ages, the position of many Middle Eastern astronomers and scientists, like Ibn Qayyim Al-Jawziyya (1292 - 1350), took distance from the theory of Aristotle. They stated in fact that the MW is composed of stars.

A huge conceptual step forward regarding the understanding of the local Universe (and of the MW) has been done in the XVI-XVII centuries with some milestone works in modern astronomy and physics. The works *De Revolutionibus Orbium Coelestium* by Nicolaus Copernicus (1473 - 1543), *Astronomia Nova* and *Harmonices Mundi* by Johannes Kepler (1571 - 1630) and *Philosophiae Naturalis Principia Mathematica* by Isaac Newton (1643 - 1727) were fundamental to 1) falsify the previous Aristotelian geocentric view of the Universe, in favour

of a model with the Sun at the centre; 2) provide geometrical evidence for the orbital empirical laws of the planets around the Sun; 3) provide a Universal law of gravitation by which we can describe the mutual attraction of astronomical objects in the Universe.

Regarding the MW, the work of Galileo Galilei (1564 - 1642), the *Sidereus Nuncius*, inlcudes one of the first modern scientific, observational evidences for stars composing the MW. Galilei made observations of these stars using the first lenses and telescopes available at his epoch. In prosecution with this, Frederick William Herschel (1738 - 1822) made a significant step forward: by means of stellar counts in the MW he reconstructed the shape of the Galaxy as a disc-like or flattened structure made of stars. He assumed however the Sun to be at the centre of the MW disc (see the Figure 4 in the original work of Herschel 1785).

Later, Kapteyn (1922) measured the positions of the stars in the MW and re-defined the location of the Sun with respect to the Galactic Centre (GC), placing it not anymore in the GC itself, but with some offset. However, the estimated distance, or Galactocentric distance (GCd), was still much lower ($\sim 2\,\mathrm{kpc}$) than the currently estimated one (see Section 1.2.1 below).

Until the early 1900s it was commonly assumed that the MW was enclosing all the stars of the once though-to-be Universe. The measurements of the redshifts of astronomical objects by Slipher (1913), the better definition of the distance of objects like the once called "Andromeda nebula" (today known to be another, nearby galaxy, the Andromeda galaxy, or M31 according to Messier Catalogue, see Hubble 1929b; Curtis 1917) and the discovery of the expansion of the Universe (Friedmann 1922; Lemaître 1927; Hubble 1929a) helped understanding that the MW is a separate galaxy among many others in the whole Universe.

1.1.1 Goal of the thesis and structure of this chapter

The main goal of this thesis is to describe, by means of numerical simulations, the distribution of the tidal debris of the satellite galaxies of the MW in its environment. Therefore, in this introductory chapter, I present a review of what is understood about our Galaxy and its satellite galaxies, also in the light of modern cosmology.

First, I review the current understanding of the MW stellar disc, of its stellar bulge, its dark matter (DM) halo and its satellite galaxies. In fact, these are all the MW components and objects that I employed in the N-body simulations presented in this thesis.

After that, I review the cosmological theoretical framework by means of which the MW and its satellite galaxies can be understood. Specifically, I give a summary of the main equations that describe the evolution of the Universe and I focus additionally on the formation of structures like the MW and its satellites.

Subsequently, I adapt the introductory section of my first author publication, in which I describe the state-of-the-art knowledge of the tidal streams of the MW satellites. I then introduce the main research goal of this thesis, i.e. the

numerical study on the distribution of the satellite debris in our Galaxy.

Last, I present the current understanding of the MW bar, as the starting point for an additional collaborative research on bar formation and evolution in a MW high-resolution N-body simulation. This additional research is intended to give more details about some aspects of the dynamics of our Galaxy (in this case, the formation and evolution of a strong bar in its centre), and to provide a new N-body MW set-up, that is competitive both in terms of faithfulness to the observations of the Galaxy and in terms of numerical resolution.

1.2 Milky Way: current understanding

The current picture of the MW describes it as a disc-like structure made of stars that rotate around the GC. Other components of the MW include a central concentration of stars, called classically *stellar bulge* due to its spheroidal shape, and a halo made of stars and of an additional component, the cold DM (CDM). To date, the DM component has not been observed. As I will show later in this section, its dynamical effects on the other MW components are proved by extended literature. However, we have not detected any DM particle candidate yet. A recent, detailed review on the observational properties of the MW is given in Bland-Hawthorn & Gerhard (2016, hereafter **BHG16**). Additionally, the MW is surrounded by a number of satellite galaxies.

For the sake of simplification, the three main MW components that I am going to describe are its disc (made of stars, gas and dust), its stellar bulge, and its DM halo. This simplification matches the N-body realisations of the MW models that I employed in this thesis [1].

1.2.1 Galactic disc

Observationally speaking, the MW disc is a peculiar case of galactic disc, since we can observe it from inside it and we can study in detail its gaseous components, such as the neutral hydrogen HI (Kalberla & Kerp 2009, for a review), a large multitude of its stars - for instance Rix & Bovy (2013), but also the recent large catalogue of stellar positions, proper motions and radial velocities from the Gaia Data Release 2 (hereafter DR2), as in Gaia Collaboration et al. (2018) - and the interstellar dust (Draine 2003, for a review). The release of the Gaia DR2 has provided positional and projected kinematic information for more than 1 billion stars of the MW and radial velocity spectroscopic information for ~ 7 million stars, allowing a larger understanding of our Galaxy.

---

[1]As pointed out by **BHG16**, it is unlikely that bulge, disc and stellar halo are completely separated components, in the sense that it is not possible to clearly distinguish where a component begins and another ends. Also, well-defined, individual components can strongly overlap, because of the common underlying gravitational potential and of stellar mixing mechanisms, posing questions to their distinction (see **BHG16** and references therein). However, the simplification adopted here eases the study of the MW via numerical simulations.

General properties of the thick disc and of the thin disc

The MW disc consists of two components, the *thick disc* and the *thin disc*, with a thick disc mass $M_{\text{thick}} = (6 \pm 3) \times 10^9$ M$_\odot$ and a thin disc mass $M_{\text{thin}} = (3.5 \pm 1) \times 10^{10}$ M$_\odot$, therefore the thick disc mass is one fifth of the thin disc mass (**BHG16**). The thin and the thick disc are typically modelled as density exponential profiles, as in Gilmore & Reid (1983). Combining the results of Gilmore & Reid (1983) with the ones of Freeman (1970), the density profile that describes the mass distribution of the thin and thick disc can be written in the form

$$\rho(R, z) = \rho(z = 0, R = 0) \times \exp\left(-\frac{R}{h}\right) \times \text{sech}^{2P}\left(\frac{z}{z_0}\right), \qquad (1.1)$$

where h is the disc scale length, z_0 is the disc scale height, and where P is the ratio between the mean square velocity dispersion values of the disc and of the sampled populations (Gilmore & Reid 1983). For a sampled population uniquely identified with the thin or thick disc, then $P = 1$. An application of this is shown for instance in Moetazedian & Just (2016, hereafter **MJ16**), where they adopted $P = 1$ for the thin disc in their MW N-body models.

The best values of the thin and thick disc scale height and scale length are set to $z_{0,\text{thin}} = 0.3$ kpc and $h_{\text{thin}} = 2.6$ kpc for the thin disc scale height and scale length, respectively, and $z_{0,\text{thick}} = 0.9$ kpc and $h_{\text{thick}} = 3.6$ kpc for the thick disc scale height and scale length, respectively (Jurić et al. 2008, **BHG16**). As a matter of simplification, in the simulations that I am going to discuss and study in this thesis the less massive thick disc is ignored, and all the models start with an initially thin and cold disc only (i.e. a disc where the stars are distributed with an initially small vertical scale height and with an initially small vertical velocity dispersion).

Rotation curve

That galactic discs have rotational properties in other galaxies than the MW is a fact known since many decades ago (Rubin & Ford 1970; Rubin et al. 1980). For the specific case of our Galaxy, already Oort (1927) could determine the constants describing the rotational properties of the MW disc in the Sun neighbourhood (a more recent determination of the Oort's constants can be found in Bovy 2017).

The rotation of the disc can be physically interpreted in terms of dynamical support by the mass enclosed within each (projected or physical) radius R, at which the circular velocity curve $V_{\text{circ}}(R)$ is reconstructed from the observed redshifts. For a given galaxy, the total matter that contributes to the rotation of any test particle in the disc is the sum of all the components enclosed within the GCd R of the particle, as

$$V_{\text{circ}}(R) = \sqrt{G\frac{M(<R)}{R}}, \qquad (1.2)$$

under the simplifying assumption of spherical distribution of the mass M enclosed within radius R. Here, $G = 6.678 \times 10^{-11}$ m^3 s^{-2} kg^{-1} is the universal constant of gravitation.

The contribution of Rubin et al. (1980) was discovering that the rotation curve of the disc galaxies is flat at large GCds. This is not expected if only the visible matter (stars and gas inside the disc and the bulge) were dynamically sustaining the rotation curve. This means that there is an additional term of mass sustaining the rotation of gas and stars in the disc, since the disc, bulge, bar and stellar halo alone would not be enough to interpret the observed rotation in terms of Equation (1.2).

Regarding the estimates of the circular velocity, using information collected from literature, **BHG16** reported a circular velocity $V_{\mathrm{circ}} = (238 \pm 15)$ km s^{-1} at the GC distance R_0 of the Sun. This is compatible with other results from previous and subsequent literature.

By applying the tangent point method on observed sources of HI (Burton & Gordon 1978) and CO molecules in the MW, one can fit a rotation curve model to these data and determine the rotation curve close to the Sun (Mróz et al. 2019, and references therein). Using data from 773 classical cepheids, Mróz et al. (2019) found that, at their assumed distance of the Sun $R_0 = (8.122 \pm 0.031)$ kpc from the GC (being this the result of GRAVITY Collaboration et al. 2018), the rotation curve has a value $V_{\mathrm{circ}} = (233.6 \pm 2.8)$ km s^{-1}. From the phase-space data of more than 23000 luminous red giant stars, Eilers et al. (2019) could fit a rotational model to the MW disc where the circular velocity at the Sun's position is $V_{\mathrm{circ}} = (229.0 \pm 0.2)$ km s^{-1}. They reported however a systematic uncertainty at $\sim 2 - 5\%$ level, that they mostly attributed to the lack of knowledge of the density profile related to the distribution of the sampled population of stars.

Regarding the shape of the curve, always Eilers et al. (2019) found that the MW rotation curve external to the Sun and until 25 kpc of GCd decreases very slowly, with a corresponding gradient (-1.7 ± 0.1) km s^{-1} kpc^{-1}, and even if there is a systematic uncertainty of 0.46 km s^{-1} kpc^{-1} in their result, they stated that this uncertainty is not enough to eliminate the measured decrease of the rotation curve. The presence of a negative gradient in V_{circ} was found also in Mróz et al. (2019), that quantified it to be (-1.34 ± 0.21) km s^{-1} kpc^{-1} in the GCd range 4 kpc $< R < 20$ kpc.

From the analysis of the rotation curve it is possible to gain more information about the structures that compose the Galactic disc. Sofue et al. (2009) collected data from previous, extended literature on the rotation of different tracers in the disc. They rescaled these values to the solar values $(R_0, V_0) = (8$ kpc, 200 km s^{-1}). They fitted the obtained velocity data with a rotation curve model coming from the contribution of an exponential disc (included ring-like structures, spiral arms and bar), a bulge and a semi-isothermal DM halo (Kent 1986). They reported a dip in the curve at 3 kpc GCd and a dip at 9 kpc GCd, slightly outside the GCd of the Sun. Since they took into consideration the contribution of the mass distribution of the Galactic bar, the spiral arms and the rings, they were able to explain the dip at 3 kpc as due to the inner Galactic bar,

and the dip at 9 kpc as due to an external ring at 11 kpc, that they suggested may be associated with the Perseus spiral arm.

Therefore, the emerging picture is that the rotation curve of the MW is almost flat for a wide range of GCds enclosing the position of the Sun, and that the dips present in it at different GCds reveal the disc substructure and the local inhomogeneities in the disc density distribution, like for instance the spiral arms. The almost flat profile of the rotation curve, combined with its value at the GCd of the Sun of ~ 230 km s^{-1}, reinforces the evidence of an underlying DM halo, with a virial mass $M_{200} = (1.1 \pm 0.3) \times 10^{12}$ M$_\odot$ (**BHG16**), sustaining the rotation of the disc. For the definition of virial mass, see Section 1.2.3.

Distance of the Sun from the Galactic centre

The current knowledge of the distance of the Sun from the GC comes from a number of observational approaches (Gillessen et al. 2013). The value adopted by **BHG16** in their review of the MW is $R_0 = (8.2 \pm 0.1)$ kpc. More recent studies set it to $R_0 = (8.0 \pm 0.3)$ kpc (Camarillo et al. 2018), or $R_0 = (8.1 \pm 0.2)$ kpc (Griv et al. 2019). The current best estimate of R_0 is given by The GRAVITY Collaboration et al. (2019). They combined astrometric techniques (recently supported by the implementation of the interferometric instrument GRAVITY) with spectroscopic techniques, to follow the star S2, that orbits around the supermassive black hole Sgr A* placed at the centre of the MW. They estimated that $R_0 = (8.178 \pm 0.013_{\text{stat.}} \pm 0.022_{\text{sys.}})$ kpc, a very high precision measurement, considering the corresponding low errors. Here, the subscripts "stat." and "sys." indicate the statistical and systematic uncertainty, respectively.

In the context of this thesis, the simulations discussed in Chapter 2 and in Chapter 3 are performed with MW models where **MJ16** assumed $R_0 = 8.0$ kpc. In Chapter 4 the value assumed in the MW model by D'Onghia & Aguerri (2020) is $R_0 = 8.1$ kpc. Both values are generally aligned with the recent estimates of R_0. However, the value of D'Onghia & Aguerri (2020) is the closest of the two to the best estimate of The GRAVITY Collaboration et al. (2019), and in this sense it is an improvement from the value of **MJ16**.

1.2.2   Galactic bulge

The bulge is usually described as a spheroid made of stars, that occupies the central region of a disc galaxy. As for the kinematics, from surveys like BRAVA (Bulge Radial Velocity Assay, Rich et al. 2007), Kunder et al. (2012) found that the bulge is centrally dominated by random motions, with a corresponding velocity dispersion of up to ~ 120 km s^{-1}, but it shows also a residual mean rotational velocity profile that goes up to ~ 75 km s^{-1} at a Galactic longitude $l \sim 4^{\text{o}}$.

There are two ways of describing the MW bulge (and the bulges in disc galaxies). The first way is the *classical bulge* picture and the second way is the *pseudo-bulge* picture.

According to the classical bulge picture, the Galactic bulge is formed in the centre of the MW, as a result of the merger of the MW with its satellite galax-

ies (**BHG16**). Since stellar populations in the bulge are much older ($10 - 12$ Gyr) than the ones of the disc, then according to the classical bulge picture, the bulge, together with the thick disc, should have been formed by the contribution of one of the last minor mergers experienced by the MW, unless the disc contains old stellar populations in its very inner regions (Wyse 2009). Among the other factors that may have contributed to the subsequent bulge build-up there can be gas-inflows to the centre of the MW after a merger with a smaller galaxy, when gas can lose angular momentum and end in the central regions of the host Galactic disc (Mihos & Hernquist 1996). A summary of the definition of classical bulges is provided by Kormendy & Ho (2013), according to which classical bulges reproduce the observational features of the elliptical galaxies, and particularly have half-light radius r_e, surface brightness at r_e, μ_e, and logarithm of the central velocity dispersion $\log(\sigma)$ that lie in the fundamental plane of elliptical galaxies (for the fundamental plane, see Djorgovski & Davis 1987).

In the pseudo-bulge picture, instead, it is by means of slow, secular processes internal to the MW (and to disc galaxies in general) that matter redistributes forming the bulge in the centre of the disc (Kormendy & Ho 2013). A distinctive feature of the pseudo-bulge is the bimodal distribution of its tracers, such as the red-clump giant stars, which gives it the configuration of an X-shape or a boxy/peanut (B/P) shape (Portail et al. 2015a, hereafter **P15**). As pointed out in **BHG16**, recent works from McWilliam & Zoccali (2010), Nataf et al. (2010) and Wegg & Gerhard (2013b) showed that the MW bulge may be considered more like a component of the MW bar. In this sense, the pseudo-bulge may be connected somehow to the formation of the Galactic bar. **BHG16** concluded that in the MW the evidence points towards most of its bulge being built-up as a pseudo-bulge via disc instabilities and secular evolution, while the classical bulge component must have been very small (originally less than 8% of the current bulge mass), if ever built.

From the density distribution of red clump giants and from the stellar kinematic data of Kunder et al. (2012), **P15** applied different MW N-body models inclusive of a DM halo and of a barred disc, to infer the value of the B/P bulge dynamical mass (stars plus DM) sustaining the observed kinematics. They found a value $M_{\rm b,dyn} = (1.84 \pm 0.07) \times 10^{10} \ M_\odot$. Calculating the mass-to-light and mass-to-clump ratios in their models and comparing them against different stellar population synthesis models, they found a total stellar B/P bulge mass $M_{\rm b,star} = (1.25 - 1.6) \times 10^{10} \ M_\odot$.

Therefore, considering all these recent advancements in the study of the Galactic bulge, this one appears to be a structure formed for most part as a consequence of the secular evolution of the Galactic bar, and with a characteristic B/P shape. The classic component of the bulge is currently expected to be subdominant in terms of mass, and the total bulge mass (pseudo-bulge together with classical bulge) is around $\sim 1.7 - 1.8 \times 10^{10} \ M_\odot$, smaller than the disc mass reported in Section 1.2.1.

1.2.3 Galactic halo

With MW halo we can refer to two possible components: the stellar halo and the DM halo. Since in our simulations only the DM halo is included, and since the stellar halo represents a small fraction of the total stellar mass, with $M_{\mathrm{halo},*} = (1.4 \pm 0.4) \times 10^9$ M$_\odot$ (Deason et al. 2019), I am going to introduce the DM halo only, because of its employment in building and setting up stable MW N-body models.

Dark matter halo

Current modelling of the MW includes a spheroidal halo, made of DM and spatially distributed with a triaxial shape (**MJ16**, Allgood et al. 2006, for instance)[2]. Assuming the presence of a DM halo in our Galaxy is important for several reasons.

First, as explained later in Section 1.3, according to the current standard cosmological model 84% of matter in our Universe is in the form of DM, while baryonic matter (the same form of matter that stars, planets, gas and interstellar dust are made of) represents only its 16%, with a ratio between DM content and baryonic matter content of ~ 5.38 in favour of DM. Therefore, if this is true, it is highly expected that DM is present as the dominant mass component of the MW, in the form of a spheroidal halo according to the current galaxy formation models.

Second, DM is required for dynamical equilibrium reasons, in order to explain the rotation curve of the MW disc. As I showed in Section 1.2.1, the MW disc has a flat rotation curve on GCds larger than few kpc. The disc stellar and gaseous components alone are not massive enough to sustain such flat rotation, that is otherwise expected to decay at large GCds R on the disc with a Keplerian fashion $R^{-1/2}$. The presence of a DM halo dynamically sustaining the disc would allow it to rotate at larger radii with support from the DM mass. In fact, following and expanding Equation (1.2), the circular velocity at GCd R on the disc can be described in terms of the underlying disc, bulge, and halo integrated masses as

$$V_{\mathrm{circ}}(R) = \sqrt{\frac{G(M_{\mathrm{b}}(<R) + M_{\mathrm{d}}(<R) + M_{\mathrm{h}}(<R))}{R}} \qquad (1.3)$$

where $M_{\mathrm{b}}(R)$, $M_{\mathrm{d}}(R)$ and $M_{\mathrm{h}}(R)$ are the bulge, disc and halo mass enclosed within GC distance R, respectively.

Third, always within the predictions of the standard cosmological model, the formation of galaxies like the MW happens via a first gravitational collapse of DM into spheroidal, triaxial haloes, followed by the subsequent collapse of gas into the gravitational wells created by these DM haloes. If DM in the MW exists, it should be in the form of a spheroidal structure that surrounds our Galaxy. For the formation of structures in the Universe, see Section 1.3.2.

---

[2]For the sake of simplicity, the MW models described in this thesis adopt a spherical DM halo. See again **MJ16**, for example.

Currently, the missing piece of information about DM is the discovery of a fundamental particle for DM. Since addressing the properties of DM at fundamental physics level goes far beyond the scope and topic of this thesis, I refer the reader to Feng (2010) for a review on DM particle candidates.

Hernquist and Navarro-Frenk-White density and mass profiles

Among the density profiles employed in modelling the MW DM halo, I will mention the two types that have been employed to build the numerical MW models that I used in my simulations. These are the *Hernquist* and *Navarro-Frenk-White* (NFW) halo models.

The Hernquist halo (Hernquist 1990) has a density profile in the form

$$\rho_{\mathrm{H}}(r) = \frac{M}{2\pi a^3}\left(\frac{r}{a}\right)^{-1}\left(1 + \frac{r}{a}\right)^{-3}, \qquad (1.4)$$

and has a finite total mass represented by M. The density profile is cuspy in the centre, with an r^{-1} dependence on the radius. This profile was introduced to approximate the density profiles of elliptical galaxies, but can be applied to bulges as well and has the advantage of allowing a halo distribution function (DF) that is dependent only on energy and is independent on direction (Yurin & Springel 2014). The corresponding, cumulative mass profile is

$$M_{\mathrm{H}}(r) = M\left(\frac{r}{a}\right)^2\left(1 + \frac{r}{a}\right)^{-2}. \qquad (1.5)$$

For large r, the cumulative mass tends to M.

The NFW (Navarro et al. 1995b) density profile comes empirically from density fits to DM haloes in DM-only cosmological simulations of structure formation and evolution. It has the form

$$\rho_{\mathrm{NFW}}(r) = \rho_0\left(\frac{r}{r_{\mathrm{s}}}\right)^{-1}\left(1 + \frac{r}{r_{\mathrm{s}}}\right)^{-2}, \qquad (1.6)$$

where r_{s} is the scale radius. The advantage of the NFW model is, as said, the good fit of its density profile to DM haloes in cosmological simulations at a wide range of scales (Navarro et al. 1996). The mass density has the same inner cusp as in the Hernquist profile, proportional to r^{-1}. The cumulative mass of this model is obtained as

$$M_{\mathrm{NFW}}(r) = 4\pi\rho_{\mathrm{s}}r_{\mathrm{s}}^3\left[\ln\left(1 + r/r_{\mathrm{s}}\right) - \frac{r/r_{\mathrm{s}}}{1 + r/r_{\mathrm{s}}}\right], \qquad (1.7)$$

and it diverges logarithmically to infinite. A way to avoid this divergence is to truncate the integrated mass to the value of virial mass M_{200}, i.e. the cumulative mass within the virial radius r_{200}, which is the radius at which the enclosed average mass density is ~ 200 times above the critical cosmological density (for the critical cosmological density, see Section 1.3.1), as defined in Navarro et al.

(1995a). The simplification here is again that the halo is treated as spherical and not triaxial, and therefore the value of M_{200} represents an underestimation of the actual virial mass M_{vir}, i.e. the mass of the virialised host galactic halo, and this underestimation is around 16% its value (**BHG16** and references therein). However, for the case of the MW **BHG16** reported an actual virial mass $M_{\mathrm{vir}} = (1.3 \pm 0.3) \times 10^{12}$ M$_\odot$, that, considering the uncertainties, is compatible with the value $M_{200} = (1.1 \pm 0.3 \times 10^{12})$ M$_\odot$, and the approximation of using M_{200} is anyway consistent with the usage of spherical haloes truncated at r_{200} for the MW models presented in this thesis.

It is possible to obtain a Hernquist profile that approximates the corresponding NFW profile reasonably well. In fact, by imposing $M = M_{200}$ from Equation (1.4), and defining the NFW halo concentration parameter $c \equiv r_{200}/r_{\mathrm{s}}$, then for the best-matching Hernquist profile the scale radius a is given by

$$a = r_s \sqrt{2(\ln(1 + c) - c/(1 + c))}. \tag{1.8}$$

More details on this procedure can be found in (Springel et al. 2005a).

1.2.4 Milky Way satellites

The MW is surrounded by a number of satellite galaxies. As I will recall in Section 1.3.2, these satellites are explained as the observable remnants of smaller mass (dwarf) galaxies that have been continuously falling, orbiting and merging into the MW environment after its buildup (Newton et al. 2018). Nowadays, there is a vast literature of observations of these galaxies, and the improvement of the observational techniques helps unveil even fainter satellites of the MW.

Census of the Milky Way satellites

Two of the most notorious and closest satellites are the Small Magellanic Cloud and the Large Magellanic Cloud (hereafter SMC and LMC, respectively), distant ~ 62 kpc and ~ 50 kpc from the Sun, respectively (Pietrzyński et al. 2013; Graczyk et al. 2014). The first documented observation of the LMC is dated X Century, when the Persian astronomer 'Abd al-Rahman al-Sufi (903 - 986) reported the observations done on this object in his work, the *Book of Fixed Stars*.

In the last century, the understanding of the nature of the MW and of the other "nebulae" as individual galaxies has helped understanding the satellite galaxies of the MW as well. McConnachie (2012) counted up to ~ 30 satellite galaxies in the MW environment. Extending the count to the entire Local Group (LG), including the field dwarf galaxies and the satellite galaxies of M31, then the total count reached ~ 100 objects. For the MW, the census has been increased further by subsequent discoveries of faint substructures like the pair Carina II and III in the proximity of the Magellanic Clouds (Torrealba et al. 2018), with inferred DM masses as small as $\sim 10^6$ M$_\odot$ (Li et al. 2018), or also the discovery of the more massive, diffuse dwarf galaxy Crater 2 (Torrealba et al. 2016). Torrealba et al. found that Crater 2 has a half-light radius of 1.1

kpc, and therefore it is the fourth largest MW satellite after the LMC, the SMC and the Sagittarius (Sgr) dwarf.

To date, a total of ~ 60 satellite galaxies of the MW have been discovered and confirmed, and a boost to their discovery has come from digital surveys (Simon 2019). Using the combined census of satellites from the SDSS (Sloan Digital Sky Survey, with the Data Release 9, Ahn et al. 2012) and the DES (Dark Energy Survey, Bechtol et al. 2015; Drlica-Wagner et al. 2015) surveys, Newton et al. (2018) applied a Bayesian inference method starting from the Aquarius (Aq) cosmological simulations of Springel et al. (2008) and extrapolated the luminosity function (LF) of the MW satellites within 300 kpc from the MW GC, reaching a total estimated number of 124^{+40}_{-27} satellites, with the higher absolute magnitude in V band being $M_V = -9$, and with a lower magnitude cut at $M_V = 0$, this corresponding to the faintest dwarf galaxies.

Missing satellites problem

One of the most important challenges of the ΛCDM model was to explain why DM-only cosmological simulations predict a number of substructures (i.e. the underlying haloes of the MW satellites counterparts) higher than the actual number of satellites observed around the MW (Klypin et al. 1999). The problem is called *missing satellites problem*. Specifically, the prediction that many massive DM subhaloes do not have massive observed satellite counterparts (with stellar luminosity $L > 10^5$ L$_\odot$) is known as the *too big to fail* problem (Boylan-Kolchin et al. 2011).

These problems are claimed to be solvable if one takes baryonic physics and baryons-involving processes (e.g. photoionisation, tidal stripping and disruption, supernova feedback) into account in the numerical recipes used to simulate the formation of structures in the Universe (Bullock et al. 2000; Macciò et al. 2010; Tomozeiu et al. 2016). The presence of baryonic physics redistributes baryons in the galactic environment, having an effect on the gravitational potential and on the distribution of the DM, with consequences on the entire evolution of the satellite galaxies. As an example of this, following the approach of Zolotov et al. (2012), Brooks et al. (2013) found that supernova feedback and tidal stripping in dwarf galaxies have the effect of reducing the number of star forming massive satellite galaxies to a number compatible with the ones observed around the MW.

1.3 Lambda cold dark matter cosmology as a framework for the Milky Way and its satellite galaxies

1.3.1 Lambda cold dark matter model

The main goal of this thesis is addressing the distribution of the satellite tidal debris in the MW environment by means of numerical simulations. This requires a cosmological framework in which to extract the information about the MW halo properties and the distribution of the MW satellites around it (**MJ16,**

Springel et al. 2008), as well as recipes to describe the dwarf galaxies employed to study their debris (Macciò et al. 2017, hereafter **M17**): the context of this study is an extension of the modern standard cosmology to the local MW environment. Therefore, I am going to review the main concepts of cosmology that represent the context in which I carried my study.

The general cosmological framework in which we describe the formation of galaxies like the MW and its satellites is the Lambda cold dark matter model, or ΛCDM model (Hinshaw et al. 2013; Planck Collaboration et al. 2018). According to the ΛCDM model, the space-time metrics of the Universe obeys to Einstein's general relativity by means of the field equations (Einstein 1915). In this context, the Universe has expanded from an initial time t_0, corresponding to the Big Bang singularity (Penzias & Wilson 1965; Dicke et al. 1965). The expansion is currently accelerated because of the so-called *dark energy* (DE), with acceleration measurable on scales larger than 1000 Mpc (Riess et al. 1998; Perlmutter et al. 1999; Cervantes-Cota & Smoot 2011).

The classic Big Bang model has been modified by means of an inflationary model. In fact, there is need for an *inflation* process after the Big Bang, in order to expand the Universe from a microscopic scale to its current scale, and in order to the explain the currently measured values of the cosmological parameters, the isotropy of the Cosmic Microwave Background (CMB) radiation (see below) and the flatness of the Universe (for an overview of the Modern Cosmology, including the inflationary theory, see for instance Liddle 2003).

The field equations are expressed for a four-dimensional space-time (three space coordinates and one time coordinate). They are a system of differential tensorial equations in the form

$$R_{\mu\nu} - \frac{1}{2}Rg_{\mu\nu} - \Lambda g_{\mu\nu} = \frac{8\pi G}{c^4}T_{\mu\nu} \,, \tag{1.9}$$

where μ and ν are tensorial indexes, $R_{\mu\nu}$ is the Riemann tensor, R is the Ricci scalar, $g_{\mu\nu}$ is the metric tensor, $\Lambda = 1.09 \times 10^{-56}$ cm^{-2} [3] is the cosmological constant (associated with a negative energy density term, and therefore connected with the DE), and $T_{\mu\nu}$ is the energy-impulse tensor. As a note, the sign in front of Λ is subject to the different sign conventions employed when describing Equation (1.9) (see the Table of sign conventions of Misner et al. 1973). The field equations connect the derivatives of the metrics to the energy-matter content of the Universe.

The Universe is observed to be homogeneous and isotropic on large scales (Yadav et al. 2010; Saadeh et al. 2016; Planck Collaboration et al. 2018). In this perspective, one can adopt the Robertson-Walker metrics with space-time interval

$$ds^2 = -c^2dt^2 + a(t)^2\Big[\frac{dr^2}{1 - kr^2} + r^2d\omega^2\Big] \,, \tag{1.10}$$

where $c = 2.997 \times 10^5$ km s^{-1} is the light speed for vacuum, $d\omega^2 = d\theta^2 + \sin^2\theta d\phi^2$

---

[3]For the values of the cosmological constants and parameters employed in this chapter, see http://pdg.lbl.gov/2019/reviews/rpp2018-rev-astrophysical-constants.pdf.

is the solid angle in polar coordinates (θ, ϕ), and k is the curvature of the Universe (Robertson 1927; Liddle 2003). $a(t)$ is the scale factor of the Universe, and it is a function of the cosmic time. At our epoch, which corresponds to the current age of the Universe, $t_0 = 13.799$ Gyr and $a(t_0) = 1$[4]. The dynamical evolution of the Universe is then obtained by combining Equations (1.9) and (1.10) into the Friedmann equations (Friedmann 1922; Liddle 2003),

$$\begin{cases} \frac{\dot{a}^2 + kc^2}{a^2} = \frac{8\pi G\rho + \Lambda c^2}{3} \\ \frac{\ddot{a}}{a} = -\frac{4\pi G}{3}\left(\rho + \frac{3p}{c^2}\right) + \frac{\Lambda c^2}{3}\,. \end{cases} \tag{1.11}$$

In these last equations, ρ expresses the matter density, while p is the pressure term associated with radiation (and hence $3p/c^2$ is the corresponding density term). Another fundamental quantity is $H \equiv \dot{a}/a$ and it is called Hubble expansion rate.

The redshift z is related to $a(t)$ by

$$z = 1/a(t) - 1 \equiv z(t)\,. \tag{1.12}$$

For t approaching the epoch of the Big Bang $(t_{BB} = 0)$, then $z \to \infty$ and $a \to 0$. In our epoch $(t = t_0)$, $z = 0$ and $a = 1$. I also introduce two different types of coordinate frames adopted in Cosmology: the first is the comoving coordinate frame, the second is the physical coordinate frame. The relation between physical coordinates $\vec{r}$ and comoving coordinates $\vec{x}$ is

$$\vec{r} = a(t)\vec{x}\,. \tag{1.13}$$

The relative position of two points will remain the same in comoving coordinates, not depending on the Universe expansion. The scale factor provides the conversion to physical coordinates at any time t.

The Universe consists of different components. For each j-th component, the corresponding density parameter Ω_j is given by

$$\Omega_j = \rho_j/\rho_{\mathrm{crit}}\,, \tag{1.14}$$

with ρ_j being the volume density of the j-th component. Here,

$$\rho_{\mathrm{crit}} = 3H_0/8\pi G = 2.78 \times 10^{11} h^2 \, \mathrm{M_\odot}\,\mathrm{kpc}^{-3} \tag{1.15}$$

is the critical density of the Universe, i.e. the minimum density that the Universe should have in order to stop its expansion at infinite time. $H_0 = 100\,h$ km s^{-1} Mpc^{-1} is the present-date Hubble expansion rate, and $h = 0.674$ is the scaling factor of the Hubble expansion rate. The Universe total density parameter at a given time t is

$$\Omega_{\mathrm{tot}}(t) = \Omega_{\mathrm{b}}(t) + \Omega_{\mathrm{CDM}}(t) + \Omega_\Lambda + \Omega_\gamma(t)\,, \tag{1.16}$$

---

[4]The online tool used for the calculation of the transition epochs and of the age of the Universe in this section can be found at http://www.astro.ucla.edu/~wright/CosmoCalc.html. See also Wright (2006).

where Ω_b is the density parameter of baryonic matter (at present time, $\Omega_{b,0} = 0.0493$), Ω_{CDM} is the density parameter of CDM ($\Omega_{CDM,0} = 0.265$), Ω_Λ is the density parameter of the DE, and it is constant in time ($\Omega_\Lambda \equiv \Omega_{\Lambda,0} = 0.685$), and Ω_γ is the density of the relativistic components (where neutrinos contribute with a term $\Omega_{\nu,0} = 0.0012 - 0.003$, and the CMB contributes with $\Omega_{CMB,0} = 5.38 \times 10^{-5}$, for a total $\Omega_{\gamma,0} = \Omega_{CMB,0} + \Omega_{\nu,0} \sim 0.00125 - 0.00305$). $\Omega_{tot} = 1$ corresponds to a flat Universe, i.e. a Universe with infinite curvature radius, or with curvature density parameter $\Omega_k = \Omega_{tot} - 1 = 0$. This happens to be also the case of our Universe, with a curvature density parameter $\Omega_k = 0.0004 \pm 0.0018$ (Efstathiou & Gratton 2020).

The CMB radiation is an important measurable in the Universe. This was discovered first by Penzias & Wilson (1965) as a background signal in the microwave frequencies, and later investigations via different missions (Boggess et al. 1992; De Bernardis et al. 2000; Bennett et al. 2003a,b; Planck Collaboration et al. 2018) helped understanding its nature.

The CMB is a radiation component with a Planckian spectrum, peaked at the wavelengths of $1 - 2$ mm. This component is the fossil of the once hotter radiation that was interacting via Thompson scattering with electrons in the ionised baryonic plasma until the epoch of *decoupling* (Binney & Tremaine 2008, hereafter **BT08**). As the Universe was expanding, the equilibrium temperature of the CMB decreased, and at $z \sim 1300$ this radiation was not anymore energetic enough to keep baryons ionised. Thus, baryons started to recombine with electrons into neutral hydrogen atoms, and the epoch at $z \sim 1300$ is called *recombination epoch*. This epoch marked the end of the interaction between photons and baryons, i.e. it marked the era of decoupling of radiation from baryons, with last scattering surface at $z_{last} \sim 1100$ (Seager et al. 2000; Ryden 2003). As recombined hydrogen atoms were not interacting anymore with radiation, the Universe became transparent to it and the isolated CMB radiation has "frozen" its spectrum to the Planckian distribution, but the peak wavelengths have shifted to microwaves due to the Universe expansion (**BT08**), and hence the name "Cosmic Microwave Background" for this radiation component[5].

The CMB is important to test the validity of the ΛCDM cosmological model and of the assumptions on the cosmological parameters. Among the different confirmations are the flatness of the Universe, the dominance of the DE component and the fact that most of the matter is in CDM form (see the references above).

Last I mention that, due to the different evolution and relevance of the radiation, matter and DE density parameters in time, the Universe has encountered three different corresponding epochs where each of them dominated. These are (Frieman et al. 2008): 1) the radiation-dominated epoch, that lasted until $z \sim 3000$, i.e. until $t = 0.064$ Myr after the Big Bang; 2) the matter-dominated epoch, that lasted from $z \sim 3000$ to $z \sim 0.5$, i.e. until a time $t = 8.589$ Gyr after

---

[5]The additional radiation that we observe as photons coming from our Galaxy and from the other galaxies in the Universe has been produced later than recombination, after the galaxies started to form the first stars.

the Big Bang; 3) the DE-dominated epoch, that is currently ongoing.

1.3.2   Formation of the structures in the Universe

Now, I review how galaxies like the MW and its satellites are formed. In order to obtain a correct description of the formation of structures in the homogeneous and isotropic Universe, we need first to perturb the equations that describe the evolution of the matter content of the Universe.

I first introduce the basic equations of hydrodynamics. These can be successfully applied to our Universe, if we consider it behaving as a homogeneous and isotropic fluid where perturbations determine the local concentration of matter on the smaller scales (Kihara & Sakai 1970, as an example). These equations are useful to introduce the analytical linear perturbation approach to describe the growth of overdensities in the Universe, as a starting point for the formation of structures.

Linear perturbation of the equations of hydrodynamics and growth of the overdensities

Given a fluid defined in space and time, the basic equations describing its physical evolution are the following (see for instance **BT08**, Landau & Lifshitz 1987):

$$\begin{cases} \frac{\partial \rho}{\partial t} + \nabla \cdot (\rho \vec{v}) = 0 \\ \rho \frac{d\vec{v}}{dt} = -\nabla p - \rho \nabla \Phi \\ \frac{\partial}{\partial t}(\frac{1}{2}\rho v^2 + \rho\epsilon) + \nabla \cdot [\rho\vec{v}(\frac{1}{2}v^2 + w)] = 0 \,. \end{cases} \tag{1.17}$$

The first equation is the *continuity equation*. It describes the mass conservation in the fluid. In fact, if we consider an infinitesimal volume of matter with density $\rho = \rho(t)$, the density inside the volume will change in time according to the flow of matter from that volume, represented by the divergence of $\rho\vec{v}$.

The second equation is the *Euler equation*, and it was first derived by Leonhard Euler. It states that the force acting on a fluid element is given by the contribution of the pressure gradient ∇p and of the potential gradient $\nabla \Phi$ (where Φ can be, for instance, the gravitational potential).

The third equation is the *energy equation*. Here, $\rho\epsilon$ is the internal energy density of the fluid element, and $\frac{1}{2}\rho v^2$ is its kinetic energy density. $dw = Tds + (1/\rho)dp$ according to Landau & Lifshitz (1987), with T the temperature of the fluid and ds its infinitesimal entropy variation. The equation states that the total energy content of the fluid element increases inversely to the flow of energy, represented by the divergence term.

With reference to **BT08**, in the expanding Universe, adopting the comoving coordinates $\vec{x}$, the first two of Equations (1.17), i.e. the continuity and the Euler equation, can be rewritten as

$$\begin{cases} \frac{\partial \rho}{\partial t} + 3H\rho + \nabla \cdot (\rho \vec{v}) = 0 \\ \frac{\partial \vec{v}}{\partial t} + (\vec{v} \cdot \nabla)\vec{v} + 2H\vec{v} + \frac{\ddot{a}}{a}\vec{x} = -\frac{1}{a^2}\left(\frac{1}{\rho}\nabla p + \nabla \Phi\right) \,. \end{cases} \tag{1.18}$$

These equations describe the behaviour of matter in the expanding Universe in the comoving frame. If the average density in the Universe is $\bar{\rho}$, then at any given point $\vec{x}$ in space the overdensity

$$\Delta(\vec{x}) = \frac{\rho(\vec{x}) - \bar{\rho}}{\bar{\rho}} \tag{1.19}$$

represents the local deviation from homogeneity in the distribution of matter (**BT08**).

Introducing a linear perturbation to Equations (1.18) in a matter-dominated Universe returns, at large scales, a growing and a decaying mode. The growing mode has a dependence on time $\Delta \propto t^{2/3} \propto a$. Specifically, the last relation holds for a matter-dominated Universe, where in fact $a(t) \propto t^{2/3}$.

If the dominating fluid in the Universe is relativistic radiation, the linear perturbation of Equations (1.18) gives, on small spatial scales, an oscillating solution to the overdensity growth: any growing density perturbation is contrasted by radiation pressure and cannot increase in time. Instead, for large spatial scales, the overdensities grow as $\Delta \propto t \propto a$, where the last relation holds for a radiation-dominated Universe, where $a(t) \propto t$.

Linear growth of the overdensities: radiation-dominated epoch and matter-dominated epoch

Always with reference to **BT08**, in the radiation dominated epoch, until $z \sim 3000$, perturbations on large scales grow as much as $\sim t$, and the baryons are coupled with radiation, so also for baryons $\Delta \propto t$ during that epoch. Additionally, during the radiation-dominated epoch, DM overdensities cannot grow, since the free-fall timescale for gravitational instabilities would then be $t_{\rm ff} \sim (G\rho_{\rm m})^{-1/2} > t_{\exp,\gamma} \sim (G\rho_\gamma)^{-1/2}$, where the last term is the expansion timescale in the radiation-dominated Universe, and where $\rho_{\rm m} < \rho_\gamma$ during that epoch.

Later ($0.5 < z < 3000$), in the matter-dominated epoch, DM can start its gravitational collapse into haloes, while baryons are still coupled to radiation. After recombination ($z \sim 1300$), due to their large viscosities and conductivities, baryons cannot immediately collapse into haloes and the corresponding overdensities are damped. This process of baryonic overdensity damping is called *Silk damping* (Silk 1968) and dominates on scales of $\lesssim 10$ Mpc, i.e. the scales of galactic clusters. Thus, as pointed out in **BT08**, due to the Silk damping of baryonic overdensities, CDM is necessary to explain the formation of the galaxies, since being a collisionless form of matter it is not subject to this Silk damping at $\lesssim 10$ Mpc scales.

Thus, the linear growth perturbation method presented above explains, with a relatively simple formalism, how local overdensities of the matter and radiation content in the Universe can develop at a certain epoch and consequently grow in time, being therefore the seeds of the structures forming at later epochs in the Universe. The growth of the overdensities Δ is considered in the linear regime for small overdensity values, i.e. until when $\Delta \ll 1$. As I show below, when overdensities become larger ($\Delta \gtrsim 1$), other methods must be implemented in order to describe structure formation.

Non-linear growth of the overdensities

For the case of overdensities $\Delta > 1$, the linear regime of the perturbation theory previously described is in principle not valid anymore, because matter overdensities have entered a strong, non-linear regime of growth. Zel'Dovich (1970) proposed an analytical model of extrapolation of the linear overdensity growth to the case when $\Delta(\vec{x}, t) \gtrsim 1$.

This linear approximation of the strong growth regime is known as *Zel'dovich approximation* (ZA). The ZA can predict the formation of the large scale structure of the Universe in good agreement with N-body simulations, including the formation of filaments in which matter distributes in the large scale Universe, and the large voids in between. However, it breaks at a scale of $\sim 20h^{-1}$ Mpc, and already at $75h^{-1}$ Mpc it does not correctly take into account quadrupole terms of the redshift-space correlation function of the matter distribution (White 2014, and references therein). Also, another limit of the ZA is that it does not work in the case where there are converging streamlines that cross each other (Scoccimarro & Frieman 1996).

Numerical cosmological simulations are a valid alternative to describe the formation of structures in the strong, non-linear regime of overdensity growth. As I will explain later in Section 1.4, modern state-of-the-art cosmological simulations nowadays can make advantage of refined gravitational and baryonic physics algorithms to reproduce the formation of cosmic structures on a wide range of scales. In large numerical projects like the Millennium simulation (Springel et al. 2005b), it is found that CDM distributes in filament-like structures of $\sim 100h^{-1}$ Mpc scale. It is at the points of encounter of these filaments, called *nodes*, that virialised haloes are found to form (**BT08**).

Hierarchical clustering scenario

The currently, most accepted scenario of galaxy and structure formation is the so-called *hierarchical clustering* scenario (White & Rees 1978). According to this model, the first CDM structures that formed were the ones on the smallest spatial scales. These structures then merged (clustered) together to form larger structures, in a hierarchical fashion. This process is indeed called hierarchical clustering or *bottom-top* formation (**BT08**).

In numerical simulations, this hierarchical process of galaxy formation in large cosmological volumes can be reconstructed by determining the relation between (and the history of) the different haloes and the families of their progenitors and structures that merged together to build them. This can be done by computing the corresponding, so-called *merger tree*. An example of calculation of a merger tree is given by Genel et al. (2009) on the results of the Millennium cosmological simulation, by applying a standard friends-of-friends algorithm (Davis et al. 1985) to identify galactic haloes, their parents and progenitors, and the corresponding families of sub-haloes in the simulation.

As for the baryons, gas collapsing into the DM haloes eventually became dense enough and cold enough to undergo star formation (SF) and switch on the light of the first galaxies, at a CDM halo mass level of 10^6 M$_\odot$ (Bromm et al.

1999, and references therein). As the smallest galaxies formed and were creating stars from their gas reservoirs, these galaxies started to merge by means of gravitational interaction, and to accrete on larger structures. This process went on up to our epoch.

The satellites of the MW, which we observe and study, are the final remnants of a large number of objects with a wide range of masses that hierarchically accreted on each other, eventually merging into the main host halo, the MW halo. The fact that some of these satellite galaxies are not yet dissolved means that the process of accretion is still ongoing.

1.4   Tidal debris of the Milky Way satellites

Given the previous overview on the formation of galaxies like the MW, i.e. by means of the hierarchical clustering of the subhaloes hosting the satellite galaxies, it is clear that the streams of stars and gas that we observe around objects like the LMC and SMC, as well as the ones related to the Sgr dwarf, are the signatures of the dissolution process that these satellite galaxies are undergoing in the MW environment. Because they are still observable at our epoch, both these streams and the remnants of their progenitors are an important test of the validity of the ΛCDM predictions about the evolution of the MW environment. At the same time, these streams and remnants pose some challenges to understand which mechanisms and conditions play a role in determining their distribution properties.

What follows is an extract from my first author paper Mazzarini et al. (2020, hereafter **MM20**), written in collaboration with my supervisor A. Just (Astronomisches Rechen-Institut, Heidelberg), with A. V. Macciò (New York University, Abu-Dhabi), and with R. Moetazedian (formerly ARI). The extract corresponds to the Introduction section of the paper. The final part of the introduction, which was about the paper structure, was cut from this extract. I have modified and rearranged parts of the text where convenient, in order to adequate it to the context of this thesis. Figure 1.1 was not part of the introduction of the paper, and I added it here for illustration purposes.

1.4.1   Section 1. from Mazzarini et al. (2020): Introduction

As I have recalled in Section 1.3, within the ΛCDM theoretical framework MW-like galaxies are surrounded by several satellite galaxies, and in the hierarchical scenario of structure formation smaller DM haloes form in the earlier stages of the Universe, and later merge to form higher mass structures, with the central massive host galaxies being the end product of this process (Blumenthal et al. 1984). The satellite galaxies around the MW are the remnants of these subhaloes and progenitors accreted in the past in the MW environment.

A stream of gas, the Magellanic Stream, is observed in the MW environment (Wannier & Wrixon 1972; Mathewson et al. 1974; Nidever et al. 2010). This gaseous stream is attributed to the tidal interaction between the LMC and SMC, with a possible contribution of the MW environment to this process (Diaz

& Bekki 2011; Besla et al. 2016; D'Onghia & Fox 2016; Wang et al. 2019). Observations of the northern Galactic hemisphere give evidence of stellar overdensities in the shape of two elongated streams (Ibata et al. 1994; Newberg et al. 2007). These streams are the debris of a progenitor (identified with the Sgr dwarf galaxy) that has been interacting with the MW in the last gigayears, has thereby dissolved in the environment, and has lost matter (Martínez-Delgado et al. 2004). Other observations include the discovery of the Monoceros-Canis Major streams, with a progenitor of estimated mass similar to that of the Sgr dwarf, around 10^9 M$_\odot$ (Newberg et al. 2002). See Figure 1.1 for some of the observed streams of the MW satellites.
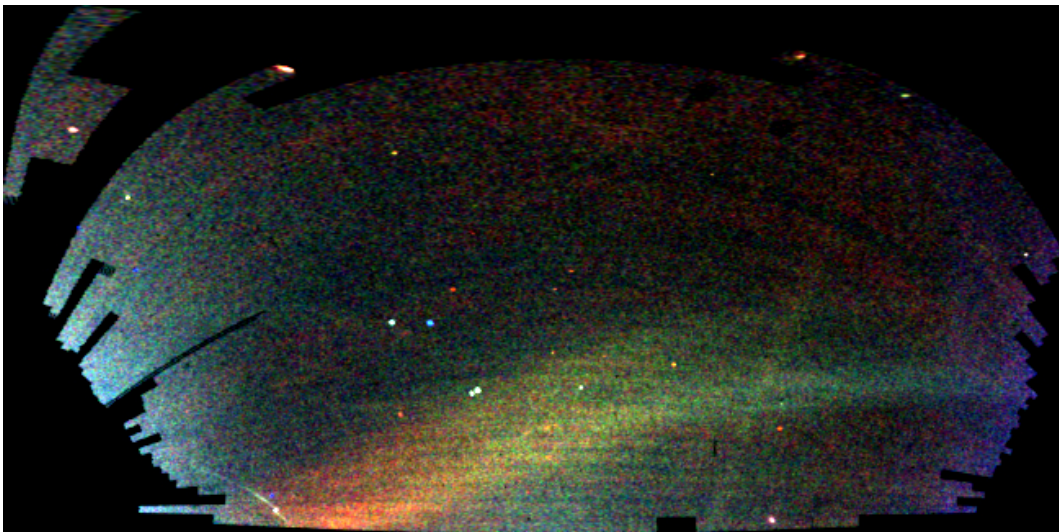
Figure 1.1: This astronomical image is a composite picture of the stars in the northern sky, coloured according to the magnitude ranges to which the observed stars belong (red for magnitudes r in the range $[21.33 < r \leq 22.0]$; green for $[20.66 < r \leq 21.33]$; blue for $[20.0 < r \leq 20.66]$). Different levels of intensity correspond to different levels of density of stars. Only turnoff and upper main sequence stars with $g - r < 0.4$ were chosen here. For turnoff stars belonging to the same population, higher magnitudes imply larger distances. Thus, the red-coloured streams are the furthest ones and the blue-coloured streams are the closest ones. Some of the streams of the MW satellites are captured, like the Sgr stream, composite of two contiguous horizontal arms having a colour gradation (i.e. showing a distance gradient from us); the Monoceros stream on the right side of the image; and a green stream cutting vertically the map close to the Sgr green-coloured bifurcation. See the page `https://www.sdss.org/science/idl-tiff-file-2` and Belokurov et al. (2006) for more information. Image credit: V. Belokurov and the SDSS.

Observations show that streams from dwarf galaxies are currently being destroyed in the MW environment. Signs of the past accretion of satellites can also be detected. From the abundances analysis of the data from Gaia DR2 and APOGEE (Apache Point Observatory Galactic Evolution Experiment, Abolfathi et al. 2018) surveys, recent work from Helmi et al. (2018) suggested that most of the inner halo of our Galaxy originated from a past major impact with the so-called Gaia Enceladus progenitor around 10 Gyr ago. Using DR2 photometry data combined with spectroscopic information from other surveys (Wilson et al. 2010; Cui et al. 2012; Kunder et al. 2017; Abolfathi et al. 2018; Mar-

rese et al. 2019), Koppelman et al. (2019) have identified new members of the Helmi stellar stream, originally identified in the solar neighbourhood by Helmi et al. (1999). Combining photometry and metallicity measurements with N-body experiments, they found low-metallicity populations and predicted that the Helmi stream originates from a dwarf galaxy of mass $M \sim 10^8 \, \mathrm{M_\odot}$, accreted onto the MW 5 Gyr ago.

Different observational and theoretical studies have focused on the spatial distribution of the MW satellites and of their debris, evidencing the presence of the so-called Vaste Plane of Satellites (VPOS), but also aligned streams of disrupted satellites (Pawlowski et al. 2012). By means of numerical simulations, Santos-Santos et al. (2019) found that the inertia tensor related to the spatial distribution of the bulk of satellites around the MW has a flatness c/a ranging from 0.1 for less than 10 satellites around the MW to 0.2 for more than 25 satellites around the MW. Buck et al. (2016) showed however that, even when forming these spatially coherent planes, satellites seem to be kinematically incoherent and these planar structures do not last a long time. Lisanti & Spergel (2012) focused on the DM debris in the Via Lactea II simulation and found evidence for the spatial homogeneity of its distribution. These results seem to be in contrast, in the perspective of understanding the distribution of the MW satellites and of their stellar and DM debris.

Considering the origin of the MW halo, the theoretical work of Pillepich et al. (2015) predicted that 70% of MW stellar content is formed in situ, that the majority of the ex situ stars come from in-falling satellites and characterise most of the stellar halo, and that the mass of these accreting satellites is relevant to the formation process of the MW halo. The additional study of Deason et al. (2016) suggested that the main contribution to the MW halo build-up (around $10^9 \, \mathrm{M_\odot}$) comes from larger satellites such as the LMC and SMC, whereby the contribution from ultra-faint dwarf galaxies (UFDs, with stellar masses below $10^5 \, \mathrm{M_\odot}$) is minimal.

Large numerical investigations such as the Aquarius and the Via Lactea II (Diemand et al. 2008) cosmological simulations successfully describe the clustering properties of Cold DM in large portions of the Universe (~ 100 Mpc) down to the scales of subhaloes and the main MW halo core ($\sim 10 - 100$ pc). These projects made use of state-of-the-art gravitational solvers (GADGET-3 after GADGET-2, and PKDGRAV; see Springel 2005; Stadel 2001, respectively), but lacked prescriptions for baryonic physics, which affects the final properties of the galactic haloes (Pontzen & Governato 2012), and in the case of galaxies like the MW influences the process of matter stripping from their satellite galaxies (Garrison-Kimmel et al. 2017). More recently, big simulation projects were dedicated to combine gravity and baryonic physics with refined numerical recipes (see AREPO, Springel 2010b) in order to obtain more accurate results in better agreement with observations of galaxies in the Universe (Vogelsberger et al. 2014b,a; Genel et al. 2014; Sijacki et al. 2015) or more specifically with the observational properties of dwarf galaxies (Wetzel et al. 2016, Latte simulation).

The zoom-in simulations Auriga (Grand et al. 2017) and Eris (Guedes et al.

2011) focus on the detailed properties of MW-like objects with a higher resolution (6×10^3 M$_\odot$ for gas particles and 4×10^4 M$_\odot$ for DM in Auriga, and 9.8×10^4 M$_\odot$, 2×10^4 M$_\odot$, and 6×10^3 M$_\odot$ for DM, gas, and stars in Eris). For their study on the environmental effects on the MW satellites, Buck et al. (2019) adopted a similar mass resolution, with stellar particles reaching a resolution of 6.7×10^3 M$_\odot$ and DM particles having a resolution of up to $\sim 10^5$ M$_\odot$. For comparison, in the IllustrisTNG (The Next Generation) project, the typical resolution of particles in TNG50 (its highest resolution simulation box; Pillepich et al. 2019; Nelson et al. 2019) is 8.5×10^4 M$_\odot$ for stars and 4.5×10^5 M$_\odot$ for DM. In other projects like Apostle (A Project Of Simulating The Local Environment, Sawala et al. 2016, 2017), which focuses on reproducing the kinematics and dynamics of the Local Group, the best resolutions for stellar and DM particles are 10^4 M$_\odot$ and 5×10^4 M$_\odot$, respectively.

While keeping in line with the best available resolution of DM particles ($M = 3.4 \times 10^3$ M$_\odot$ at best), Wang et al. (2015) made an advancement in resolving baryons for their NIHAO (Numerical Investigation of a Hundred Astrophysical Objects) cosmological simulations, with adopted masses as low as $M = 6.2 \times 10^2$ M$_\odot$ for gas particles. Their high-resolution simulations were used to study the evolution and properties of galaxies in a range of masses going from dwarf DM haloes of mass $M \sim 10^9$ M$_\odot$ to MW-like haloes with masses $M \sim 10^{12}$ M$_\odot$. Higher resolutions were also employed in cosmological simulations of isolated dwarf galaxies by **M17**, using the N-body code Gasoline (Wadsley et al. 2004) with SPH (Smoothed particle hydrodynamics) prescriptions for gas dynamics (Lucy 1977; Gingold & Monaghan 1977; Monaghan 1992). For their dwarf galaxy models, **M17** reached resolutions as high as $M = 1.2 \times 10^2$ M$_\odot$, $M = 4 \times 10$ M$_\odot$, and $M = 6 \times 10^2$ M$_\odot$ for gas, star, and DM particles, respectively. **M17** evolved their dwarf galaxy models in isolation (i.e. without any host MW exerting gravitational and hydrodynamical effects on them) in the redshift range $[100 < z < 1]$. The position-velocity (i.e. phase-space) distribution of stars and DM at $z = 1$ in these objects reflects the additional hydrodynamics, gas cooling, and stellar feedback recipes implemented in the **M17** simulations. Having switched on SF in their simulations, **M17** obtained satellites consisting of a realistic combination of DM particles, gas particles, and star particles.

1.4.2 Numerical study on the Milky Way satellite tidal debris distribution

Given the above picture, I will present in Chapter 3 our results from **MM20** of the study on the general properties of the MW satellites debris via numerical simulations. To do this, in this study we adopted a hybrid approach, for which we combined high-resolution MW models from the literature (with parameters extracted from cosmological data) with **M17** high-resolution dwarf galaxy models (employing them as satellites of the MW). Furthermore, the initial distribution of the satellites around the MW comes from the results of the

Aquarius cosmological simulations.

Our approach was similar to what was employed in **MJ16**. Following the numerical prescriptions of Yurin & Springel (2014), **MJ16** combined cosmological initial set-up and high-resolution numerical simulations. They modelled six MW numerical realisations, each consisting of live disc, bulge, and halo, and each with halo parameters extracted from the Aq-A2 to Aq-F2 cosmological simulations at redshift $z = 0$. They combined each MW model with a number of N-body satellites for which they extracted the parameters from the corresponding Aquarius snapshot. The mass resolution of their discs is $3.4 \times 10^3 \, \mathrm{M}_\odot$, higher than the stellar resolution in cosmological simulations. With this hybrid approach they were able to study the effect of a cosmologically motivated set of satellites on a high-resolution MW disc. Specifically, they focused on studying the impact that the MW satellites have on the MW disc vertical thickening and heating (where by disc heating it is meant the increase in time of the vertical velocity dispersion of its stellar particles). Since we wanted to address the distribution of both the stellar and DM satellite debris in our study, in contrast to **MJ16** we decided to employ a selection of satellites made of baryons and DM (hereafter hybrid satellites) that we extracted from the sample of dwarf galaxies described and studied in **M17**.

1.5 Milky Way bar and numerical simulations of bar buckling

In this section, I give an overview of what is currently known about the bar at the centre of the MW, including the X-shape. I also give an overview of the study of the bar buckling in numerical simulations of MW-like galaxies. This section is relevant to introduce the collaboration presented in Chapter 4, where I show the results of the numerical study on an N-body simulation of the MW, done to address the properties of the Galactic bar. In Chapter 4, I also briefly review the description of the bar properties (strength, phase angle and buckling) in terms of Fourier analysis, before presenting the results obtained so far with this collaboration.

1.5.1 The Galactic bar

The presence of a bar in the central part of the MW disc is given by a series of observational constraints (Kuijken 1996; Gerhard 2002). These include, for instance:

- The early micron (2.4μm) telescope observations of the centre of the MW (Matsumoto et al. 1982), by interpreting the surface brightness distribution in terms of a triaxial bar (Blitz & Spergel 1991);

- The stellar counts, as in Stanek et al. (1994) where, by analysing the distribution in magnitudes of the stars observed at the extremes of the bulge, the shift in their peaks in magnitude was interpreted with the presence

of a triaxial, non-spherical and elongated structure. Amôres et al. (2013) determined from stellar counts that the bar has an angle $(43\pm5)^{\circ}$ with the Sun-GC line, while the value suggested by Wegg & Gerhard (2013a) was equal to $(27\pm2)^{\circ}$, which finds confirmation in other literature (**P15** and references therein);

- Kinematic features, as in Palicio et al. (2018) that, comparing two numerical MW simulations with and without bar with the APOGEE stellar line of sight velocity (LOSV) data, found that the barred model reproduces better the kurtosis of the LOSV distribution of the observed stars close to the GC;

- The gravitational microlensing effects that the bar exerts on observed background stars (Alcock et al. 1995; Stanek et al. 1997).

The age of the MW bar is still under discussion. Using carbon stars as tracers of the age of the bar, Cole & Weinberg (2002) estimated an upper limit of 6 Gyr for it; they also found that its pattern speed is stable and that the bar is not a fading structure. Polyachenko et al. (2016) studied the formation of the bar in N-body runs for 4 Gyr using a full MW model (i.e. a model made of an N-body disc, an N-body halo and an N-body bulge). They found that the bar forms after 1.3 Gyr and therefore its age should be shorter than the one indicated by Cole & Weinberg (2002).

Regarding the mechanism of growth and evolution of the bar, Athanassoula (2002) argued that the presence of the halo and the exchange of angular momentum with it are favouring the growth of the bar. As a result of numerical simulations, Athanassoula (2003) obtained that the larger are the densities of the disc and the halo, and the colder is their kinematics, then the lower is the bar pattern speed and the higher is its strength. This is because of the possibility for the bar to exchange angular momentum with the disc and the halo, favouring its growth and its slowing down. Additionally, Athanassoula (2003) showed that the presence of a higher mass bulge in the GC favours more angular momentum exchange and, consequently, a strengthening of the bar.

As for our understanding of the shape of the bar, Athanassoula (2008) reported that N-body simulations, in agreement with observations (e.g. the comparison of images from N-body simulations with the near-infrared observations of bulges of edge-on galaxies, Lütticke et al. 2000), show a correlation between the bar strength and the formation of the B/P shape. Furthermore, based on previous studies, Athanassoula (2008) suggested that galactic bars are composed of an inner, short and thick part, corresponding to the B/P shape, and of an outer, extended and elongated feature. By both considering the distribution of red clump stars in individual observed stellar fields in the region of the long bar, and employing density models to fit all the observed fields together, Wegg et al. (2015) estimated a length of the bar $l_{\mathrm{bar}} \geq 4$ kpc, and a total stellar mass in the bar equal to 1.8×10^{10} M$_{\odot}$.

Gerhard & Wegg (2015) collected evidence from different studies, observational (for instance, Weiland et al. 1994; Wegg & Gerhard 2013a), numerical (Martinez-Valpuesta & Gerhard 2011) and analytical (Romero-Gómez et al.

2011), on the MW and on other galaxies. They found support to the idea that the MW central region may host a disc-like structure that immediately extends to the typical B/P structure with its characteristic X-shape, and that the extended region in the shape of a misaligned long bar is probably a disc feature.

Regarding the rotation of the bar, in their MW N-body simulations (which I already mentioned in Section 1.2.2) **P15** found that the bar has a pattern speed $\Omega_{\mathrm{bar}} \sim 25 - 30$ km s^{-1} kpc^{-1}, but they did not find complete agreement with previous literature. For comparison, different studies, including direct measurements, gasdynamical models applied to the position and velocities of HI and CO, and the study of the stellar velocity distribution bimodality in N-body simulations, obtained much higher values of pattern speed, in the range $\sim 50 - 70$ km s^{-1} kpc^{-1} (Dehnen 2000; Debattista et al. 2002; Englmaier & Gerhard 1999), while more recent studies (Rodriguez-Fernandez & Combes 2008; Long et al. 2012) placed the value somewhat closer to **P15**, though still higher ($\sim 30 - 40$ km s^{-1} kpc^{-1}). Thus, **P15** could not give a conclusive answer on the pattern speed of the bar.

Still, comparing their values of bar pattern speed with the rotation curve of Sofue et al. (2009), they could give their estimate of the ratio $\mathcal{R}$ between the bar corotation radius R_{corot} (the radius at which the bar pattern speed equals the angular rotation curve of a galaxy) and the bar length. They found a value $\mathcal{R} \sim 1.5 - 1.8$. Thus, since their value of $\mathcal{R}$ is larger than 1.5 they concluded that the bar is a slow rotator. For comparison, bars that have $1 \leq \mathcal{R} \leq 1.4$ are called fast bars (see for instance Debattista & Sellwood 2000). Also, for the corotation radius **P15** found a value of $R_{\mathrm{corot}} = 7.2 - 8.4$ kpc.

Additionally, **P15** found that their model with $\sim 40\%$ of the bulge mass in DM is the one that better constraints the stellar mass-to-light ratio obtained from the stellar initial mass function (IMF) of Zoccali et al. (2000, which was the best IMF that **P15** found in their analysis). Thus, with this fraction of DM in the bulge, they could estimate $M_{\mathrm{b,DM}} \sim 0.7 \times 10^{10}$ M$_{\odot}$.

From their models they could also estimate that the mass in the stars inside the B/P shape is $24^{+5}_{-4}\%$ of the total bar mass. This fraction, they claimed, is much higher than the previous estimates in literature, such as from Li & Shen (2012), that estimated anyway a fraction of 7% of the total bar mass residing in the X-shape, still translating into a detectable X-shape. The fraction of bar mass ending in the X-shape finds confirmation from two numerical simulations of Abbott et al. (2017) with MW-like N-body models, where they found that 19% and 23% of the bar mass in the two models distributes in the X-shape, respectively.

As for the orbits sustaining the X-shape, earier studies with numerical simulations (Pfenniger & Friedli 1991; Martinez-Valpuesta et al. 2006; Quillen et al. 2014) showed that the x1 family of orbits in the bar is the main responsible for the X-shape, as a consequence of orbits having angular speeds with ratios $\Omega_x : \Omega_z = 2 : 1$ (called "banana-shaped" orbits). However, Portail et al. (2015b) disagreed with these results, finding instead that the $2 : 1$ banana orbits do not contribute significantly to the X-shape. The X-shape is mostly the result of the contribution of different resonant orbits, of which the most impor-

tant ones seem to be the "brezel" $3\!:\!5$ orbits. Additionally, from the analysis of projected density distribution maps and unsharp masked images in their MW models, Abbott et al. (2017) confirmed that a variety of orbits contribute to the X-shape: non-resonant box orbits, long-axis tube orbits, resonant boxlet orbits. Particularly from the unsharp masked images the resonant boxlet brezel $3\!:\!5$ orbits and the additional "fish-brezel" orbits (with angular speed ratios $\Omega_x\!:\!\Omega_y\!:\!\Omega_z = 3\!:-2\!:0$) appear to be the main contributors to the X-shape, while the x1 banana orbits contribute only externally to the elongated boxy shape and cannot explain alone its characteristic inner bifurcation.

To sum up, the bar in the central regions of the MW appears to be a dominant feature in the disc: with a mass of $\sim 1.8 \times 10^{10}$ M$_\odot$, it represents about 40% the total mass of the disc, that is $\sim 4 \times 10^{10}$ M$_\odot$ (I already discussed this value in Section 1.2.1). Around 40% of its total mass is in the form of DM and a number of different orbit families contribute to the X-shape, that represents a non-negligible fraction, $\sim 20 - 30\%$, of its mass. However, to date there is still uncertainty on the value of the bar pattern speed and on the age of the MW bar.

1.5.2 Bar buckling in numerical simulations

Bar buckling is defined as the process by which the bar develops vertical asymmetries in the orbital distribution that determine its vertical bending. Athanassoula & Martinez-Valpuesta (2009) showed that, in simulated N-body galactic models, bars that undergo buckling diminish their strength for the period of the buckling, but increase the strength of their B/P feature. At this point, it is important to stress that the X-shape is not the buckling event per se. Rather, should there be any connection between the X-shape and the buckling, this is then a consequential relation, and not the same phenomenon.

Regarding the possible connection between buckling instability and X-shape, Quillen et al. (2014) showed from their numerical experiments that bar buckling is not a necessary mechanism for developing the X-shape, and that resonances in the orbits inside the growing bar are another driving factor. The result of Quillen et al. was obtained with mid-to-low–resolution simulations, with around 240K to 320K particles in the disc and 160K particles in the halo.

Previous numerical work from Martinez-Valpuesta et al. (2006) has evidenced that in simulated live discs embedded in live haloes it is possible to have a second, longer bar buckling episode of lower intensity. Also, they argued that the X-shape is developed as a consequence of the second buckling. They employed a disc with 8×10^5 particles. The presence of a second buckling event finds confirmation in more recent numerical work on a higher resolution disc from Łokas (2019), where the second buckling event is again less intense but lasts longer than the first one.

1.5.3 Numerical study on the Galactic bar

Based on the previous considerations, I will present in Chapter 4 the results of a collaborative effort in which we addressed, by means of N-body simulations,

the evolution properties of the bar in the MW, and where we tried to understand if the X-shape can develop without necessarily having a bar buckling. Furthermore, we wanted to understand the effects of the bar growth on the kinematics and dynamics in the inner MW disc. E. D'Onghia performed a high-resolution numerical simulation of the MW, already described in D'Onghia & Aguerri (2020), inclusive of N-body disc, bulge and halo, and evolved in isolation using the code GADGET-3. We used this simulation to perform our analysis of the growth of the Galactic bar, of its effects on the inner MW disc, and of its buckling and X-shape.

1.6 Thesis: structure and content

What follows is a summary of the structure and content of the thesis.

In this chapter, I gave an overview of the MW and its environment, specifically its disc, bulge and DM halo, as well as its satellite galaxies. I gave a review of some aspects of the ΛCDM model that are useful to understand the MW environment in a cosmological context. I then provided an overview, taken from the introduction of my first author paper, **MM20**, of the tidal streams of the MW satellites, illustrating the goal of this thesis, that is addressing the distribution of the satellite tidal debris in the Galactic environment. I finally gave an overview of the Galactic bar and I introduced the collaboration to study the MW bar in a numerical simulation.

In Chapter 2, I review the numerical methods for N-body simulations of galaxies. I then report the results of a benchmark performed to test how the N-body codes GADGET-2 and CHANGA (Jetley et al. 2008, 2010; Menon et al. 2015) reproduce the evolution of the MW disc in isolation and interaction with the MW satellites, in comparison to the results obtained by **MJ16** with the N-body code SUPERBOX-10 (Bien et al. 2013). I finally show the improvements of the code GADGET-4 (Springel et al. 2020, in prep; hereafter **S20**) in terms of momentum conservation with respect to GADGET-2.

In Chapter 3, I show the extract of **MM20** corresponding to the parts where I present our simulations of MW-satellites interaction, and the results of the study on the distribution of the satellite stellar and DM debris. At the end of the chapter, I also show a brief investigation on how the calculation of the tidal radius of a satellite galaxy of the MW is affected by the kind of MW potential employed, to check the impact of our approximations on the calculation of the satellite tidal radii.

In Chapter 4, I show the results of a collaboration with other researchers, to study the evolutionary properties of the MW bar in an N-body high-resolution simulation. The research is focused on studying the growth of the bar, the impact of the bar on the MW inner disc, and the process of bar buckling. Additionally, I show some of the properties that we found in the X-shape.

In Chapter 5, I give a conclusive summary of the results obtained in this thesis. I also provide some additional discussion and I present the future, possible developments of the projects described in this thesis.

Chapter 2

A numerical comparison of SUPERBOX-10, CHANGA, GADGET-2, and GADGET-4

In this chapter, I present the results of a benchmark done in order to compare the performance of the N-body codes GADGET-2 and CHANGA against the results on the evolution of the MW, both in isolation and in interaction with its satellite galaxies, obtained by **MJ16** with the N-body code SUPERBOX-10. The goal of this benchmark is to show that GADGET-2 is a robust code that still produces similar results in comparison with the other two, more modern codes. I discuss the benchmark in Section 2.7. Additionally, in Section 2.8 I show that momentum conservation is improved moving from GADGET-2 to the follow-up code GADGET-4, and that GADGET-4 is therefore a good choice for performing the simulations discussed in Chapter 3.

Before discussing the benchmark, in Sections 2.1 to 2.5 I first review some numerical methods employed to run N-body simulations in astrophysics. These are useful to discuss the benchmark presented in this chapter and the simulations presented in Chapter 3 and in Chapter 4. In Section 2.6 I introduce the N-body codes SUPERBOX-10, CHANGA and GADGET-2.

Galaxies are gravitating systems, i.e. systems whose dynamic evolution is mainly determined by gravitational interactions. In the context of computational astrophysics and N-body simulations, a gravitating system is typically discretised in N particles. Each particle has a position and a velocity, to sample the discrete phase-space distribution of the system, and a mass, to sample the discrete spatial mass distribution of the system. The masses of the particles and their total number N determine the mass and number resolution of the system. In order to simulate the evolution of a gravitating N-body system with a numerical code, the code needs 1) the input ICs of the system; 2) a method to calculate the forces acting on all the particles, and therefore to calculate the accelerations that they suffer; 3) a scheme to integrate particles positions and velocities in time, i.e. to update their velocities and positions by a finite timestep, once their accelerations are computed.

System of units in numerical simulations

The units of measure adopted in numerical simulations are called *internal units*. The three fundamental quantities to describe the mechanics of N-bodies are length, time and mass, with corresponding dimensions indicated by [L], [T] and [M], respectively. The dimension of the gravitational constant is defined by [L], [T] and [M], exactly as $[G] = [L]^3[T]^{-2}[M]^{-1}$.

Therefore, a typical convention for the internal units it to choose them so that correspondingly $G = 1$. This means that, of all the units U_{L}, U_{T}, and U_{M} (length unit, time unit and mass unit, respectively), one needs to fix two units to have the full set of the three determined. For instance, by adopting $U_{\mathrm{L}} = 1$ kpc, and $U_{\mathrm{M}} = 2.325 \times 10^5\,\mathrm{M}_\odot$, then U_{T} is close to 1 Gyr. With this advantageous choice, moreover, another unit like the velocity unit, U_{V}, is $\sim 1\,\mathrm{km\,s}^{-1}$.

2.1 Initial conditions of numerical simulations

To run a simulation with a code on a computer or a computer cluster, the code requires to be given the initial conditions (ICs). Mathematically, the ICs are a collection I of vectors and scalars,

$$
\begin{aligned}
I \equiv \Big(&\vec{r}_1(0), ..., \vec{r}_N(0), \vec{v}_1(0), ... \\
&..., \vec{v}_N(0), m_1(0), ..., m_N(0) \Big),
\end{aligned}
\tag{2.1}
$$

where, for each i-th particle in the system ($i = 1, ..., N$), $\vec{r}_i(0)$ represents its initial position, $\vec{v}_i(0)$ its initial velocity, and $m_i(0)$ its initial mass.

An additional parameter file can add information about how to run the simulation, providing the values of parameters that regulate specific behaviours of the code. Examples of parameters required to run a simulation may be the softening ϵ to limit the divergence of the gravitational force (see Section 2.2.3); the timestep Δt required to advance the simulation in time at every integration step (see Section 2.3); the opening angle θ to regulate the accuracy of the tree opening procedure in case the code implements a tree algorithm (see Section 2.2.2).

The more is the simulated physics complicated, the more are the requested additional parameters. For instance, the additional presence of gas particles in the simulation, as well as of stellar evolution recipes in the code, will require input data for other physical parameters, such as the initial temperature of gas particles or the initial metallicity of stellar particles. Also, additional parameters may regulate the choice of the kind of physics to implement for gas (e.g. if gas has metal cooling or if gas is evolving adiabatically), how much energy is released by supernovae or whether to include the cosmological expansion of space during the integration of the system.

To sum up, the combination of ICs and parameters provides all the information that the code needs to calculate the evolution of an N-body system. The way the code calculates gravity and implements recipes to simulate additional physics determines the complexity of the required ICs and parameters.

2.2 Force calculation

In a gravitating N-body system, given two particles P_i and P_j, with masses m_i and m_j and coordinates $\vec{r}_i$ and $\vec{r}_j$, we define the gravitational potential Φ_{ij} felt by P_i and due to P_j as

$$\Phi_{ij} = -G\frac{m_i m_j}{r_{ij}}\,, \tag{2.2}$$

where G is the universal gravitational constant and $r_{ij} = |\vec{r}_i - \vec{r}_j|$ is the distance between P_i and P_j. The Newtonian force acting on the particle P_i due to the particle P_j is calculated as

$$\vec{F}_{ij} = -\nabla\Phi_{ij} = -G\frac{m_i m_j}{r_{ij}^2}\hat{u}_{ij}\,, \tag{2.3}$$

where $\hat{u}_{ij}$ is the unit vector applied on P_j and oriented towards P_i. Then, the particle P_i will feel a total force $\vec{F}_i$ due to all the other particles P_j equal to

$$\vec{F}_i = \sum_{\substack{j \neq i}}^{N} \vec{F}_{ij}\,, \tag{2.4}$$

where $i, j = 1, ..., N$ and $\vec{F}_{ij}$ is the same as in Equation (2.3) for particles P_i and P_j. This system of differential equations is analytically unsolvable in the general case. Thus, N-body methods are used to solve the system of Equations (2.4), by computing the forces acting on all the particles, and therefore their accelerations $\vec{a}_i(t) = \vec{F}_i(t)/m_i$. Depending on the kind of gravitating system, different numerical solvers employ different algorithms to calculate the forces acting on particles.

In N-body systems where pair-wise gravitational particle interactions are frequent, strong and relevant to determine their acceleration, one needs to use the system of Equations (2.4) to determine the integration of velocity and position of each particle. The N-body codes that adopt this approach are called *direct N-body codes*. The advantage of this approach is that all the interactions are taken into account to determine the evolution of particles in the system.

The disadvantage is the high computational cost. For each of the N particles, the total force acting on it is the sum of $N - 1$ terms, each corresponding to the force due to each of the other $N - 1$ particles. Any computer calculating the force acting on all particles in this way will execute a number $N \times (N - 1) \propto N^2$ of operations, with the N^2 dependence being valid for large N. For a system simulated at high resolution with at least $\sim 10^7$ particles, the number of required operations per timestep is $\sim 10^{14}$, in order to calculate all the forces acting on all the particles. A computer with a performance of 1 Gflops (i.e. 1 billion FLoating point OPerations per Second) would need 10^5 s, i.e. more than 1 day, to calculate the force acting on all the particles for integrating one timestep only!

In order to reduce the computational costs of this operation, simulations are usually performed in parallel, i.e. the computational workload is distributed among many processors or many GPU threads operating together at the same

time. Therefore, parallel computing and parallel software programming are fundamental concepts in N-body simulations.

It can be shown (**BT08**) that for galactic systems, like for instance the MW, which are made of a large number of stars (the MW has $\sim 10^{10}$ stars), and with a typical density of ~ 1 star pc^{-3}, single star-star interactions are infrequent and therefore they can be neglected. In this case, it is rather the total potential of the galaxy that determines the resulting force felt by each star. These systems are called *collisionless* systems.

Given the negligible importance of pair-wise interactions in collisionless systems, and given the very large (typically > 1M) number of particles that are used nowadays to describe them in N-body simulations, the calculation of the force in an N-body collisionless system is simplified by means of proper algorithms. The codes implementing these algorithms are called *indirect N-body codes*. I describe now two N-body indirect schemes, the PM algorithm and the tree algorithm, in Section 2.2.1 and in Section 2.2.2, respectively.

2.2.1 Particle mesh algorithm

Given an N-body system embedded in a grid or mesh, a particle mesh (PM) algorithm is an algorithm that implements the Poisson equation to calculate the potential from the distribution of the N-body particles in the grid, and hence calculates the force acting on the particles. The Poisson equation describes the local relation between the gravitational potential derivatives and the matter density distribution. It has the form

$$\nabla^2 \Phi(\vec{r}) = 4\pi G \rho(\vec{r}), \tag{2.5}$$

where $\nabla^2 \Phi(\vec{r})$ and $\rho(\vec{r})$ are the Laplacian of the gravitational potential Φ and the matter density, respectively, both evaluated at radius $\vec{r}$.

In N-body systems, where the number of particles is finite, the mass distribution is discrete and a possible solution to Equation (2.5) is given by using the Fourier space. The idea behind this approach is that the convolution of two functions corresponds to a product in the Fourier space. Below I follow Bien et al. (2013) for a brief description of the algorithm.

The simulation volume can be divided in a grid of $N_a \times N_b \times N_c$ cubic cells. Each cell has mean density $\rho_{a,b,c}$, with $a = 1, ..., N_a; b = 1, ..., N_b; c = 1, ..., N_c$. The discrete potential $\Phi_{a,b,c}$ in the cell of indexes a, b, c is then given by

$$\Phi_{a,b,c} = \sum_{a_1,b_1,c_1} H_{a_1-a,b_1-b,c_1-c}\rho_{a_1,b_1,c_1}, \tag{2.6}$$

i.e. summing on all the other cells with indexes a_1, b_1, c_1. Here $H_{a_1-a,b_1-b,c_1-c} = [(a_1 - a)^2 + (b_1 - b)^2 + (c_1 - c)^2]^{-1/2}$ is the discrete Green function, as in Bien et al. (2013). In the Fourier space, the potential is then Fourier-transformed to

$$\hat{\Phi}_{i,j,k} = \hat{H}_{i,j,k}\hat{\rho}_{i,j,k}, \tag{2.7}$$

where $\hat{H}$ and $\hat{\rho}$ are the Fourier transforms of H and ρ, respectively. The Fourier transform (FT) of Φ is then simply the product of the FTs of H and ρ. The final evaluation of the potential comes from anti-transforming Equation (2.7).

From the evaluation of the potential in the cells, by applying a discrete gradient one can calculate the forces acting on the particles. The system can be then integrated (as an example with SUPERBOX-10, see Section 2.6.1 for the computation of the force starting from the potential calculated in the grid cells).

Particle mesh codes and fast Fourier transform: cost

For a grid of cells with size $N \times N \times N$, if a method like the fast Fourier transform is applied, the procedure requires $N^3 \times \log(N)$ calculations, with N being the number of cells per size (Bien et al. 2013). This kind of approach has the advantage that does not scale with a power of the number of the particles N_{P}- unlike N-body direct codes that scale with N_{P}^2 for large N_{P} -, but only with a power of the number of cells per dimension. If $N \ll N_{\mathrm{P}}$, then this operation is much less expensive than force calculation in N-body direct codes.

2.2.2 Tree algorithm

The base idea of tree algorithms is to recursively divide the simulation volume into sub-volumes or sub-cells of parallelepipedic or cubic shape. The force acting on particles is evaluated with contributions from single particles or from the mass centres of the sub-volumes, depending on the criterion. In analogy with a tree ramification, the whole simulated volume is the tree, while each sub-volume (or *sub-cell*) is the *node* or branch of the tree. When a minimum number of particles (corresponding to a given threshold) is found in a sub-cell during the tree subdivision, the algorithm stops the subdivision of that cell, that is then called the *leaf* of the tree. In Figure 2.1 I show a schematic representation of the tree hierarchy and domain decomposition.

An important reference for tree codes is the scheme presented by Barnes & Hut (1986). Hereafter I refer to this as BH tree. The BH tree is an oct-tree. This means that each volume or sub-volume is divided in 8 sub-cells. There are other kinds of tree, similar to the BH tree. Another example is the binary tree, where each cell is divided along the longer axis in only 2 sub-cells, as described in Wadsley et al. (2004). In the case of Wadsley et al., the division in sub-cells is done along the direction of the longest cell side, and the point of division along the longest cell side is chosen so that there is no sub-cell without particles.

Instead of evaluating the force acting on a test particle due to all the other $N - 1$ particles, a tree algorithm operates a distinction. All the particles inside cells that are far enough from the test particle will be substituted by a common centre of mass $\bar{m}$, and their interaction with the test particle is substituted by the interaction of $\bar{m}$ with the test particle. Otherwise, if the cell is not far enough from the particle, then it will be "opened", i.e. the same evaluation proceeds with its sub-cells. To evaluate whether to stop the tree traversal at a given cell or to open it, the code uses a threshold parameter, the *opening angle* θ. Whenever
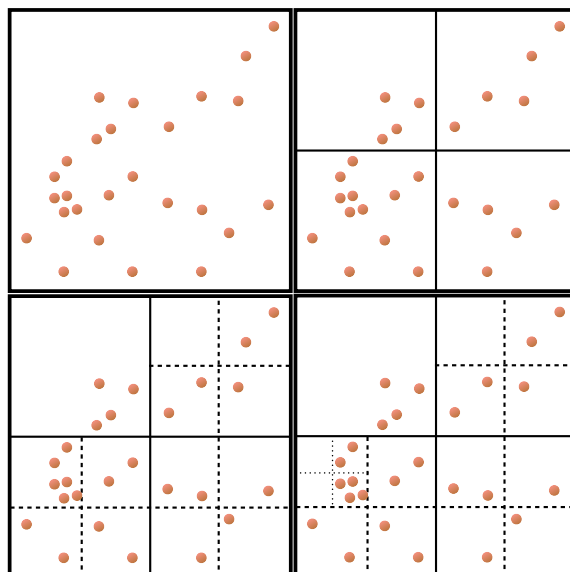
Figure 2.1: Schematic representation of the domain decomposition in a tree code. The representation is in the two-dimensional space for graphical convenience, therefore I chose to represent a quad-tree (i.e. a tree where every cell is divided in four sub-cells). I chose an arbitrary total number $N = 26$ of particles. For the leaf level, I chose a threshold of four particles per cell. The tree decomposition is represented in the four panels delimited by thick full lines, and it is executed in the order given by the following text. *Top left panel*: The whole simulation box is considered, with all the N particles distributed inside. *Top right panel*: Since the total number of particles is $N > 4$, the first level of division in four cells is applied to the whole simulation volume, and it is represented by the thin full lines. *Bottom left panel*: The top-left sub-cell has four particles, therefore it is not further divided (it has reached the leaf level). The other three sub-cells have each more than four particles, therefore they are divided each in four sub-cells (dashed lines). *Bottom right panel*: The only further division is applied to one sub-cell (thin dotted lines), since there are more than four particles there. After this operation, all the sub-cells have been divided until leaf level and the domain decomposition stops here. This scheme is conceptually similar to the scheme represented in Figure 1 of Springel et al. (2001).

a cell satisfies the opening angle criterion,

$$\frac{l}{d} > \theta \, , \tag{2.8}$$

the cell is opened and the same evaluation will be done on its sub-cells, until leaf level is reached. Here l is the linear cell size and d is the distance of the cell to the test particle.

In case Equation (2.8) is not satisfied, the particles in the cell are added to a common list where they are substituted by $\bar{m}$, and for that cell the code calculates the gravitational force on the test particle due to $\bar{m}$. Otherwise, the cell is opened and the code proceeds with applying the criterion of Equation (2.8) to its sub-cells.

If the value of the opening angle is chosen too large, too many cells will not be opened and the code will lose accuracy in the force calculation. If the opening angle is chosen too small, more cells are opened, with a consequently higher accuracy in the force calculation, but with a higher computational cost, because of more particle-cells force evaluations.

Multipole expansion

The evaluation of the force due to a not open node on a distant test particle is done by means of the *multipole expansion* of the mass distribution of the nodes (and hence of the long-distance gravitational potential and force acting on particles). This is done in order to consider the fact that the distribution of mass in the node is not point-like, and gravitationally speaking this impacts on the test particle differently from a point-like source. As an example, if the node is a cube of homogeneously distributed mass, the hexadecapole expansion of the potential is (Barnes & Hut 1989)

$$\Phi(\vec{r}) = \frac{GM}{r} + \frac{7}{960}\frac{GMa^4}{r^9}[3r^4 - 5(x^4 + y^4 + z^4)], \qquad (2.9)$$

where the first term is the monopole term of gravity, $\vec{r} = (x, y, z)$ is the position vector of the test particle seen from the node, r is the corresponding magnitude, and a is the size of a side of the cell/node. As I show later in Section 2.6 when introducing CHaNGa and Gadget-2, different codes implement the expansion in different ways.

Tree codes: cost

Tree codes scale with order $O(Nlog(N))$, where N is the number of particles (Barnes & Hut 1986). This is better than $O(N^2)$ of the direct codes. See Appel (1985) for an early discussion on the speed-up that a tree code has in numerical simulations with respect to direct summation codes.

2.2.3 Gravitational softening

Given two point particles P_i and P_j, if their distance r_{ij} goes to 0 (i.e. if the two point particles approach each other infinitesimally), the force calculation represented by Equation (2.3) diverges. This has some consequences, apart from the obvious unphysical meaning of a force diverging to infinite.

First, the more the two point particles get closer, the more they can suffer a very large acceleration due to each other's effect. Thus, their mutual approach introduces a large kick to their motions.

Second, given that in many codes (as we will see later) the integration in time is done assigning discrete timesteps to each particle, inversely proportional to some power of the particle's acceleration, this means that for that pair of particles the assigned timestep is very low. This slows down the whole integration of the system.

In order to solve this problem, one can introduce the so-called softening length ϵ. This is a parameter defined in order to limit the gravitational interaction between two particles within finite values, as they mutually approach.

Many N-body codes adopt a kernel function to implement the softening in Equation (2.3). The simplest form of softening kernel is the one associated to a

Plummer sphere of radius ϵ, for which the force calculation of Equation (2.4) takes the form

$$\vec{F}_i = -G \sum_{\substack{j \neq i}}^{N} \frac{m_i m_j}{(r_{ij}^2 + \epsilon^2)^{1.5}} \vec{r}_{ij} \,, \tag{2.10}$$

as in Athanassoula et al. (2000), for instance. The Plummer sphere is an example of infinite kernel, where the modification to the pure Newtonian law is extended to all distances between particles. In fact, here the term ϵ is always inserted in the calculation of the force.

There are more refined formulas than Equation (2.10) to avoid the divergence of the gravitational interaction at short distances. The spline kernel for the calculation of the force from the works of Gingold & Monaghan (1977) and Hernquist & Katz (1989) takes the form

$$g(r) = \begin{cases} 1/\epsilon^3 [4/3 - (6/5)u^2 + (1/2)u^3] \,, \ 0 \leq u \leq 1 \\ 1/r^3 [-1/15 + (8/3)u^3 - 3u^4 + (6/5)u^5 - (1/6)u^6] \,, \ 1 \leq u \leq 2 \\ 1/r^3 \,, \ u \geq 2 \end{cases}$$

$$\tag{2.11}$$

where ϵ is the particles softening and $u = r/\epsilon$ is the radial distance between particles normalised by the softening. $g(r)$ here has the dimension of acceleration per unit length and unit mass, with $G = 1$. The force $\vec{F}$ is calculated as

$$\vec{F}(r) = mg(r)\vec{r}, \tag{2.12}$$

where m is the mass of the particle that suffers the force $\vec{F}(r)$, and $\vec{r}$ is the vector pointing from the test particle to the source exerting the gravitational force.

This expression returns three different behaviours for the spline kernel, depending on the distance between the particles. At one extreme case, if two particles are distant less than $u = 2$ (i.e. the distance r is less than two times the softening parameter ϵ), the spline returns a softened expression for the force calculation, that does not diverge to infinity as Equation (2.3) does for $r \to 0$. At the other extreme case, for $u > 2$ (i.e. for distances $r > 2$ times the softening parameter) Equations (2.11) reduce to Equation (2.3). This is an example of finite kernel, because over a certain distance the force between particles is again Newtonian as in Equation (2.3). Some codes like the one by Dehnen (2000) consider also the node-node interaction by means of an evaluation mediated by a spline kernel.

2.3 Time Integration

Once the forces - and therefore the accelerations - acting on particles are calculated, particles must have their positions and velocities $\vec{r}, \vec{v}$ integrated in time, with $\vec{v}(t) - \vec{v}(0) = \int_0^t \vec{a}(t')dt'$ and $\vec{r}(t) - \vec{r}(0) = \int_0^t \vec{v}(t')dt'$. However, since there is no analytical expression to solve this integration, N-body codes make use of discrete timesteps Δt.

A way to advance the whole simulation in time is to use a common, *global* timestep Δt, with the advantage of having the particles synchronised in time, because they all have their positions and velocities updated together. However, this choice can be inadequate in situations where there is a range of dynamical timescales over which the particles evolve.

2.3.1 Individual timesteps and block timesteps

In the case of collisional systems, adopting the same, global timestep may show some limitations. If some particles in the simulation suffer strong accelerations (because they closely interact with other particles, or they are in dense regions where the mean gravitational field changes quickly), updating them with the same common timestep Δt of particles that do not suffer strong accelerations is not optimal. In fact, if the global timestep is chosen too small to follow the evolution of the strongly accelerating particles, the whole simulation is slowed-down because the timestep is too smaller than necessary for the many particles that do not suffer these strong accelerations. On the contrary, a choice of too large timesteps is good for the integration of particles that suffer low accelerations, but leads to lose accuracy in the orbit integration of the highly accelerated particles.

A better way to do the integration in this case is to attribute first *individual* timesteps to the particles, and then to organise them into a hierarchy, by means of *block* timesteps. An example of individual timestep is the generalised Aarseth timestep (Nitadori & Makino 2008; Capuzzo-Dolcetta et al. 2013)

$$\Delta t = \eta \Big(\frac{A^{(1)}}{A^{(p-2)}} \Big)^{1/(p-3)} , \tag{2.13}$$

where η is the accuracy parameter, p is the order of the integration scheme and $A^{(m)}$ being

$$A^{(m)} = \sqrt{|a^{(m-1)}||a^{(m+1)}| + |a^{(m)}|^2} , \tag{2.14}$$

with a being the particle acceleration and $a^{(m)}$ being its m-th derivative. With these individual timesteps, a hierarchy is established and particles with a lower timestep need to be integrated first, and consequently their positions and velocities will be updated more rapidly than particles with a higher timestep.

However, if the individual timesteps are not one the exact multiple of the others, the update of particles in time becomes asynchronous and the whole integration is more complicated to handle. This is why the individual timesteps are organised in block timesteps. The block timesteps satisfy the following recursive relation between two contiguous timesteps,

$$\Delta t_k = \Delta t_{k-1}/n , \tag{2.15}$$

with $k = 2, ..., M$, and with n being a factor, for instance $n = 2$ (convenient because of the binary representation of numbers in computers). With this notation, the largest timestep is Δt_1. Particles whose individual timestep Δt falls

between t_k and t_{k+1} are attributed the same block timestep Δt_k. Every n advancements in timestep Δt_k for particles belonging to the k-th block, particles belonging to the $(k-1)$-th block will be updated with timestep Δt_{k-1}.

In this model of time integration, every particle that can have position and velocity updated at the current timestep is called *active* particle, while each particle whose position and velocity are not updated in the current timestep (because their individual timestep falls in a higher level inside the block hierarchy, i.e. it is larger) is called *passive* particle.

2.3.2 Timesteps in simulations of collisionless systems

In all the simulations - including large cosmological simulations - involving collisionless systems like galaxies and galaxy clusters there is a wide range of dynamical scales that interests the evolution of these systems (Springel 2005; Wadsley et al. 2004). This makes using only one global timestep inconvenient to advance the simulation in time.

An alternative is employing a combination of individual timesteps for particles and of block timesteps in which to group them, as well as of global timesteps to determine the maximum overall size of the block hierarchy. Usually this maximum timestep is taken to be a fraction of the dynamical timescale of the simulated system. An example is illustrated in Quinn et al. (1997), where the maximum timestep is chosen such that

$$\Delta t_{\mathrm{max}} < \frac{\eta}{\sqrt{G\rho}} \,, \tag{2.16}$$

with ρ the typical density of the system. Here, the dynamical timescale is $t_{\mathrm{dyn}} \sim (G\rho)^{-1/2}$.

Again, distributing the individual timesteps into a hierarchy of block timesteps, starting from the largest timestep Δt_{max}, allows synchronisation between the different particles. For a comparison of the efficiency of different timestep criteria, see Power et al. (2003).

2.3.3 The leapfrog method, a symplectic integration scheme

Once we have timesteps for particles, we need to update the system. The theoretical foundations for the integration methods employed in N-body systems come from considerations on classical Hamiltonian systems, such as described in Springel (2005). Hamiltonian systems have the equations of motion for the particles in the phase-space $(\vec{r}, \vec{v}) \equiv (\vec{q}, \vec{p})$ described by

$$\begin{cases} \dot{\vec{q}}_i = \frac{\partial H}{\partial \vec{p}_i} \\ \dot{\vec{p}}_i = -\frac{\partial H}{\partial \vec{q}_i} \end{cases} \tag{2.17}$$

for a number of particles N and with $i = 1, ..., N$. Here, H is the Hamiltonian of the system,

$$H = \sum_{i=1}^{N} \frac{1}{2} m_i |\vec{v}_i|^2 + \frac{1}{2} \sum_{i=1}^{N} m_i \sum_{j=1, j \neq i}^{N} \Phi_{ij} \equiv H(\vec{q}, \vec{p}) \,. \tag{2.18}$$

In this last equation, the first term after the first equality sign is the sum over all the kinetic terms of the N particles while Φ is the potential energy (in this case, the gravitational potential).

As pointed out in Springel (2005), Hamiltonian systems are not stable against perturbations: some integration methods may introduce numerical approximations that increase the inaccuracy in time integration and can eventually destabilise an Hamiltonian system. A way to solve this problem is to introduce the so-called *leapfrog method* (Quinn et al. 1997; Springel 2005) by adopting two possible techniques: the $kick-drift-kick$ (KDK) or the $drift-kick-drift$ (DKD), where the $drift$ operator D updates the position from the previous to the next value, and the $kick$ operator K similarly updates the velocity. In the case of the KDK method, the operator for the total time integration has the form $K(\vec{r}, \vec{v}, \Delta t/2) D(\vec{r}, \vec{v}, \Delta t) K(\vec{r}, \vec{v}, \Delta t/2)$. This means that the update is done first with a kick on velocities,

$$K(\vec{r}, \vec{v}, \Delta t/2) : \vec{v}(t) \to \vec{v}(t + \Delta t/2) = \vec{v}(t) + \vec{a}(t)\Delta t/2 \,, \tag{2.19}$$

followed by a drift operation with an update on positions,

$$D(\vec{r}, \vec{v}, \Delta t) : \vec{r}(t) \to \vec{r}(t + \Delta t) = \vec{r}(t) + \vec{v}(t + \Delta t/2)\Delta t \,, \tag{2.20}$$

and concluded with a second kick on velocities,

$$K(\vec{r}, \vec{v}, \Delta t/2) : \vec{v}(t + \Delta t/2) \to \vec{v}(t + \Delta t) = \vec{v}(t + \Delta t/2) + \vec{a}(t + \Delta t)\Delta t/2 \,. \tag{2.21}$$

With the first kick the velocity is updated for half the integration time, according to the gravitational acceleration that the particle suffers at time t. After that, the position is updated according to the half-time update of the velocity value. Last, the final kick advances the velocity to the next time, considering the acceleration of the particle in the new position.

Here, $\vec{a}(t) \equiv \vec{a}(\vec{r}(t))$ is the particle acceleration calculated at the initial position, and $\vec{a}(t + \Delta t) \equiv \vec{a}(\vec{r}(t + \Delta t))$ is the particle acceleration calculated at the final position. The usage of $\vec{v}(t + \Delta t/2)$ instead of $\vec{v}(t)$ to integrate $\vec{r}$ allows more accuracy, since the position is updated considering the variation of the velocity during the integration. Similarly, the last kick is done using the acceleration of the particle at the next step to update the velocity, thus considering the evolution of the dynamics that the particle suffers from time t to time $t + \Delta t$.

This method of integration is *symplectic*, i.e. it is symmetric with respect to the direction of time integration. Therefore, it is convenient since it reduces long-term increases in energy errors during the integration of the system.

In order to take into consideration the different dynamical timescales of particles in a simulation, a way to implement the KDK is to group particle timesteps in blocks, and advance active particles by means of a KDK integration. As pointed out by Quinn et al. (1997) and Springel (2005), integration schemes where timesteps are distributed in a block hierarchy are not exactly symplectic, even if the single timestep updates of each particle are done by means of a KDK leapfrog method. Nonetheless, in this case the symplectic nature of the KDK leapfrog method is preserved in the single timestep advancement of the active particles.

2.4 Smoothed particle hydrodynamics

Simulations that include gas need additional recipes to treat hydrodynamics. Gas and fluids are in fact described by additional physical quantities such as density, pressure, temperature, entropy and viscosity that give complete information about their behaviour. To describe the behaviour of gas, one can adopt an *Eulerian* or a *Lagrangian* approach.

With the Eulerian approach, the description of the fluid system focuses on a given point in space and describes how the physical parameters of the fluid change as a function of each point in space and of time. For the gas density ρ, one would have for instance $\rho = \rho(\vec{r}, t)$, with $\vec{r}$ and t being independent coordinates in space and time. With the Lagrangian approach, instead, one follows the individual fluid elements as they move through space and time and as they change their physical parameters. The calculation of the density for a small gas element that moves in space and time with a parametric equation $\vec{r} = \vec{r}(t)$ is $\rho = \rho(\vec{r}, t) \equiv \rho(\vec{r}(t), t)$, with $\vec{r}$ depending in this case on t.

An example of Eulerian numerical scheme is the *Adaptive mesh refinement* (AMR, Berger & Oliger 1984; Berger & Colella 1989), a technique that makes use of a mesh with sub-grids of different size to describe the properties of gas in a simulation. There is no gas particle employed in this method, and cells of different sub-grids in the mesh have sizes that adapt to the local hydrodynamical properties of gas. AREPO (Springel 2010b) is a modern example of hydrodynamical adaptive mesh code that provides an improved scheme that eliminates the lack of Galileian invariance typical of AMR codes.

For the case of Lagrangian numerical solvers, the typical example is represented by the SPH method (Gingold & Monaghan 1977; Lucy 1977, already mentioned in Section 1.4.1 of this thesis). SPH is a method to solve the Euler equations of hydrodynamics directly for N-body gas particles. Therefore, SPH does not adopt any grid in space.

2.4.1 SPH: smoothing the properties of gas particles to solve the equations of hydrodynamics

The three Equations (1.17) describe the basic properties of fluids. Their application to N-body gas particles however is not straightforward. In fact, Equations (1.17) are valid for a fluid, that can be represented as a continuous system. The discretisation of fluids in particles makes them incompatible with a continuous representation.

The idea behind SPH is to smooth the properties of each gas particle according to a given number of closest gas particles (the neighbours), before interpreting gas particles as a continuous fluid. To do this, one associates a *smoothing length* h to each gas particle in the simulation. h is then the radius of a sphere centred on the particle, within which the N_h closest neighbours are included. Then, by introducing a kernel function W with compact support, it is possible

to smooth the given parameter a of the gas particle as:

$$a_{0,i} \rightarrow a_{\mathrm{s},i} = \sum_{j=1}^{N_h} W a_{0,j} \,. \tag{2.22}$$

Here, $a_{0,i}$ and $a_{\mathrm{s},i}$ are the initial and smoothed value of a for the particle i, respectively. W can be expressed as a function of the distance r_{ij} between the i-th and j-th particles and of their smoothing lengths, h_i and h_j, $W \equiv W(r_{ij}, h_i, h_j)$ (Stinson et al. 2006). The employment of the kernel W in Equation (2.22) is intended to smooth the properties of each gas particle with the contributions of the neighbour particles. In this way, the fluid can be considered as a continuous system and the Equations (1.17) can be solved for each gas particle. Having W a compact support, this means that only for particles within a certain range of distances the kernel W is non-null, while out of that radius W is null. For instance, (Stinson et al. 2006) chose this radius to be equal to $2h$, i.e. two times the smoothing length of gas particles.

Among the advantages of SPH, the method is Galilean invariant (Springel 2010a) and like other Lagrangian methods it is suitable for systems with large density contrasts (Tasker et al. 2008). However, SPH shows problems in resolving shocks, and in treating fluid discontinuities and instabilities (Springel 2010b). In contrast, Tasker et al. (2008) pointed out that AMR and Eulerian codes appear to work better in systems with regions of rapid change in density, since they better resolve the properties of gas on smaller scales with the usage of the adaptive grid, while they lack Galileian invariance (as mentioned above) and they show problems with overmixing in hydrodynamic systems (Springel 2010b).

2.5 Sub-grid physics: star formation, gas cooling, supernova feedback

Additional behaviour of baryonic matter, such as gas cooling processes, SF and stellar feedback can be described introducing additional recipes to simulate these effects happening on scales smaller than the mass resolution of the N-body particles. As an example, if the resolution limit of gas particles in a simulation is of $10^3 \, \mathrm{M_\odot}$, the birth of a star of $10 \, \mathrm{M_\odot}$ cannot be directly simulated as the collapse of more gas particles together, since there is not enough mass resolution for that. Therefore, additional recipes are implemented to attribute a series of physical properties and behaviours to each particle, to simulate these events happening below mass resolution. These recipes are called *sub-grid* recipes. To give some examples, I am going to describe SF, gas cooling and supernova feedback.

2.5.1 Star formation

SF is the process of spawning a new stellar particle from simulated gas. In the case of SPH codes, this means spawning a stellar particle from a gas particle. In practice, there are different ways to implement this process.

One way is to apply the concept of stability of a molecular gas cloud of temperature T and density ρ, as well as the observations of the SF rate (SFR) in disc-like galaxies, to the procedure of spawning stellar particles from gas particles. The base criterion to determine if a molecular gas cloud is unstable to gravitational collapse is to evaluate if in the cloud there is any perturbation with a size larger than a critical length, the Jeans Length, defined as

$$\lambda_J = \sqrt{\frac{RT}{G\rho}} \, , \tag{2.23}$$

where $R = N_A k_B = 8.314 \text{ J K}^{-1}\text{mol}^{-1}$ is the universal constant of gas, $k_B = 1.38 \times 10^{-23} \text{ J K}^{-1}$ is the Boltzmann constant, and $N_A = 6.022 \times 10^{23}$ is the Avogadro Number. This criterion was first derived by Jeans (1902). The Jeans length expresses the maximum scale of a sound wave that can cross the cloud without triggering its collapse through gravitational instability. From Equation (2.23) it is clear that colder and denser clouds will collapse easier and will form stars easier.

Observations of star forming, gas-rich galaxies suggest that the surface density of star forming gas, Σ_{SF}, and the surface density of gas, Σ_{gas}, are related through the Schmidt-Kennicutt relation (Kennicutt 1998). The Schmidt-Kennicutt relation has the form

$$\Sigma_{SF} = (2.5 \pm 0.7) \times 10^{-4} \Big(\frac{\Sigma_{gas}}{\text{M}_\odot \, \text{kpc}^{-2}} \Big)^{1.4 \pm 0.15} \text{M}_\odot \, \text{yr}^{-1} \, \text{kpc}^{-2} \, . \tag{2.24}$$

Combining the previous concepts, the idea in numerical simulations is to find a criterion to decide whether or not a gas particle is cold and dense enough to spawn a star particle, to reproduce the Schmidt-Kennicutt relation in star forming systems.

As an example of implementation of SF via jeans instability criterion in N-body SPH simulations, I report the method illustrated by Katz (1992). According to this method, a gas particle, in order to be eligible for SF, must be part of a converging flow that is unstable according to the Jeans criterion of Equation (2.23). Assuming the smoothing length h_i to be the size of the i-th gas particle and c_i its local sound speed, the condition of Jeans instability is obtained if the gas particle satisfies the requirement $h_i/c_i < 1/\sqrt{4\pi G\rho_i}$, where the term h_i/c_i represents the sound crossing timescale, and the term $1/\sqrt{4\pi G\rho_i}$ is the dynamical timescale.

If the particle is eligible to SF, a random number is compared to its SF probability, calculated as

$$p = 1 - e^{-c_* \Delta t / t_g} \, , \tag{2.25}$$

with c_* being the dimensionless SFR parameter, Δt being the integration timestep and t_g being the maximum between the local gasdynamical timescale and the

local gas cooling timescale. If this random number is larger than p, a star particle is spawned.

Even if the mass of an SPH particle represents the resolution limit of the simulated star forming regions, alternative numerical implementations to the one showed above adopt a strategy to simulate an environment with many phases inside the same particle where to form stars. This is for instance the case of the explicit method for quiescent mode SF presented by Springel & Hernquist (2003). In this case, the total SPH particle mass m is divided in three components, the ordinary gas (gas that does not undergo any cooling or SF process), the cold gas and the formed stellar component, with masses m_g, m_c and m_*, respectively. Initially, $m_* = 0$.

Inside the particle, every timestep Δt there is a conversion of a fraction of gas mass into stellar mass, as

$$\Delta m_\mathrm{SF} = m_\mathrm{c} \frac{\Delta t}{t_*}, \qquad (2.26)$$

where t_* is the timescale for converting cold gas into stars. The remaining fraction of gas mass is distributed between cold gas and ordinary gas, and evolves according to a proper hydrodynamical treatment, see Springel & Hernquist (2003).

Therefore, each SPH (initially gas) particle, after starting to form stars, has a time interval during which both a stellar collisionless mass fraction and a gaseous mass fraction co-exist together. When the total stellar mass inside the particle satisfies the condition $m_* > 0.5m$, the particle is fully converted into a stellar particle of mass m_*. The remaining gas mass is distributed to the neighbour SPH particles. For an alternative, simplified version of the explicit method reported here, see again Springel & Hernquist (2003).

2.5.2 Gas cooling

Gas cooling is the process of temperature decrease in gas. In numerical simulations, this is typically represented by molecular hydrogen cooling or metal line emission cooling.

Modelling gas cooling processes requires an additional energy variation term into the Equations (1.17), inclusive of a cooling function Λ, which in the general case is a function of the parameters of the gas, like temperature and density. A description of the behaviour of the cooling function Λ due to metals and molecular hydrogen can be found in Sutherland & Dopita (1993) and in Shen et al. (2010). Also, a description of the non-equilibrium abundances of the elements concurring to gas cooling in the specific case of SPH simulations is provided by Christensen et al. (2012).

Gas cooling is important to lower gas temperature and allow gas to form stars, if also other conditions are satisfied, (see the above SF treatment, for instance). In fact, gas cooling diminishes the temperature of gas in Equation (2.23) and therefore diminishes the Jeans length. This means that even a density wave with a small size can trigger the gravitational collapse of a gas cloud, if this is cold enough.

2.5.3 Supernova feedback

At the end of their evolution, stars can undergo different fates. Specifically, if stars are massive enough (i.e. $M_* \gtrsim 10\,M_\odot$), they finally reach a phase of core collapse explosion. This explosion is known as *supernova*. Supernovae II are associated with the core collapse of a neutron star after that nuclear burning has led to the production of Iron in its core, and after that the process of neutronisation has converted all the iron into neutrons inside the star. Supernovae II release a large amount of energy in the surrounding space ($\sim 10^{51}$ erg) and therefore are important to regulate SF in the interstellar environment of galaxies (Silk 2003; Stinson et al. 2006).

An example of supernovae II feedback implementation in N-body SPH simulations is the *supernova blastwave* model by Stinson et al. (2006). In their model, if in a stellar particle at a given time there is a supernova II explosion, the particle distributes a fraction of the total 10^{51} erg of energy, ΔE_{SN}, to the i-th neighbouring gas particle as

$$\Delta E_{\mathrm{SN}}, i = \frac{m_i W(|\vec{r}_i - \vec{r}_\mathrm{s}|, h_\mathrm{s})\Delta E_{\mathrm{SN}}}{\sum_{j=1}^{N} m_j W(|\vec{r}_i - \vec{r}_\mathrm{s}|, h_\mathrm{s})} \,, \tag{2.27}$$

where they defined h_s as the distance of the stellar particle to the 32nd closest gas particle, and where W is the smoothing kernel for SPH. In this model, only thermal energy is considered as feedback since the kinetic energy of gas is converted to gas thermal energy in timescales smaller than typical simulation timesteps. To simulate the effects of the supernova blastwave on the surrounding gaseous environment, the authors imposed that the gas particles within h_s switch off cooling for an amount of time, in order to prevent these particles from forming stars when receiving the thermal feedback from the supernova.

2.6 Superbox-10, ChaNGa and Gadget-2

In the Sections 2.1 to 2.5, I showed some methods employed in numerical simulations in astrophysics. Now I present the codes Superbox-10, ChaNGa and Gadget-2, to show how the numerical methods discussed before apply to their cases.

2.6.1 Superbox-10

As I mentioned at the beginning of this section, Superbox-10 was the code employed by **MJ16** to perform their set of N-body simulations. Superbox-10 is a PM code and it adopts the fast Fourier transform illustrated in Bien et al. (2013) to calculate the gravitational potential and hence the force acting on particles. I have recalled the principles of PM codes in Section 2.2.1.

Superbox-10 employs also a system of nested grids of cells. The system of nested grids works as follows.

For each galaxy, an inner grid of cells is attributed to its densest region, in order to obtain high resolution in the calculation of the acceleration applied

to the N-body particles there. An example can be the grid applied around the bulge of a disc galaxy. A second grid is employed for the calculation of the force at intermediate resolution, and for instance it can be localised in the region of the disc of a galaxy.

A third, global grid is employed to sample matter distribution in the remaining regions of the simulation box, with the lowest resolution. For more details, see Bien et al. (2013). Superbox-10 improves the vertical resolution of disc-galaxy-like systems by introducing a flattening parameter, that represents the vertical-to-horizontal ratio of the cells, thus increasing the vertical force resolution, following Just & Jahreiß (2010).

Having calculated the potential in each cell, it is possible to calculate the force acting on each particle. For instance, a given particle in the a, b, c-th cell will have an acceleration a_x along the x-direction equal to

$$
\begin{aligned}
a_x =\ & \frac{\Phi_{a+1,b,c} - \Phi_{a-1,b,c}}{2l_x} + \frac{\Phi_{a+1,b,c} + \Phi_{a-1,b,c} - 2\Phi a,b,c}{l_x{}^2}\Delta x \\
& + \frac{\Phi_{a+1,b+1,c} - \Phi a - 1,b+1,c + \Phi_{a-1,b-1,c} - \Phi_{a+1,b-1,c}}{4l_x l_y}\Delta y \\
& + \frac{\Phi_{a+1,b,c+1} - \Phi a - 1,b,c+1 + \Phi_{a-1,b,c-1} - \Phi_{a+1,b,c-1}}{4l_x l_z}\Delta z \,,
\end{aligned}
\tag{2.28}
$$

where $\Delta x, \Delta y, \Delta z$ are the particle coordinates inside the cell and where l_x, l_y, l_z are the lengths of the cell in the three coordinate directions x, y and z.

The integration in Superbox-10 is performed by means of a leapfrog method and with a global timestep, following Fellhauer et al. (2000). The code allows to choose timesteps conveniently small to integrate the simulated systems, like in the case of **MJ16**, that chose a timestep $\Delta t = 0.1$ Myr in order to have a high degree of accuracy in the integration of their simulations of MW-satellites interaction.

2.6.2 CHaNGa

CHaNGa is the last N-body code (together with the recent Gasoline-2, see Wadsley et al. 2017) in a series started with the development of pkdgrav and prosecuted with Gasoline. The code makes use of the optimised parallelisation provided by Charm++ [1], to better distribute workload between cores[2]. As for the parallelisation of the simulations in CHaNGa discussed in this chapter, I made additional use of routines and modules from the Open-MPI distribution[3], that follows the MPI (Message Passing Interface) protocol for parallel communication between cores in computer clusters. I also made use of the TIPSY[4]

---

[1]See http://charmplusplus.org.

[2]I used the CHaNGa release 3.7.1. As for the cluster version of the code, given the linux-based cluster employed to perform the simulations, I installed the verbs-netrls-linux-x86 version of CHaNGa and Charm++.

[3]See https://www.open-mpi.org/ for more information.

[4]By N. Katz and T. Quinn, see the page http://faculty.washington.edu/trq/hpcc/tools/tipsy/tipsy.html.

package to convert the ICs data for SUPERBOX-10 into a proper format readable by CHANGA.

The tree algorithm adopted in CHANGA is a modification of the BH tree in the form of a binary tree, similar to what is described in Wadsley et al. (2004). To control the accuracy of the tree opening, the code employs an opening angle θ by means of the cell-opening criterion of Equation (2.8). A value of the opening angle $\theta \sim 0.5 - 0.55$ represents the typical, standard choice. For the calculation of the force, the code employs a softening length parameter ϵ and the spline kernel of Equations (2.11) for softening the forces when distances between particles and nodes are less than 2ϵ, with ϵ being the average of the softening values of the two interacting objects (particle or node). For distances more than 2ϵ, the Newtonian force is recovered.

Additionally, CHANGA makes use of the hexadecapole expansion to describe matter distribution inside the tree cells and for the calculation of the force acting on particles due to distant nodes (see Stadel 2001, for more details about the calculation of the hexadecapole expansion terms). However, when particles and cells are distant less than the average softening length, the spline-softened force is evaluated only with the monopole term (Menon et al. 2015).

The combination of the standard opening angle values with the hexadecapole expansion of the matter distribution grants a high accuracy in the calculation of force in cosmological simulations (Menon et al. 2015). On the other side, this requires a higher computational effort, as I will show later in the benchmark.

Time integration is done by means of the leapfrog KDK scheme introduced in Section 2.3.3, following Quinn et al. (1997). In particular, each particle of given softening ϵ and acceleration a has an individual timestep Δt given by

$$\Delta t = \eta \sqrt{\frac{\epsilon}{a}}. \tag{2.29}$$

Here η is a parameter that controls the integration accuracy. Like in Quinn et al. (1997), the maximum timestep can be set to be below the dynamical timescale of the integrated system, as in Equation (2.16). Starting from this maximum timestep, the code distributes particle timesteps into a block hierarchy as in Equation (2.15).

CHANGA was developed to simulate baryonic physics as well, and SPH and sub-grid physics are implemented in the code. I only mention the main features of these implementations, and I do not discuss them into detail, since I did not use them for the simulations presented in this thesis, that are N-body-only simulations.

As for the treatment of gas, the SPH implementation of CHANGA improves the calculation of entropy and thermal diffusion processes, as well as the description of pressure gradients and timesteps, following the results of previous literature (Wadsley et al. 2008; Shen et al. 2010; Durier & Dalla Vecchia 2012; Menon et al. 2015). Thanks to this revision on the SPH formulation, the code can solve some issues like the Kelvin-Helmholtz instability problem, with a bet-

ter performance than the SPH prescriptions of GADGET-2 (see Figure 1 of Menon et al. 2015).

As for the implementation of sub-grid physics, SF in CHaNGa is regulated as a mechanism mainly developing in cold, dense gas regions (Menon et al. 2015), and gas cooling is implemented by means of recipes describing metal lines and molecular hydrogen cooling, following Shen et al. (2010) and Christensen et al. (2012). Feedback from supernovae is included with two alternative mechanisms: the already discussed blastwave model and the *superbubble* mechanism. For a description of the superbubble mechanism, see Keller et al. (2014). This formulation of sub-grid physics allows CHaNGa to reproduce with success a number of processes related to stellar evolution (Menon et al. 2015, and references therein).

2.6.3 GADGET-2

The N-body code GADGET-2 was developed as the sequel of GADGET-1 (Springel et al. 2001). GADGET-2 offers a range of possible input/output formats. I have chosen to work with the HDF5 format[5], due to its intuitive, hierarchical organisation of the data in directories inside the files. The installation of GADGET-2 requires MPI protocols for parallel support when running simulations.

Like its predecessor, GADGET-2 is a tree code that follows the BH tree algorithm. GADGET-2 adopts only the monopole expansion term to describe the distribution of matter in the tree cells. However, the code compensates this lower accuracy with a revised opening angle criterion, requesting that a node is opened if the error on the corresponding monopole force evaluation on the test particle is very small compared to the last total acceleration $\vec{a}$ of the particle, i.e.

$$\frac{GM}{r^2}\left(\frac{l}{r}\right)^2 \leq \alpha|\vec{a}|\,, \tag{2.30}$$

with M being the total mass in the node, l and r being the size and distance of the node from the particle, respectively, and α being a parameter to control the tolerance on the error (Springel 2005). The default value of α is set to 0.005. Also, a node is always opened for force evaluation if the test particle is inside its volume. With this opening criterion being employed, the old BH opening angle criterion of Equation (2.8) is used in a simulation only for the first evaluation of the forces, while the tree walks in the subsequent timesteps follow the revised criterion of Equation (2.30).

Also, the construction of the oct-tree in GADGET-2 combined with the monopole evaluation of the mass distribution in cells is claimed to have a series of advantages, included a more efficient memory management and a better tree update that avoids long-term large errors in the integration (Springel 2005).

The force softening is done by employing a similar spline kernel to the one illustrated in Equations (2.11), but with some modifications. The spline kernel

---

[5]For more information on HDF5, see the page `www.hdfgroup.org`.

in GADGET-2 has the form

$$f(r,u) = \begin{cases} 1/h^3[10.67 + u^2(32u - 38.4)]\,, & 0 \leq u \leq 1/2 \\ 1/h^3(21.33 - 48u + 38.4u^2 - 10.67u^3 - 0.67/u^3)\,, & 1/2 \leq u \leq 1 \\ 1/r^3\,, & u \geq 1 \end{cases}$$

(2.31)

with $u = r/h$ and with h being 2.8 times the larger of the softening values of the two interacting objects (particle or node). This means that, adopting the same softening ϵ as in CHANGA, the Newtonian force in GADGET-2 is recovered within a larger range (1.4 times more) than the range of CHANGA.

In GADGET-2 time integration is done following the KDK leapfrog method of Quinn et al. (1997). The method, like for the case of CHANGA, is quasi-symplectic and as I showed in Section 2.3.3 it avoids long-term divergences in the energy errors.

GADGET-2 distributes the individual timesteps of particles into a block hierarchy as in CHANGA. The timestep for each $i-$th particle is calculated as

$$\Delta t_i = \min\left[\Delta t_{\max}, \sqrt{\frac{2\eta\epsilon_i}{a_i}}\right]\,,$$

(2.32)

where η again is the accuracy parameter, ϵ_i is the softening length of the particle, a_i is the magnitude of the acceleration vector of the particle, and $\Delta t_{\max}$ is a maximum timestep that holds for all the particles. Similar to Equation (2.16), also in GADGET-2 the optimal choice for the maximum timestep is when this is smaller than the dynamical timescale of the simulated system.

Like for CHANGA, I used GADGET-2 for N-body-only simulations, switching off all the SPH and sub-grid physics recipes. Therefore, like I did above for CHANGA, I am only going to briefly describe the SPH and sub-grid physics implemented in GADGET-2.

As for the treatment of gas dynamics, GADGET-2 implements the SPH recipes of Springel & Hernquist (2002), that have the advantage of manifestly conserving gas energy and entropy, improving on the previous, older implementations of SPH in numerical codes (Springel 2005). Additionally, both the treatment of radiative cooling and heating by photoionisation (Katz et al. 1996) and molecular hydrogen cooling recipes (Yoshida et al. 2003) are implemented in the code.

GADGET-2 adopts the multi-phase treatment of SPH particles to simulate SF in gaseous mixed environments at a sub-grid level, including regulation by supernova feedback. This follows the prescriptions of Springel & Hernquist (2003), that I already presented in Section 2.5.1.

2.7 Benchmark: comparing SUPERBOX-10 , CHANGA and GADGET-2

In this section, I present the benchmark done with the N-body codes SUPERBOX-10, CHANGA, and GADGET-2. The goal of this benchmark, as mentioned before,

is to show that GADGET-2 produces similar results to CHANGA and SUPERBOX-10, that are more modern codes, and that therefore the choice of a subsequent, modern version of the GADGET family of codes is suitable for the N-body experiments presented in Chapter 3.

For the benchmark, I considered the three following types of run performed by **MJ16** using the Aq-D2 ICs. The three simulations are:

- A run simulating the isolated evolution of a full N-body MW model made of disc, bulge and halo. I will refer to this run as RELAX, since in this first Gyr the MW model develops instabilities that propagate through the disc, relaxing to the new equilibrium distribution function (DF) starting from the initial axisymmetric set-up;

- A run simulating the isolated evolution of the same model starting at the end of the first run, without MW satellites. I will refer to this run as ISOLATION, because it served as a control case for the evolution of the MW in interaction with its satellites;

- A run having the same IC MW model as in the ISOLATION run, but including DM-only N-body satellites that orbit around the MW. I will refer to this run as INTERACTION. This is also the kind of simulation performed by **MJ16** to study the impact of the satellites on the disc vertical thickening and heating.

2.7.1 Numerical set-up for the benchmark

I show here the ICs of the MW models and of the satellite models employed in the benchmark, following **MJ16**. I also discuss the parameters employed in CHANGA and GADGET-2 to run the simulations with these two codes, the cluster used for the simulations, the choice of the snapshots, and the coordinate rescaling before analysing the results of the simulations.

Initial conditions of the Milky Way and of the satellites

As explained in **MJ16**, the simulated MW N-body model consists of live disc, live bulge and live halo, with 10M, 500K and 4M particles, respectively. **MJ16** realised six initial MW models following the Aq-A2 to Aq-F2 cosmological simulations. For the benchmark, I chose the Aq-D2 case because of the average properties of the model with respect to the other five cases. It is in fact the model with respect to which **MJ16** rescaled the properties of the other five MW models.

All the MW models were generated by **MJ16** using the code GalIC (Yurin & Springel 2014). The code takes as input the desired, target equilibrium density distributions of the bulge, disc and halo components and the desired additional constraints, like the values of velocity dispersion of these components. It samples the target DF with N-body particles, with an initial guess on their kinematics. It integrates their orbits, similar to the Schwarzschild (1979) orbit-based method, and evaluates inside spatial cells the time-averaged numerical

quantities corresponding to the target ones. By adjusting iteratively the velocities of particles, the code searches for the simultaneous minimisation of the relative differences between the numerical density and velocity dispersion values and the corresponding target values. The final distribution of the particles in the phase-space samples the desired equilibrium DF for the model ICs.

I give now a summary of the properties of the Aq-D2 model, while more details can be found in **MJ16**, and while in their Table 4 there is a summary of the MW model parameters. This table, together with Table 2 and Table 3 of their paper, is useful in the light of giving a summary of the properties of all their six MW models and of the satellite models employed around them [6].

The disc was modelled with an exponential density profile, as described in Equation (1.1) and with $P = 1$. The disc scale length is $h = 2.8$ kpc and the scale height is $z_0 = 0.277$ pc. The total mass is 3.42×10^{10} M$_\odot$.

The bulge was modelled as a Hernquist profile, with density profile as in Equation (1.4). The scale radius was chosen to be $a_b = 0.35$ kpc, while the total mass is $M_b = 1.9 \times 10^{10}$ M$_\odot$.

The information about the MW halo was reconstructed from the corresponding NFW halo extracted at redshift $z = 0$ in the Aq-D2 simulation. The halo at redshift $z = 0$ has a total virial mass $M_{200} = 1.77 \times 10^{12}$ M$_\odot$ at a virial radius $r_{200} = 242.8$ kpc. The final N-body halo employed in the simulation was obtained by best-matching the properties of this NFW halo with a Hernquist profile of the same total mass as M_{200}, like described in Section 1.2.3. The NFW scale radius is $r_s = 24.95$ kpc, with a concentration parameter $c = r_{200}/r_s = 9.37$. The Hernquist scale radius of Equation (1.8) is therefore $a = 43.90$ kpc.

Finally, in the INTERACTION simulation, the additional 23 satellites have 50000 particles each [7]. The satellites span over a range of masses, going from $\sim 10^8$ M$_\odot$ to some 10^9 M$_\odot$. **MJ16** generated the 23 N-body satellites adopting the recipes from Lora et al. (2013) to return spheroidal N-body galaxy models with NFW density profiles. The initial positions and velocities of the satellites in the MW environment was set by **MJ16** following the corresponding data extracted at redshift $z = 0$ from Aq-D2. In Table 2.1 I sum up the relevant parameters of the MW model and the number of satellites employed for the benchmark.

CHANGA: parameters used in the runs

The parameter for the tree code opening angle θ was put to a value dTheta= 0.55, which is within the range of recommended values. For each particle of given softening ϵ and acceleration a, the timestep Δt is given by Equation

---

[6]**MJ16** performed an additional set of simulations with a set-up that followed the indications from the Via Lactea II cosmological simulations. However, this is far from the scope of this thesis.

[7]I have to report some discrepancies in these numbers. Due to a small issue in the conversion code from SUPERBOX-10 to GADGET-2, the last satellite had ~40200 particles instead of 50000 particles. The satellite mass lost in this way was $\sim 2.5\%$ of the total satellite mass. However as we will see from the results presented in this chapter, the disc evolution of the MW in interaction was not deeply affected by this in GADGET-2, with respected to the other codes.

Table 2.1: Relevant parameters describing the MW model by **MJ16** after extracting the corresponding data from the Aq-D2 cosmological box. From top to bottom: Number of disc, bulge and halo particles, disc mass, bulge mass, halo virial mass, halo virial radius, halo NFW scale radius, halo Hernquist scale radius, bulge scale radius, disc scale length, disc scale height, and, additionally, the corresponding number of satellites in the INTERACTION simulation.

N_{disc}	1×10^7
N_{bulge}	5×10^5
N_{halo}	4×10^6
M_{disc}	$3.4 \times 10^{10}\ \mathrm{M_\odot}$
M_{bulge}	$0.9 \times 10^{10}\ \mathrm{M_\odot}$
M_{200}	$1.77 \times 10^{12}\ \mathrm{M_\odot}$
r_{200}	$242.8\ \mathrm{kpc}$
r_{s}	$25.91\ \mathrm{kpc}$
a	$43.90\ \mathrm{kpc}$
a_b	$0.35\ \mathrm{kpc}$
h	$2.8\ \mathrm{kpc}$
z_0	$0.277\ \mathrm{kpc}$
N_{sat}	23

(2.29), where the η parameter corresponds to `dEta` in the parameter file for CHANGA. Here, I chose `dEta`$= 0.3$, high enough to avoid to excessively slow down the simulations.

Regarding the choice of the softening, if it is chosen too small, according to Equation (2.29) then 1) the timestep is decreased by a factor $\sqrt{\epsilon}$; 2) the acceleration that a particle suffers may be larger because of the smaller range of force softening, thus contributing to decrease the timestep by another factor $1/\sqrt{a}$. If the softening is chosen too high, there is on the contrary more inaccuracy in the time integration (the timesteps are larger) and the gravitational force is softened at a higher range, with a consequent loss of accuracy in its calculation.

CHANGA was the first code that I used for the RELAX, ISOLATION and INTERACTION simulations, therefore it was the code that I used to calibrate the choice of the softening values, depending on the consequent integration speed of the code. I chose a softening length $\epsilon = 100\ \mathrm{pc}$ for disc, bulge and satellite particles and $\epsilon = 200\ \mathrm{pc}$ for the halo particles. For the halo, the choice of a softening $\epsilon = 200\ \mathrm{pc}$ is optimal to avoid spurious kicks on the halo particles.

For the disc, bulge and satellite particles, I had initially opted for a smaller softening, $\epsilon = 40\ \mathrm{pc}$ instead of $100\ \mathrm{pc}$. This choice was done to get as close as possible to the vertical force resolution of the disc in **MJ16** with SUPERBOX-10, which was set to $40\ \mathrm{pc}$. For the halo in I initially chose a higher value of the softening, $\epsilon = 500\ \mathrm{pc}$, to counterbalance the higher computational time required for the disc, bulge and satellite particles integration.

Since in CHANGA the softening spline kernel reproduces the Newtonian force at two times the average value of the softening of two given particles, then to obtain a disc vertical force resolution of $40\ \mathrm{pc}$ the choice of the softening of the disc particles should have been set to $20\ \mathrm{pc}$. However, already choosing the disc, bulge, and satellite particle softening to be $\epsilon = 40\ \mathrm{pc}$, the simulations were

slower by a factor 1.75 than the corresponding ones with $\epsilon = 100\,\text{pc}$ for the disc, bulge and satellite particles and $\epsilon = 200\,\text{pc}$ for the halo particles.

Thus, a choice of $20\,\text{pc}$ in the disc was excluded because it would have most likely led to an even slower integration, and I opted for $\epsilon = 100\,\text{pc}$ in the disc, bulge and satellites, to gain this 1.75 speed-up factor and reduce the computational time. Also, I note that the value of $\epsilon = 100\,\text{pc}$ is below the initial tidal radii r_{tid} of the satellites (satellite 17 of the Aq-D2 set-up has the smallest tidal radius in the simulation, $r_{\text{tid}} = 1.5\,\text{kpc} \gg 0.1\,\text{kpc}$), and therefore the satellites are force-resolved within their tidal radii.

The base (i.e. the highest) timestep for the construction of the block hierarchy was chosen to be `dDelta`$= 10\,\text{Myr}$, small enough to be conveniently below the dynamical timescale of the evolution of the MW, which is of order ~ 100 Myr. The resulting timesteps, given the division in rungs of the block hierarchy, reach an order comparable to $\Delta t = 0.1\,\text{Myr}$ in **MJ16** with Superbox-10.

The simulations performed by **MJ16** were N-body runs without any additional recipes for gas hydrodynamics, gas cooling, SF and feedback. Therefore, I ran the simulations with ChaNGa in N-body mode only, and I switched off all the recipes to simulate additional physics.

Gadget-2: parameters used in the runs

Given that in Gadget-2 the timestep for particles is defined as in Equation (2.32), then to have timesteps with a similar order of magnitude as the ones in ChaNGa, η (`ErrTolIntAccuracy`) was set to 0.219 in the parameter file. The value of the opening angle parameter (`ErrTolTheta`) for the first tree walk in each simulation was set to 0.55 as in ChaNGa. As for the revised opening criterion employed in the subsequent timesteps, I chose for the tolerance parameter α the default value `ErrTolForceAcc` $= 0.005$. Regarding the softening, I chose the same values as in ChaNGa, i.e. $\epsilon = 100\,\text{pc}$ for disc, bulge and satellite particles, and $\epsilon = 200\,\text{pc}$ for the MW halo particles.

Before choosing these values of softening, I evaluated the option of rescaling the softening values adopted in ChaNGa by a factor 1.4 smaller, in order to obtain the corresponding softening values for Gadget-2. This, in principle, finds justification in the different ranges adopted to recover the Newtonian force in ChaNGa and Gadget-2. In fact, as I showed in Sections 2.6.2 and 2.6.3, the Newtonian force in ChaNGa is recovered within two times the average softening of the two interacting objects (particle or node), while in Gadget-2 it is recovered within 2.8 times the larger of the softening values of the two interacting objects (particle or node).

Thus, even if choosing $\epsilon = 100/1.4\,\text{pc} \sim 71.4\,\text{pc}$ for disc, bulge and satellite particles in Gadget-2 would allow to recover the Newtonian force at the same scale ($200\,\text{pc}$) as in ChaNGa for disc-bulge-satellite particle interactions, the same rescaling could not be granted already for the interaction of these particles with the halo particles and with nodes containing different kinds of particle. This motivated my final choice of adopting the same softening values as in ChaNGa. This choice implies a softening of the force acting on similar

scales in CHANGA and GADGET-2 (few hundreds of pc) and, as I show later in this section, it did not affect the final results in the benchmark and their overall similarity.

Last, for the choice of the maximum timestep $\Delta t_{\max}$ I adopted a value `Max-SizeTimestep` $= 10$ Myr. This is the same value of the base timestep that I adopted in CHANGA, and it is again conveniently smaller than the dynamical timescale of the MW galaxy. Also for GADGET-2 the resulting distribution of particle timesteps in the block hierarchy allows for time synchronisations of the same order as the 0.1 Myr of **MJ16**.

Being this an N-body benchmark, also with GADGET-2 I did not need to switch on cooling, SF and feedback recipes. Therefore, I used the code in N-body mode only.

Computer cluster

The cluster used to run the simulations was the `BwForCluster`, a collaboration of the Universities of Heidelberg and Mannheim [8]. I found the choice of running the simulations in parallel with 48 CPUs (3 nodes, 16 processors per node) convenient to give results in a reasonable time of ~ 1 week per simulation both with CHANGA and GADGET-2. With a higher number of processors, the simulations in CHANGA were producing errors that terminated them[9]. Therefore, it is clear now why the choice of a softening $\epsilon = 40$ pc for disc, bulge and satellite particles was inconvenient: to compensate for the higher workload in the integration, I could have used more processors, but this was not possible due to these crashes.

Selection of the snapshots and coordinate rescaling

Even if **MJ16** originally run each simulation for at least 2 Gyr, in the case of this benchmark I run each simulation for 1 Gyr. This choice, given the typical dynamical timescales of MW-like galaxies of a few hundred Myr, is enough to compare the isolated evolution of the MW model and its interaction with the satellites in the different codes, and it is enough to capture significant divergences in the behaviour of the codes.

I have stored outputs every 100 Myr in the RELAX simulation for CHANGA and GADGET-2 to compare the energy, angular momentum and momentum conservation with SUPERBOX-10. For the analysis of the disc evolution in the RELAX simulation, I took snapshots only every 500 Myr, enough to make a general comparison on the secular evolution of the MW disc between the different codes. For the INTERACTION and ISOLATION simulations, I only considered the final snapshot to directly compare the result on disc thickness and heating in CHANGA and GADGET-2 with the results of **MJ16** in SUPERBOX-10.

---

[8]See the page http://wiki.bwhpc.de/e/BwForCluster_User_Access for more information.

[9]This may be due to the version of `Charm++` that I employed at the time of the test, that may have not been stable. For practical reasons I did not investigate this problem more in detail, giving priority to start the simulations in CHANGA with a convenient number of CPUs.

Before calculating any disc property from the outputs of CHaNGa and Gadget-2, and in order to compare it with the results of **MJ16**, I have rescaled the coordinates of the disc particles for the MW density centre position and velocity[10], and I have rotated the disc particles in order to have the angular momentum of the disc aligned with the z-axis. This procedure was done to follow the calculations of **MJ16** and to avoid biases in the benchmark.

2.7.2 Results for the evolution in isolation

I first show how CHaNGa and Gadget-2 compare with Superbox-10 in reproducing the isolated evolution of the MW disc in the RELAX simulation.

CHaNGa: results for the isolated evolution of the Milky Way

I first discuss the results obtained with CHaNGa for the isolated evolution of the MW model. In the RELAX simulation, I have studied some kinematic and dynamical quantities of the disc to check how they evolved in the different codes.

The Toomre Q parameter for stellar discs (Toomre 1964) describes the stability of stellar discs against gravitational collapse and puts in relation their surface density Σ with the epicyclic frequency k of stellar orbits and the radial velocity dispersion σ_R,

$$Q = \frac{\kappa \sigma_R}{3.36 G \Sigma} \, . \tag{2.33}$$

A disc with hot kinematics in the radial direction or with high stellar epicyclic frequency is less prone to instabilities, that otherwise can manifest in the form of a bar or of spiral structures. A Fourier analysis of the disc mass distribution can unveil these features, as I will discuss in Chapter 4, showing the numerical study of the MW bar. A massive disc, on the contrary, tends to develop these instabilities. The epicyclic frequency was calculated as in **BT08**,

$$\kappa = \sqrt{R \frac{d\Omega^2}{dR} + 4\Omega^2} \, , \tag{2.34}$$

where Ω^2 is the squared angular frequency, obtained from the gravitational potential Φ as

$$\Omega^2 = \frac{1}{R} \frac{d\Phi}{dR} \quad . \tag{2.35}$$

This is slightly different than what is done in the case of **MJ16**, where the acceleration of particles was employed. The derivatives appearing in the last two

---

[10]The method to calculate the density centre is based on the one adopted by P. Berczik (Main Astronomical Observatory, Kiev, Ukraine). It consists in shrinking iteratively a sphere that initially contains all the particles of the MW. This is done by calculating at each iteration the centre of mass of the particles inside the previous sphere, and then in centring the new shrunken sphere on this centre of mass. This method therefore excludes, iteration after iteration, all the particles that do not have any more weight in determining the location of the densest region of the system. The iteration can be stopped when a desired minimum number of particles or a desired minimum radius are reached.
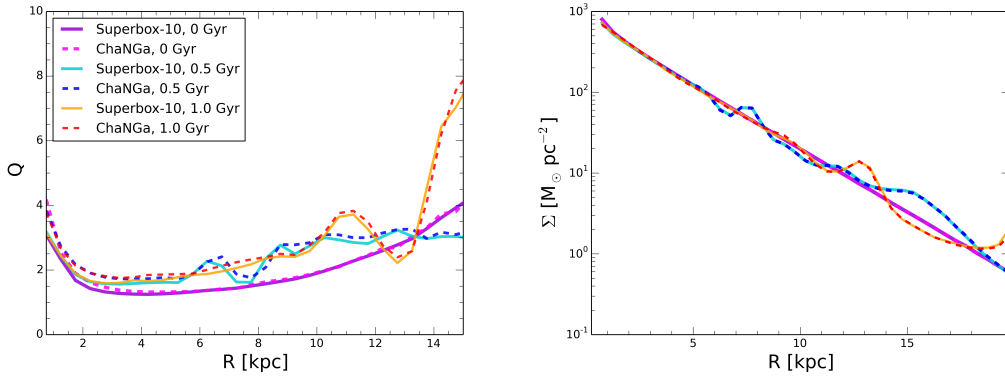
Figure 2.2: Radial profiles of the MW disc Q parameter (left panel) and surface density (right panel), at times $t = 0$, 0.5 and 1 Gyr, for the simulation RELAX in SUPERBOX-10 and CHANGA. Colour and line codes explained in the label in the left panel.

equations were substituted with discrete differences between contiguous radial bins. I chose a division in 80 equally spaced radial bins, two times the binning chosen by **MJ16**. This binning is enough to obtain a smooth profile of Q. The results are similar in the two codes through time (left panel of Figure 2.2). Particularly, the Q parameter has a minimum between 1 and 2 that increases in time, approaching ~ 2 towards the end of the simulation. As a matter of fact, this disc model does not develop any bar instability through its evolution, as was already visible in **MJ16**.

The surface density appears to behave similarly in the two codes (right panel of Figure 2.2). Both simulations show the propagation of a density perturbation in the disc, that undergoes relaxation in the whole isolated evolution. This density perturbation propagates outwards in time and causes the surface density to oscillate around the initial exponential profile. This is visible from the crest present at $t = 0.5$ Gyr at around 7 kpc of GCd (cyan full line for SUPERBOX-10, blue dashed line for CHANGA), which after other 0.5 Gyr moves to $12 - 13$ kpc of GCd (orange full line for SUPERBOX-10, red dashed line for CHANGA).

Last, I also show the average radial, tangential and vertical velocities and their dispersion values for the case of CHANGA in comparison to SUPERBOX-10 (top, central and bottom panels of Figure 2.3, respectively; the average velocities are on the left panels, the dispersion values are on the right panels). In both codes, the outward propagation of the density wave in the disc has effects on the radial, tangential and vertical velocity profiles, which present crests that, similarly to the surface density, propagate towards the outside. This may happen at the expense of the tangential velocity, which is lowered down in time, due to the redistribution of part of the kinetic energy associated to the tangential motions into kinetic energy associated to radial motions. The numerical MW model discussed here was realised by **MJ16** with $\sigma_R^2 \sim \sigma_\phi^2$. This condition favours transfer of kinetic energy from the tangential to the radial direction throughout the evolution of the disc.

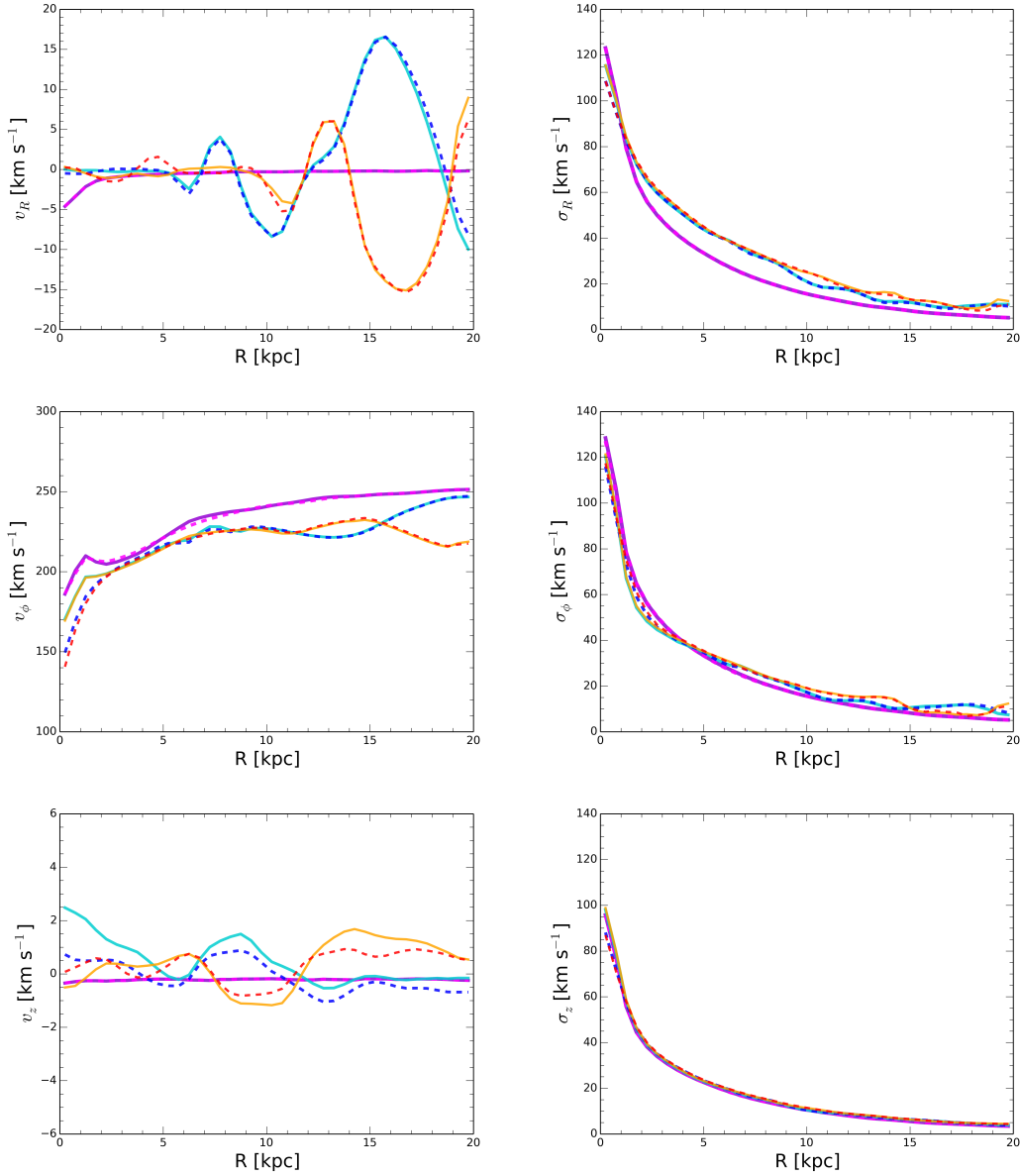Additionally, the fact that the radial velocity dispersion profile (top right

Figure 2.3: From top to bottom: MW disc average radial, tangential and vertical velocity profiles (left panels) and the corresponding velocity dispersion profiles (right panels), at times $t = 0$, 0.5 and 1 Gyr, for the simulation RELAX in SUPERBOX-10 and CHANGA. Colour and line codes as in Figure 2.2.

.

panel) shows also in CHANGA an increase in time out of $1-2$ kpc of GCd, specifically preventing bar formation, confirms that this surface density wave and the increase of the energy budget invested in radial motions are a numerical artefact of the initial MW set-up generated with GalIC. Therefore, this is not a numerical feature introduced by SUPERBOX-10, that was the code originally employed to simulate the MW evolution studied in **MJ16**.

In general, this analysis confirms that the evolution of the relaxing MW disc

in CHANGA is similar to what was found by **MJ16**. Perturbations on the disc surface develop within a similar timescale and the bar is a missing feature in both simulations. Also, the exponential density profile of the disc was built by **MJ16** to follow the observations of the MW and does not change drastically from equilibrium, if we exclude these perturbations.

GADGET-2: results for the isolated evolution of the Milky Way

I have performed with GADGET-2, like I did for CHANGA, the same analysis of the evolution in time of the Q parameter, of the surface density profile, of the $z-$, $r-$ and $\phi-$velocities, and of their dispersion values. Again, I compared these results to the results obtained in SUPERBOX-10 by **MJ16**.

In the RELAX simulation, the Q parameter and the surface density profile behave and evolve very similarly using GADGET-2 and SUPERBOX-10 (Figure 2.4, left and right panel, respectively). The evolution of the velocity and velocity
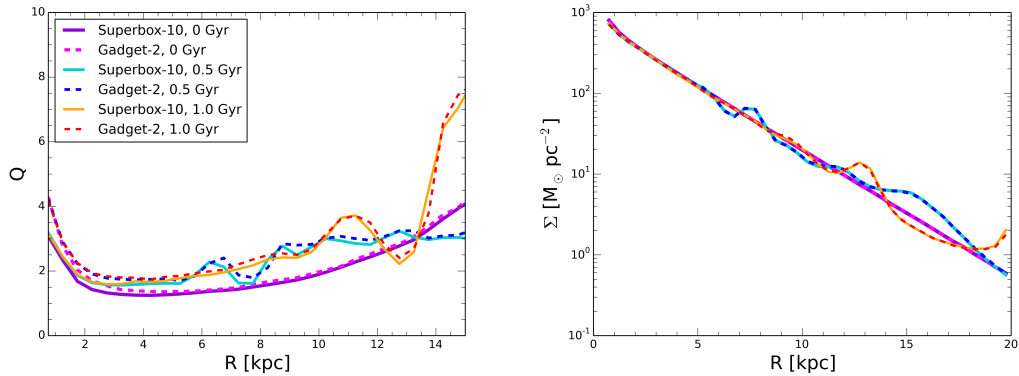
Figure 2.4: Radial profiles of the MW disc Q parameter (left panel) and surface density (right panel), at times $t = 0$, 0.5 and 1 Gyr, for the simulation RELAX in SUPERBOX-10 and GADGET-2. Colour and line codes explained in the label in the left panel.

dispersion profiles is similar as well (Figure 2.5).

From this comparison, I can confirm that the density wave that propagates radially in the MW disc simulated in SUPERBOX-10 and CHANGA is present also in the case of GADGET-2, where the increase of the radial velocity dispersion at the expense of the tangential velocity profile finds as well confirmation. This reinforces the idea, discussed already for the case of CHANGA, that this whole effect is a consequence of the MW ICs, and it is not a peculiar numerical effect introduced neither by a PM code like SUPERBOX-10, nor by the tree codes CHANGA and GADGET-2.

2.7.3 General comparison of the evolution in interaction with the satellites

Now, I show and discuss the results obtained studying the evolution of the MW disc interacting with the satellites in the INTERACTION simulation using the codes CHANGA and GADGET-2, in comparison to the results of **MJ16** obtained
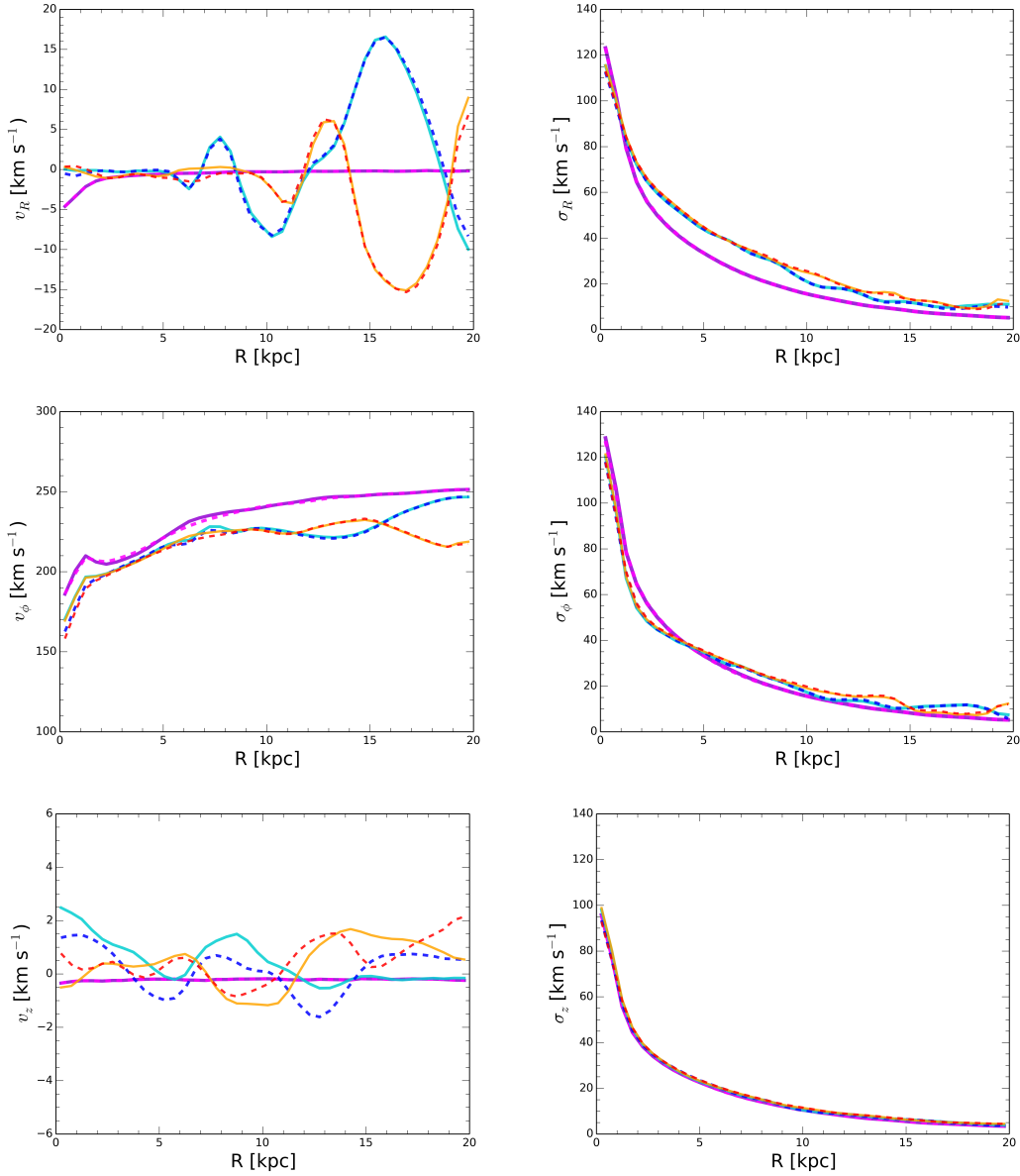
Figure 2.5: From top to bottom: MW disc radial, tangential and vertical velocity profiles (left panels) and the corresponding velocity dispersion profiles (right panels), at times $t = 0$, 0.5 and 1 Gyr, for the simulation RELAX in SUPERBOX-10 and GADGET-2. Colour and line codes as in Figure 2.4.

using the code SUPERBOX-10.

Following **MJ16**, I have calculated the disc radial profiles of the average vertical position of the particles, $< z >$, which is an indicator of the vertical average displacement of the disc. Also, I calculated z_{rms}, which is an indicator of the disc vertical thickening, and σ_z^2, which indicates the degree of vertical heating of the disc. Additionally, I have calculated $< z >$ and z_{rms} for the ISOLATION simulation as well, in order to make a comparison between the cases of evolution in inter-

action and evolution in isolation. For the calculation of σ_z^2, instead, I compared the results from the three codes in the INTERACTION simulation with the data provided at solar GCd ($R_0 = 8$ kpc) by Holmberg et al. (2009), like previously done in **MJ16**.

Regarding $<z>$, the final profile is overall similarly reproduced by the three codes. In particular, in the INTERACTION simulation, the outer downward-oriented warp of the disc at 1 Gyr, that originally was found in **MJ16**, is similarly captured in CHANGA and GADGET-2, as showed in Figure 2.6 (full lines). This confirms that the satellites impacting on the MW disc are able to produce a warp on the external regions of the disc. Also, the similar effect of the satel-
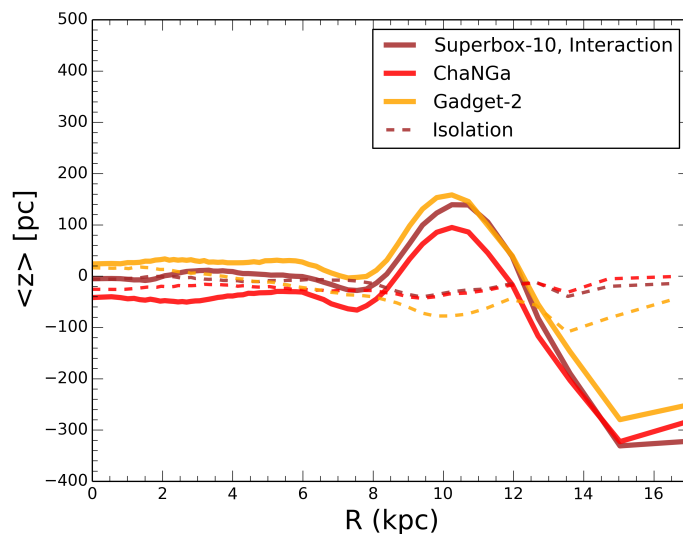
Figure 2.6: $<z>$ profile in the simulations INTERACTION and ISOLATION in all the three codes, at time $t = 1$ Gyr. Colour and line codes explained in the label.

lites on the disc warp is evident if compared, for the three codes, against the corresponding results on the $<z>$ profile at the same time but for the ISOLATION case (dashed lines). The warp of the isolated disc at around 14 kpc of GCd is smaller in CHANGA and SUPERBOX-10 than in GADGET-2, by a difference of ~ 70 pc. However, this difference is confined to this region only, therefore it has no relevance in this analysis, overall.

I then compared the disc thickness, z_{rms}, for the three codes in ISOLATION and INTERACTION. I show the result in Figure 2.7. Using GADGET-2 and CHANGA, I found a similar, final disc thickness as in SUPERBOX-10. Only in the inner regions there is divergence between the three codes. The higher thickness close to the MW disc centre is reached by CHANGA, with values of $z_{\mathrm{rms}} = 360$ pc, $50 - 70$ pc more than in GADGET-2 and SUPERBOX-10.

Overall, the fact that in SUPERBOX-10 the final disc thickness profile is higher in the case of the INTERACTION simulation than in the case of the ISOLATION simulation is confirmed in CHANGA and GADGET-2, where the interaction of the MW disc with the satellites produces again more flaring of the disc than in the

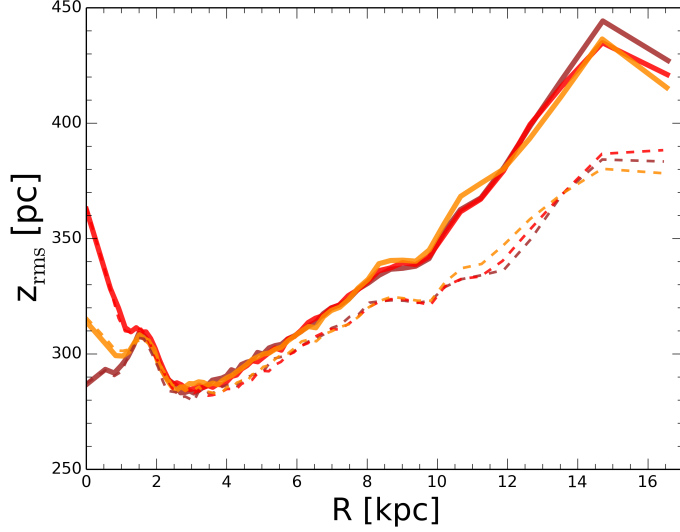ISOLATION case. This is particularly evident in the outer regions of the disc.

Figure 2.7: z_{rms} profile in the simulations INTERACTION and ISOLATION in all the three codes, at time $t = 1$ Gyr. Colour and line codes as in Figure 2.6.

Finally, I show in Figure 2.8 the comparison of the disc heating in the IN-TERACTION simulation, i.e. $\sigma_z^2(t) - \sigma_z^2(0)$, between the three codes. In this case I compared the heating, i.e. the increase of the disc vertical velocity dispersion from the initial time, and not the value at the final time, in order to compare this increase to the observational data provided by Holmberg et al. (2009) at the solar GCd of 8 kpc. Based on the observation of positions and motions of several stars in the solar neighbourhood, Holmberg et al. predicted an increase in the squared vertical velocity dispersion of disc stars equal to 72 km^2 s^{-2} Gyr^{-1}. This means that, after 2 Gyr, starting from a vertically cold disc, one should expect a final increase in the vertical velocity dispersion $\sigma_z^2(t) - \sigma_z^2(0) = 144$ km^2 s^{-2}.

This was the observational result that **MJ16** compared with the numerical one obtained in their simulations. **MJ16** concluded that in the proximity of the GCd of the Sun the satellites cannot heat the disc at a level that is able to reproduce the value predicted by Holmberg et al. (2009), not even when accounting for a delay of 0.5 Gyr in the interaction process between the MW and its satellites.

In the context of this benchmark, I considered the final comparison value of vertical velocity dispersion $\sigma_z^2 = 72$ km^2 s^{-2}, since my runs reproduced only 1 Gyr of interaction. For additional comparison, I also considered the value of $\sigma_z^2 = 36$ km^2 s^{-2} accounting for the case of 0.5 Gyr delay in the interaction of the MW with the satellites. In all the three codes, the thickening cannot match the predicted value in the solar neighbourhood with any of the codes (Figure 2.8). CHANGA gets relatively closer to the value with 0.5 Gyr delay predicted after 1 Gyr by Holmberg et al. (2009), but cannot really match this constraint. Therefore, the results on the final disc thickness and
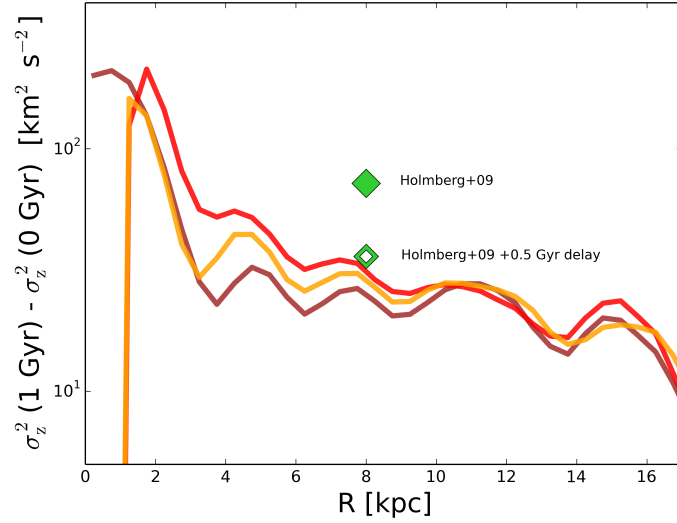
Figure 2.8: $\sigma_z^2(t) - \sigma_z^2(0)$ profile for the simulation INTERACTION in all the three codes, at time $t = 1$ Gyr. Colour codes as in Figure 2.6. Additionally, the values of Holmberg et al. (2009) for the solar neighbourhood are reported with an empty diamond and with a filled diamond. The empty diamond accounts for the case of 0.5 Gyr delay in the interaction with the satellites, the filled diamond accounts for no delay in the interaction.

heating obtained with CHANGA and GADGET-2 are in line with the previous ones of **MJ16** obtained with SUPERBOX-10. As an additional note, in CHANGA and GADGET-2 the inner heating profile turns towards negative values (not displayed in the logarithmic scale of Figure 2.8). This is in contrast with what is observed in SUPERBOX-10 for the same region.

This should be compared with what I showed before in Figure 2.7 about the inner higher values of $z_{\rm rms}$ in CHANGA and GADGET-2, in comparison to SUPERBOX-10. A lack of accuracy in the calculation of positions and velocities of the density centre can be excluded, because then one would expect systematic discrepancies in all the results discussed in the benchmark. Rather, it is plausible that the softening values for the bulge and disc particles employed in CHANGA and GADGET-2 reduce the effects of the gravitational potential in the inner regions of the disc, where there is much more resolution in SUPERBOX-10 (~ 20 pc of vertical force resolution, due to the inner PM grid employed to better resolve the high-density region of the MW). In CHANGA and GADGET-2 the softening spline kernels act on a range of $200 - 300$ pc, which may be of non-negligible impact in a high-density region like the centre of the MW and the bulge. The softened forces that act on the particles make them less gravitationally bound to the system, and hence may cause the inner disc to vertically thicken more than in SUPERBOX-10 and to cause less heating of the vertical motions.

In conclusion, it is plausible that force resolution is the real cause of these differences between the three codes, that however are confined only in the inner MW disc. Apart from this, by means of the analysis above, I can conclude

that the three codes similarly reproduce the impact of the MW satellites on the Galactic disc, and that these results find confirmation when compared with the case of isolated evolution of the MW disc.

2.7.4 Conservation of energy, angular momentum, and momentum

Now, I discuss the results based on a comparison of the accuracy in SUPERBOX-10, CHANGA and GADGET-2. I checked the relative variation (with respect to the initial value) of the MW total energy, of the total angular momentum components, and of the centre of mass position and velocity coordinates. I used the RELAX simulation to perform this analysis.

Energy conservation and angular momentum conservation

The total energy was calculated as

$$E_{\rm tot} = E_{\rm kin} + E_{\rm pot} \,, \tag{2.36}$$

where $E_{\rm kin}$ is the total kinetic energy of the system, calculated as

$$E_{\rm kin} = \sum_{i=1}^{N} \frac{1}{2} m_i v_i{}^2 \,, \tag{2.37}$$

and $E_{\rm pot}$ is the total potential energy, calculated as

$$E_{\rm pot} = -\sum_{i=1}^{N} \sum_{j \neq i}^{N} \frac{G m_i m_j}{2 r_{ij}} \,. \tag{2.38}$$

Here, N is the number of particles, m_i is the mass of the $i-$th particle of the system, r_{ij} is the distance between the i-th and j-th particle. The angular momentum vector is

$$\vec{L}_{\rm tot} = \sum_{i=1}^{N} = m_i \vec{r}_i \times \vec{v}_i \quad . \tag{2.39}$$

I calculated the relative displacement in energy, $|\Delta E_{\rm tot}/E_{\rm tot}(0)|$, and in the angular momentum components, $|\Delta L_{{\rm tot},x,y,z}/L_{{\rm tot},x,y,z}(0)|$, with respect to their initial values.

The energy conservation comparison returns no systematic differences between the three codes (left panel of Figure 2.9), and there is no code with a better behaviour through the whole simulation. However, it can be observed that the relative displacement of the total energy is overall good, being always lower than 1% for all the three codes.

A check on the angular momentum variation shows that in CHANGA the three components of the total angular momentum conserve overall better than in SUPERBOX-10 and GADGET-2. However in the two latter codes the variation of $\vec{L}_{\rm tot}$ in the in the x- and y-directions is still no more than $\sim 2-3\%$ at the end of the simulation.
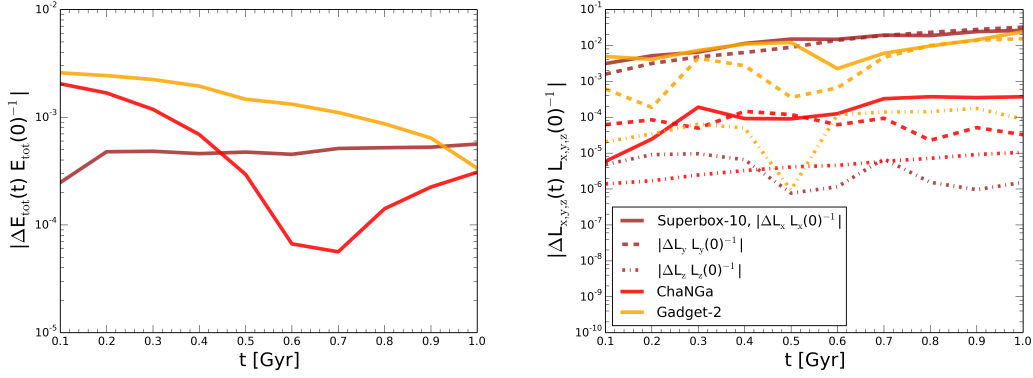
Figure 2.9: *Left panel:* Absolute value of the relative variation of E_{tot} for the simulation RE-LAX in all the three codes. Colour codes as in Figure 2.6. *Right panel:* Absolute value of the relative variation of the three coordinate components of $\vec{L}_{\text{tot}}$ for the same simulation and in all the three codes. Colour codes as in Figure 2.6. Full lines are for the x-component, dashed lines are for the y-component and dot-dashed lines are for the z-component.

Momentum conservation

I then compared the momentum conservation in the three codes, by means of checking the variation of the centre of mass coordinates and velocity components with respect to the initial values. In absence of external forces, the centre of mass of a system should have constant velocity (equal to the initial one) and so it should move with uniform straight motion. Divergences from this behaviour are indicative of errors and inaccuracies introduced by the codes when integrating the system in time.

The analysis performed on the three codes shows that the centre of mass has the strongest divergences from uniform motion in GADGET-2, particularly in the z-direction (left panel of Figure 2.10). Also regarding the velocity, in CHANGA the centre of mass has the least variation of velocity (right panel of Figure 2.10), and again GADGET-2 performs as the worse of the three codes. In Section 2.8 I discuss how the integration scheme of GADGET-2 limits momentum conservation and I show how this problem is solved in GADGET-4.

2.7.5 Comparison on the computational speed

I now discuss the performance, in terms of computational speed, in the codes CHANGA, GADGET-2 and SUPERBOX-10. I could not be provided precise details about the computational speed in SUPERBOX-10 for the simulations performed in **MJ16**. I was only given some order-of-magnitude estimates of the time required to run the simulation with satellites, therefore I can only report a general, order-of-magnitude comparison of the performances.

With reference to the INTERACTION simulation, **MJ16** spent ~ 2.5 weeks, i.e. $17-18$ days, in order to run the simulation for $2\,$Gyr in SUPERBOX-10. Assuming on average a constant rate of timestep advancement and of snapshot writing, this means ~ 9 days to run the simulation for $1\,$Gyr. However, **MJ16** used 32 cores instead of 48, so additionally assuming linear scaling with the number
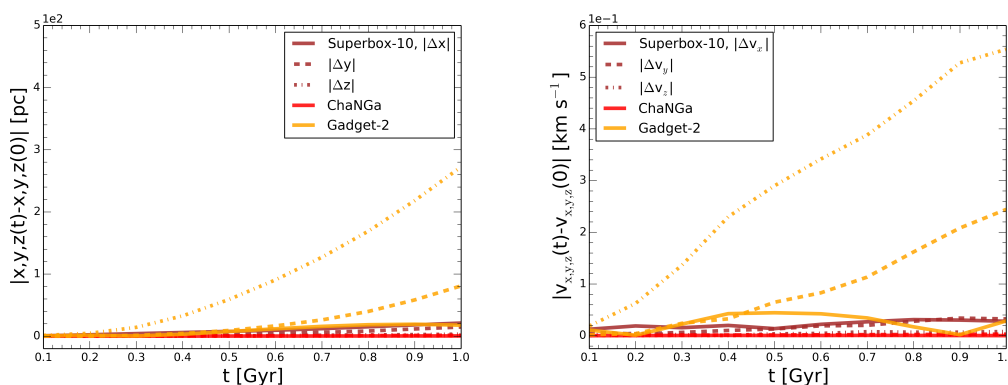
Figure 2.10: Absolute value of the variation of the centre of mass coordinates (left panel) and of the centre of mass velocity components (right panel) for the simulation RELAX in all the three codes. Colour codes as in Figure 2.6. Line codes for the three coordinate directions as in the right panel of Figure 2.9.

of processors, this would correspond to no more than 6 days if using 48 CPUs. Multiplying this in terms of hours and by the 48 CPUs, it means ~ 6900 CPU hours of total computational time. Assuming that the speed is similar for the case of the RELAX and ISOLATION runs, this is also an estimate of the CPU hours for the RELAX simulation in **MJ16**.

For comparison, in the case of CHaNGa, it took me $7-8$ days of calculations to run each simulation with 48 CPUs. This translates into ~ 8600 total CPU hours with CHaNGa. GADGET-2 was run with the same number of processors as CHaNGa. It took me $4-5$ days to run each simulation, which translates into ~ 5200 CPU hours with GADGET-2.

Among all the codes, given the same ICs, CHaNGa is the most demanding one in terms of computational time, while GADGET-2 is the fastest one. However, as I showed, CHaNGa returns in general more accuracy in the angular momentum calculation and, most of all, it grants better momentum conservation than SUPERBOX-10 and GADGET-2.

2.8   Moving from GADGET-2 to GADGET-4

From the benchmark performed on the MW N-body simulations of **MJ16**, based on the Aq-D2 set-up, I have showed that GADGET-2 compares well with more modern codes like CHaNGa and SUPERBOX-10. Also, like for the other two codes, for GADGET-2 the conservation of the total energy and angular momentum are granted with a relative error less than 1% and $2-3\%$, respectively. This is an indication that the GADGET family of N-body codes is a good choice for the study of stellar dynamics and satellite dynamics in numerical simulations of the MW environment.

However GADGET-2 does not conserve momentum as well as CHaNGa and SUPERBOX-10. Therefore the goal of this section is to show how the code GADGET-4 is promising in terms of improvements of momentum conservation. This is due to some aspects and features introduced by the code.

2.8.1 Fast multipole method and revised timestepping

Among the features that it implements, GADGET-4 makes use of the additional fast multipole method (Greengard & Rokhlin 1997). Using this method, the calculation of the force acting on particles is manifestly momentum conserving, with residual force errors only at machine-precision level (**S20**).

Additionally, GADGET-4 makes use of a revised hierarchical timestepping criterion with respect to the one employed in GADGET-2. GADGET-2 employs the KDK leapfrog method illustrated before in this thesis in Section 2.3.3, coupling it with a hierarchical timestepping that does not allow the code to conserve momentum. In fact, when updating the active particles by calculating the force acting on them, their interaction with the passive particles is still calculated, while for the passive particles the force is not calculated. The total force resulting from this is asymmetric, with a lack of conservation of the momentum of the system. This explains the behaviour of the centre of mass seen in Figure 2.10 for the simulation RELAX in GADGET-2.

The new scheme implemented in GADGET-4 solves this problem. In fact, while keeping a KDK leapfrog integration for particles and a hierarchical distribution of timesteps, the code now allows only active particles to feel the mutual forces and interactions, neglecting the contribution from the passive particles (**S20**). The resulting, total force calculation is symmetric and makes the code manifestly momentum conserving in the local time integration of the active particles, reducing the total force error to the residual forces only coming from the calculation of the tree.

2.8.2 Numerical test and simulation set-up

To prove the validity of the revised hierarchical timestepping for momentum conservation in GADGET-4, I have performed with the code a simulation, with the same ICs as in the RELAX case presented in Section 2.7 (i.e. a run of an isolated MW model starting from an initial axisymmetric set-up, and consisting of live disc, live bulge and live halo). I have switched on the HIERARCHICAL_GRA-VITY option for allowing the revised timestepping criterion of GADGET-4, adopting the same value of tolerance α on the force error, i.e. ErrTolForceAcc$= 0.005$. Also, I set the η accuracy parameter for the timpestep calculation to a value ErrTolIntAccuracy$= 0.0219$, i.e. the same as in GADGET-2. I have employed the same value of the initial opening angle θ as before, i.e. ErrTolTheta$= 0.55$.

GADGET-4 runs in parallel using MPI prescriptions. I have used again the BwForCluster to run the simulation with 48 CPUs. I have run the RELAX simulation for 1 Gyr like in the other cases.

2.8.3 Results on the disc properties

I show first the results with GADGET-4 on the evolutionary properties of the MW disc already showed for the RELAX simulation before. I compared them to GADGET-2. I show the same results on the Q parameter and on the surface density profile for the isolated disc from $t = 0$ to $t = 1$ Gyr in Figure 2.11,

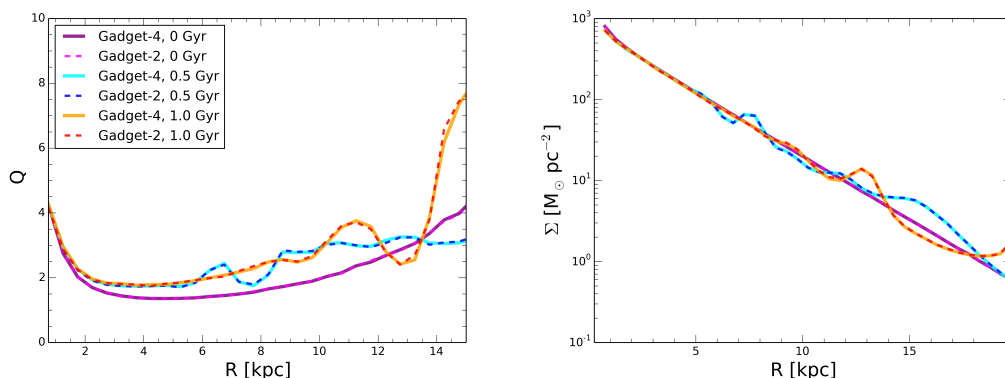similarly to what I showed for instance in Figure 2.2. In Figure 2.12 I show the

Figure 2.11: Radial profiles of the MW disc Q parameter (left panel) and surface density (right panel), at times $t = 0, 0.5$ and 1 Gyr, for the simulation RELAX in GADGET-4 and GADGET-2. Colour and line codes explained in the label in the left panel.

results for the radial, tangential and vertical velocity profiles in the disc, as well as the corresponding velocity dispersion profiles, similarly to what I showed in Figure 2.3.

Figure 2.11 and Figure 2.12 suggest that GADGET-4 produces results in line with the ones from GADGET-2 (and therefore with the other two codes). Only some discrepancies are found in the calculation of the vertical average velocity profile v_z. However, given the very low range in velocities under consideration (between -2 and 2 km s^{-1}), and given the fact that all the other profiles show strong agreement, this does not pose problems in the light of the comparison.

Given the good agreement between the two codes, this first test does not need further discussion. The main reason behind it in fact was to show that the overall dynamics and kinematics of the isolated evolution of the MW presented before with CHANGA, SUPERBOX-10 and GADGET-2 finds confirmation in GADGET-4.

2.8.4 Conservation of energy, angular momentum, and momentum

I calculated again the total energy and the total angular momentum of the isolated MW in GADGET-4, to compare their conservation with the previous results of GADGET-2. In Figure 2.13 I show the results of this calculation. There is no systematic difference in the energy and angular momentum conservation between the two codes. Also in GADGET-4, the variation of angular momentum, specifically in the x- and y-directions, while not as good as seen previously in CHANGA, is still reasonably confined below $\sim 2 - 3\%$.

As for the momentum conservation, in Figure 2.14 I show the variation of the centre of mass coordinates and velocity in the simulation RELAX in GADGET-4 and GADGET-2. Remarkably, GADGET-4 shows an improvement in momentum conservation. In GADGET-4 the variation of the centre of mass position and velocity is much smaller, in comparison with the displacement that is found in
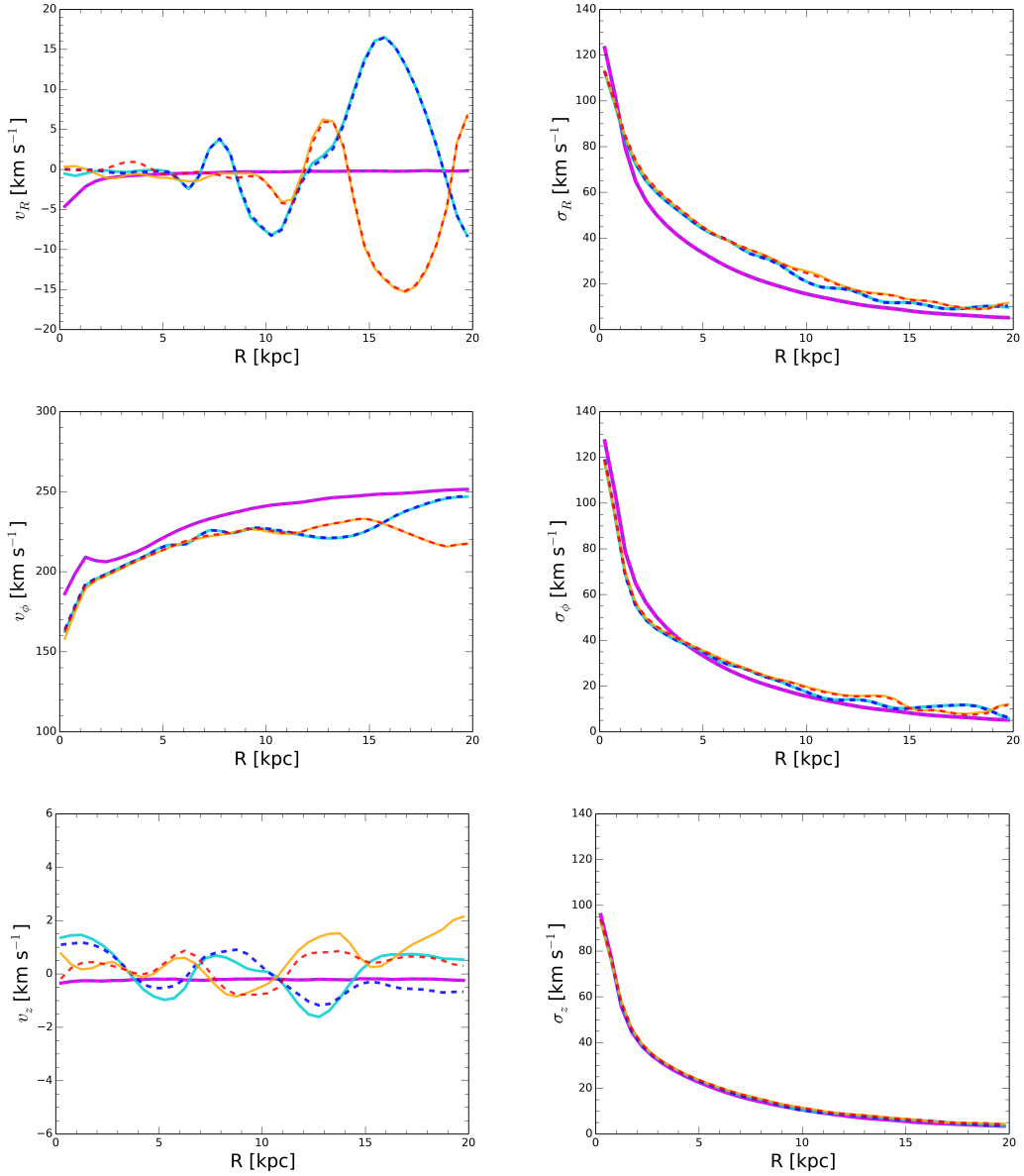
Figure 2.12: From top to bottom: MW radial, tangential and vertical velocity profiles (left panels) and the corresponding velocity dispersion profiles (right panels), at times $t = 0$, 0.5 and 1 Gyr, for the simulation RELAX in GADGET-4 and GADGET-2. Colour and line codes as in Figure 2.11.

GADGET-2. Also, GADGET-4 conserves momentum in a similar way to what was showed in the case of CHANGA in Figure 2.10.

Last, I compared the performance of GADGET-4 and GADGET-2 in terms of the total computational time in the simulation RELAX. It took ~ 4 days to run the simulation with GADGET-4, i.e. multiplying by 24 hours and the 48 cores employed it means a total of ~ 4600 CPU hours. Thus, the speed of GADGET-4 is better than the one of GADGET-2, given the ~ 5200 CPU hours required by the latter code.
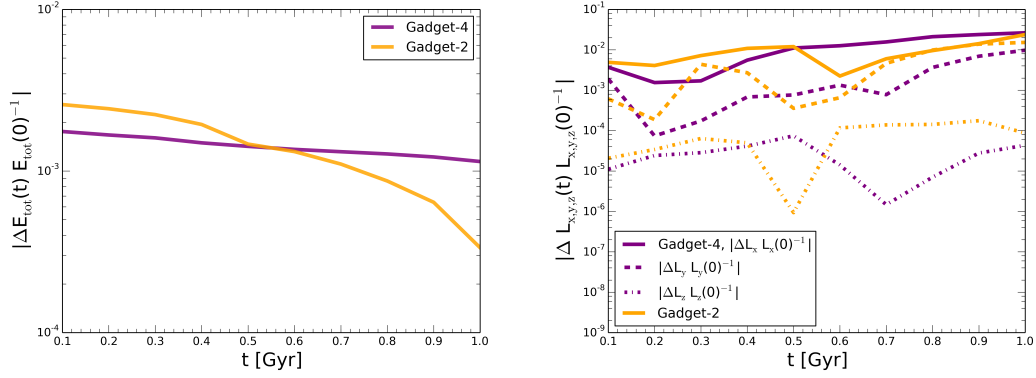
Figure 2.13: *Left panel:* Absolute value of the relative variation of E_{tot} in GADGET-4 (purple line) and GADGET-2 (orange line) for the simulation RELAX. *Right panel*: Absolute value of the relative variation of the three coordinate components of $\vec{L}_{tot}$ in the two codes. Colour codes as in the left panel. Line codes for the three coordinate directions as in the right panel of Figure 2.9.
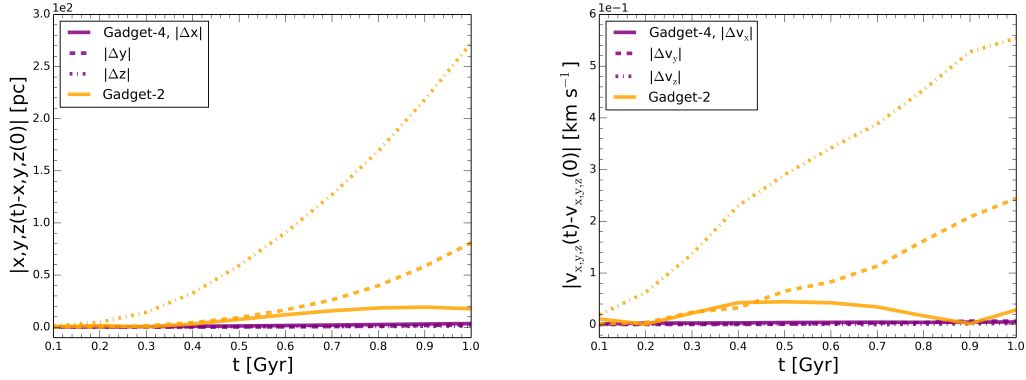
Figure 2.14: Absolute value of the variation of the centre of mass coordinates (left panel) and of the centre of mass velocity components (right panel) for the simulation RELAX in GADGET-4 and GADGET-2. Colour codes as in Figure 2.13. Line codes for the three coordinate directions as in the right panel of Figure 2.9.

2.9 Benchmark: summary and remarks

In this chapter, I showed a direct comparison of the results - obtained with the codes SUPERBOX-10 (by **MJ16**), CHANGA, and GADGET-2 - on the isolated evolution of the MW disc and on its thickening and heating when interacting with the MW satellites.

In the isolated case, the response in time of the disc to the presence of density perturbations is similar in the three codes, as evidenced by the similar oscillations of the surface density profile of the disc. For the isolated evolution, this general similarity of results has implications on the Galactic model employed here. The MW model used for these tests evolves overall due to its initial set-up, and not due to the peculiarities of the employed code, may this be a PM code like SUPERBOX-10 or a tree code like CHANGA and GADGET-2 (or even GADGET-4).

Also, another point emerging from the comparison of the isolated evolution of the MW is that the high values of the disc σ_R favour the increase of the profile of the Q parameter in the disc, preventing the formation of a bar. The generation of ICs for MW models like this one, using `GalIC`, produces non-equilibrium in the ratio σ_R/σ_ϕ, with transfer of kinetic energy from the tangential to the radial direction. Therefore, the fact that σ_R increases rapidly in the disc is not related to any specific issue of Superbox-10, since it was confirmed using the other three codes.

The test on the evolution of the MW in interaction shows similar results between the codes. It is confirmed, furthermore, what was found in **MJ16**: the satellite galaxies cannot impact too much on disc thickening and heating.

The usage of the new hierarchical timestepping in Gadget-4 produces more accurate results than in Gadget-2 and puts Gadget-4 in line with ChaNGa in terms of momentum conservation, at the same time with sufficiently good total energy and angular momentum conservation. Also, the smallest computational times required by Gadget-4 make it the fastest code among all the four codes tested in this benchmark.

Thus, Gadget-4 is an eligible code for the set of simulations that I am going to describe in Chapter 3, where I address the distribution of the satellite debris in the MW environment. The degree of accuracy and computational efficiency at an optimal speed granted by Gadget-4 make it convenient for obtaining reliable results on the distribution of the satellite debris with N-body simulations of the MW environment, at a good force resolution and in a short computational time.

Chapter 3

The distribution of the tidal debris of the Milky Way satellites in numerical simulations

In this chapter, I present an adapted version of the publication **MM20**, with the exclusion of its introduction, that was adapted in Section 1.4.1 of this thesis. The part of the publication adapted here corresponds to the numerical investigation on the satellite tidal debris in the MW environment. In Section 3.5 I then report an additional investigation of the effects of adding the MW stellar gravitational potential in the analytical calculation of the tidal radii of the satellites.

3.1 Section 2. from Mazzarini et al. (2020): Numerical simulations

We ran a set of N-body simulations of the MW interacting with its satellites to address the properties of the stripped satellite debris. As I already mentioned in Section 1.4.1 of this thesis, for each simulation we took the MW model used by **MJ16** for the corresponding Aquarius set-up, from Aq-A2 to Aq-F2. As I already discussed in Section 2.7.1 for the specific case of Aq-D2, the initial MW data for all the six cases were originally extracted by **MJ16** from the corresponding Aquarius cosmological volumes by recognising the corresponding NFW haloes at redshift $z = 0$. Then, **MJ16** used the information about these haloes to construct full disc-bulge-halo N-body models where the DM haloes have the best-matching Hernquist profiles corresponding to the original NFW halo profiles, as prescribed in Springel et al. (2005a). Like for the specific case of Aq-D2, the disc of these numerical MW models has an exponential profile with the distance of the Sun set to $R_0 = 8$ kpc from the GC, while the bulge has a Hernquist density profile. I already showed the parameters common to the MW models in Table 2.1.

For each MW halo that had been selected in the corresponding Aquarius simulation, **MJ16** employed a subhalo mass cut of 10^8 M$_\odot$ and required the subhaloes to have a pericentre passage within 25 kpc of the MW within 2 Gyr. They

71

resimulated these systems as higher resolution DM-only N-body spheroids (50 K particles each), for a total number of satellites per simulation ranging from a minimum of 12 (Aq-E2) to a maximum of 24 (Aq-F2). Their satellites have a range in mass that spans from 10^8 M$_\odot$ [1] to 6×10^{10} M$_\odot$. They modelled each satellite as an NFW profile, and each satellite has particles of equal mass. They placed the satellites in the positions indicated from the corresponding Aquarius simulations. In Table 3.1 we show the number of satellites, the NFW scale radii and the corresponding best-matching Hernquist scale radii of the MW models for the six Aquarius set-ups.

Table 3.1: Number of satellites and MW halo scale radii for the six Aquarius set-ups (from the second line from the top to the bottom line, Aq-A2 to Aq-F2) employed by **MJ16**. The columns indicate (from left to right) Aquarius run, number of satellites N_{sat} in the simulations, halo NFW scale radius $r_{\mathrm{scale,NFW}}$ and halo best-matching Hernquist scale radius a.

Aquarius run	N_{sat}	$r_{\mathrm{scale,NFW}}$ (kpc)	a (kpc)
Aq-A2	20	15.00	29.25
Aq-B2	17	24.98	42.76
Aq-C2	14	15.96	30.68
Aq-D2	23	25.91	43.90
Aq-E2	12	29.39	44.28
Aq-F2	24	24.80	42.54

3.1.1 Selecting the satellite galaxies

For the selection of the satellite galaxies to be used in our simulations in place of the DM-only ones from **MJ16**, we extracted the best dwarf galaxies from the sample of **M17**. The two samples of satellites come from different simulations (DM-only versus full N-body-SPH) run up to different final redshifts ($z_{\mathrm{final}} = 0$ versus $z_{\mathrm{final}} = 1$). Therefore, we chose to match them by minimising the distances of the two satellite samples in the $\log(M_{200})$-$\log\left[(v_{\mathrm{max}}/r_{\mathrm{max}})^2\right]$ space. Here, $v_{\mathrm{max}}/r_{\mathrm{max}}$ is the ratio of the maximum circular velocity of the satellite to the radius of maximum circular velocity. This ratio is an indicator of the inner density (and therefore of the depth of the potential well) of each satellite. In fact,

$$\left(\frac{v_{\mathrm{max}}}{r_{\mathrm{max}}}\right)^2 = \frac{G \times M(< r_{\mathrm{max}})}{r_{\mathrm{max}}} \times \frac{1}{r_{\mathrm{max}}^2} = \frac{4\pi G}{3}\bar{\rho}(< r_{\mathrm{max}}), \qquad (3.1)$$

where $\bar{\rho}(< r_{\mathrm{max}})$ is the average density within the radius of maximum circular velocity.

---

[1]This mass cut in **MJ16** was done to address the impact of satellite galaxies on the MW disc kinematics and dynamics, and in this case they showed that the impact of satellites increases with satellite mass as $\propto M^2$.
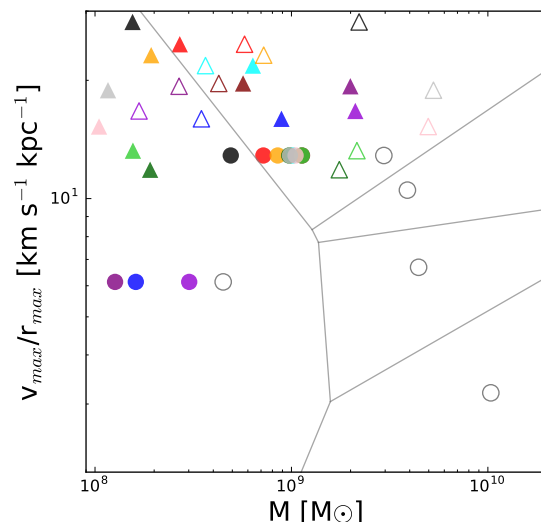
Figure 3.1: Distribution of the candidate best-matching dwarf galaxies in the $\log(M_{200}) - \log\left(v_{\max}/r_{\max}\right)$ plane. Empty grey circles represent all the five best-matching dwarf galaxies in the **M17** sample, which are used for the six Aquarius simulations (see Table 3.2 for their properties). The tessellation with grey segments represents the division in regions where the satellite galaxies of **MJ16** are closest to any of the five best-matching dwarf galaxies of **M17**. The satellites of **MJ16** are shown here for the case of Aq-E2 as empty triangles, according to their M_{200} and $v_{\max}/r_{\max}$ values. Filled triangles are the same satellites after tidal cutting, i.e. with their M_{tid} values. The filled circles show the corresponding **M17** satellites after tidal cutting. The colours of the filled symbols represent the matched pairs. For Aq-E2, only sat1 and sat4 have triangles that fall in their regions.

Due to the intrinsic differences in properties of the two samples of objects, we do not expect the matching sample to be as homogeneously distributed in the log-log space as the **MJ16** satellites. Consequently, five of the **M17** satellites fall in the relevant parameter range and so each candidate dwarf matches many satellites of **MJ16**. We also note that the selected objects tend to be lower in central density than the ones from **MJ16**. In Table 3.2 we show the number of particles, the masses of the gas, DM, and stellar component for each of the five selected dwarfs, together with their ratio of maximum circular velocity to radius of maximum circular velocity and their radius of maximum circular velocity.

In the next step we cut the total masses of the selected dwarfs to their initial tidal radii. In order to do this mass cut, we first calculated the tidal radius of each satellite of **MJ16**, as in Ernst & Just (2013):

$$r_{\mathrm{tid}}(r) = \left(\frac{M_{\mathrm{tid}}}{\omega^2 - \frac{d^2\Phi(r)}{dr^2}} \right)^{\frac{1}{3}}. \tag{3.2}$$

Here M_{tid} is the tidal mass of the satellite, r is its GCd, ω is its orbital angular speed, and Φ is the gravitational potential of the MW. In order to obtain the

Table 3.2: Properties of the five selected satellites before they are cut in tidal radii. The satellites are ordered from sat1 to sat5 (second column from left to right column) according to decreasing total DM mass. The lines indicate (from top to bottom) satellite name, number of gas particles, number of DM particles, number of star particles, total gas mass, total DM mass, total stellar mass, v_{max}/r_{max}, and r_{max}.

Satellite	sat1	sat2	sat3	sat4	sat5
N_{gas}	3.5×10^5	1.20×10^5	5.99×10^4	6.54×10^4	1764
N_{DM}	3.7×10^6	1.05×10^6	9.32×10^5	1.06×10^6	1.62×10^5
N_*	8.2×10^4	7880	8116	5194	406
M_{gas} ($M_\odot$)	1.92×10^8	9.80×10^7	4.92×10^7	3.61×10^7	9.72×10^5
M_{DM} ($M_\odot$)	1.02×10^{10}	4.34×10^9	3.85×10^9	2.92×10^9	4.49×10^8
M_* ($M_\odot$)	8.97×10^6	1.27×10^6	1.30×10^6	5.46×10^5	4.25×10^4
v_{max}/r_{max} ($km\,s^{-1}kpc^{-1}$)	3.34	6.37	10.37	12.27	6.26
r_{max} (kpc)	12.35	4.65	3.11	2.53	2.40

tidal radius for each **M17** satellite, we used the approximation

$$r_{tid,M17} = r_{tid,MJ16} \left(\frac{M_{200,M17}}{M_{200,MJ16}} \right)^{\frac{1}{3}}. \tag{3.3}$$

The resulting distribution of satellites masses is shown as full coloured symbols for the case of Aq-E2 in Figure 3.1. Since v_{max} and r_{max} are not altered by the tidal cutting, the satellites are shifted horizontally in the figure. For Aq-E2 only the two satellites sat1 and sat4 of **M17** were relevant.

3.1.2 Numerical dwarf galaxies as candidate satellites: properties

We show now that, thanks to our hybrid approach, with the selected hybrid dwarf galaxies we achieve a mass resolution which is an order of magnitude better than what is possible in current self-consistent cosmological simulations; that the density profiles of their stellar and DM components have different slopes, thereby allowing us to treat them as two distinct populations; and that the mass distribution of their DM and stars as a function of specific energy returns two distinct populations that we cannot naturally derive from the DM-only satellites. To do this, we show the properties of satellite 3 (particle mass distribution, density profile, and mass distribution as a function of specific energy) to represent all five satellites, since they all have similarities in these aspects.

Mass resolution

In the top panel of Figure 3.2 we can see that DM and stellar particle masses are orders of magnitude below the masses of the corresponding particles in the cosmological simulations TNG50, Eris, and Latte. The disc of our MW models,
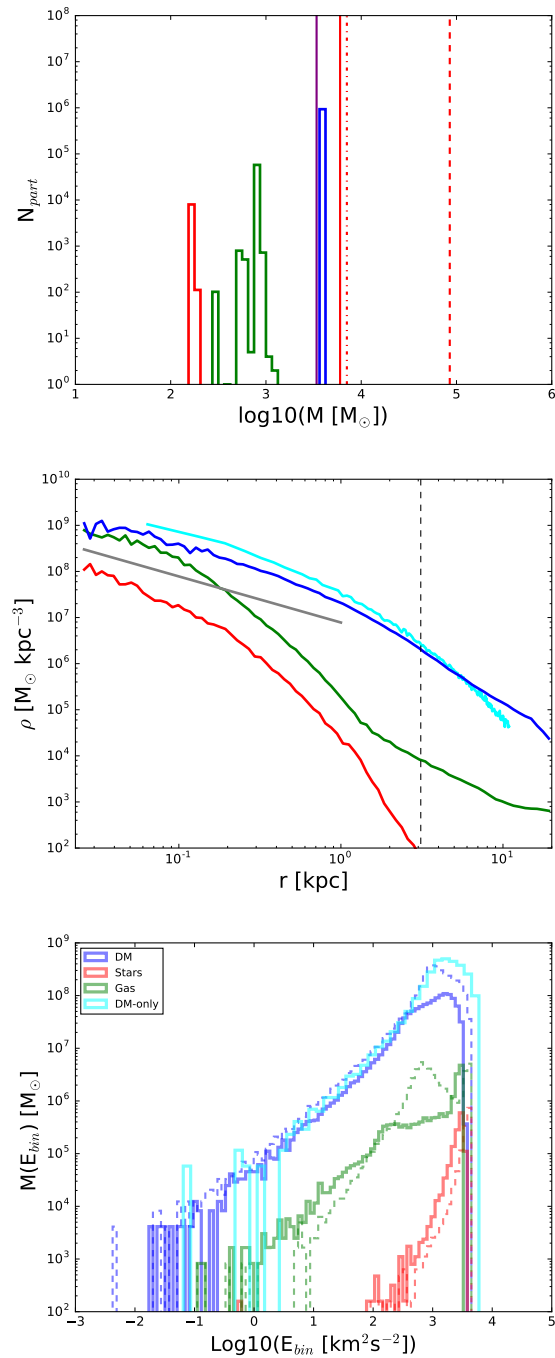
Figure 3.2: From top to bottom: Particle mass distributions, radial density profiles, and specific energy distributions for the three components (stars, gas, and DM) of satellite 3. In all figures, red is for stars, green for gas, and blue for DM. Cyan is for one corresponding DM-only satellite from **MJ16**. *Top panel*: The additional vertical dashed red line is the stellar mass resolution for the TNG50 simulation, the red dot-dashed vertical line is for Latte, and the red full line is for Eris. The purple full line is for the disc resolution in the MW model of **MJ16**. *Central panel*: The density profiles are given as a function of the distance r from the density centre of the satellite. For comparison, the full grey line represents an NFW inner profile (with radial dependence $\propto r^{-1}$). The black dashed vertical line indicates the tidal radius position of satellite 3 after tidal radius rescaling from the corresponding DM-only satellite. *Bottom panel*: The dashed and full histograms represent the specific energy distribution in terms of mass per energy bin for each component of satellite 3 before and after applying the tidal cut to the satellite, respectively. The cyan line shows the same for the DM-only satellite.

which is made of collisionless stellar particles, has a better resolution than the stars in the Eris simulation. This puts our satellite models and the disc models in a better position in terms of resolution. The fact that the stellar and DM debris particle masses are at least 2 orders of magnitude below the corresponding best cosmological simulation resolutions allows a more accurate statistical investigation of the stellar and DM debris in our simulations, avoiding low number noise in the calculations.

Density profiles

The central panel of Figure 3.2 shows the density profiles of gas, DM, and stars in satellite 3, as well as the density profile of a DM-only satellite that is substituted by satellite 3 in Aq-B2. The grey straight line shows the inner slope $\propto r^{-1}$ of a NFW profile, for comparison. We can see that while DM and gas have a slope of their inner density profiles close to the NFW case, the stellar component has a significantly steeper inner density profile. This is already a hint that there is no simple recipe to select a realistic stellar component based on a DM-only simulation.

Specific energy distribution

For each satellite particle we calculated its total specific binding energy (i.e. binding energy per unit mass) as

$$E_{\mathrm{bin}} = -\epsilon_{\mathrm{tot}} \,, \tag{3.4}$$

with

$$\epsilon_{\mathrm{tot}} = \epsilon_{\mathrm{pot}} + \epsilon_{\mathrm{kin}} \,, \tag{3.5}$$

where ϵ_{tot}, ϵ_{pot}, and ϵ_{kin} are the specific total, potential, and kinetic energy of the particles. For the gas particles, an additional term, the specific thermal energy ($\epsilon_{\mathrm{therm}}$) was counted in the sum. The specific thermal energy was calculated as

$$\epsilon_{\mathrm{therm}} = \frac{3}{2} \frac{n}{\rho} k_{\mathrm{B}} T \,, \tag{3.6}$$

where k_{B} is the Boltzmann constant and

$$\frac{n}{\rho} = \frac{1}{0.6 m_{\mathrm{H}}} \tag{3.7}$$

is the number of particles per unit mass for fully ionised gas, with the term m_{H} at the denominator being the hydrogen mass, $m_{\mathrm{H}} = 1.67 \times 10^{-27}$ kg.

Since the particle masses of the **M17** satellites vary over a wide range, we weighted the particle distributions in specific energy by their masses. In the bottom panel of Figure 3.2 we plot the specific energy distributions of each component for the satellite 3 at $z = 1$ before and after tidal cutting. For comparison the specific energy distribution function (also weighted by particle mass) of a corresponding DM-only satellite of **MJ16** is shown in cyan. Even after

tidal cutting, the gas and DM particles of **M17** dwarfs and the DM particles of **MJ16** satellites have specific energy distribution functions with a similar slope. In contrast, the shape of the distribution function of the stellar component is very different to the distribution of the DM component of the **M17** and the **MJ16** satellites. This confirms the need for baryonic physics in the satellite models in order to obtain a realistic stellar component.

3.1.3 Numerical set-up and simulation properties

We ran a total of 12 simulations, two for each corresponding Aquarius set-up from **MJ16**. For the first set of six simulations, one for each Aquarius set-up from **MJ16**, we put the five best-matching satellites in place of the corresponding **MJ16** satellites at the same initial positions and velocities. For the second set of six simulations, again one for each Aquarius set-up from **MJ16**, we used the same five best-matching satellites in place of the corresponding **MJ16** satellites, this time rotating the MW disc by 90° to obtain a control set of simulations to check the final distribution of the satellite debris.

Each satellite contains hundreds of thousands of DM particles and hundreds to thousands of star particles. This, considering the number of satellites per simulation, allows a good statistical investigation of the properties of the DM and stellar debris.

We made use of the N-body code GADGET-4 (with `MPI` prescriptions to run it in parallel), since, as I showed in Section 2.8, it compares well with other recent codes, and at a reasonable degree of accuracy and momentum conservation. In addition to what I described in Section 2.8, GADGET-4 has SPH (Springel & Hernquist 2002; Hopkins 2013) and SF (Springel & Hernquist 2003) recipes that can optionally be switched on.

Typically, gas is stripped from satellites as they enter the MW environment (Grebel et al. 2003; Frings et al. 2017; Simpson et al. 2018). Additionally, considering the median case, the surviving gas in satellites forms the greatest fraction of their present-day stellar component before $z = 1$ (Weisz et al. 2014). Therefore, as a first approximation, we can switch off the hydrodynamics and the SF recipes and focus only on running N-body simulations.

The **M17** satellites are made of DM, stars, and gas. Here we are only interested in the tidal debris of the DM and the stellar component. Since the gas component contributes to the depth of the satellite potential wells, we kept it in the simulations as N-body particles. On the other hand, the gas particles represent only a tiny fraction at each specific energy compared to the DM component (see Figure 3.2), which also results in a negligible contribution to the total debris. Therefore, for simplicity we added the gas particles to the DM component in the following analysis.

In all our simulations we employed a softening $\epsilon = 200$ pc for the MW halo (in order to minimise spurious scatter effects on the DM halo particles) and $\epsilon = 50$ pc for the disc and bulge (for a higher resolution in the force calculation). The satellite DM and star particles have softening values $\epsilon = 25$ pc and $\epsilon = 10$ pc, respectively. Given that for the employed gravitational softening kernel

(Monaghan & Lattanzio 1985) the Newtonian force radial dependence $\propto r^{-2}$ is exactly reproduced at distances $r > 2.8\epsilon$ (Springel 2005), the smaller softening choice adopted for the satellite particles allows a very high resolution of the forces, and hence a more accurate description of the tidal forces acting on the satellites. The MW disc, bulge, and halo particles have masses of $3.4 \times 10^3\,\mathrm{M}_\odot$, $3.8 \times 10^4\,\mathrm{M}_\odot$ and $4.4 \times 10^5\,\mathrm{M}_\odot$, respectively. **MJ16** also chose to use 10M particles in the disc of their MW models in order to have a high-resolution disc. This is useful because the higher resolution of the disc means less spurious scattering of the satellite debris particles that approach the inner MW halo, dominated by the disc.

Each simulation was run on 96 parallel CPUs on the computer cluster `bw-ForCluster`. We ran each of the six simulations for a total of 2 Gyr. For our analysis, we focused mainly on the final snapshot of each simulation. However, we generated outputs every 50 Myr in order to track the process of mass stripping from the satellites.

In all the simulations, before analysing any snapshot, we have rescaled all the particle coordinates and velocities in the snapshot by the position and velocity of the MW density centre. Then, we have rotated the coordinate frame around the MW density centre in order to have the MW disc angular momentum aligned with the new z-axis. This procedure is the same as the one employed in Chapter 2 before analysing the simulations in the benchmark.

3.1.4 Impact of the satellites on the MW disc thickening and heating

As a cross-check of the quality of our selection of satellites, we first compare the impact of our satellites on the MW disc with the corresponding results from **MJ16** data, in particular calculating the disc thickening and heating. We compare these results to check whether a different distribution of satellites (the distribution of hybrid satellites) has a different impact on the thickening and heating of the disc, and hence whether it produces a different dynamical effect on the disc.

For each simulation we calculated the disc vertical thickness z_rms and the squared vertical velocity dispersion σ_z^2 for each ring-like bin of radius R in the disc. The vertical thickening and heating were calculated as $\Delta z_\mathrm{rms} = z_\mathrm{rms,2} - z_\mathrm{rms,0}$ and $\Delta \sigma_z^2 = \sigma_{z,2}^2 - \sigma_{z,0}^2$, where the subscripts 2 and 0 indicate that the given quantity is calculated at time $t = 2\,\mathrm{Gyr}$ and $t = 0\,\mathrm{Gyr}$, respectively.

In Figure 3.3 we show the average radial profile of the disc vertical thickening and heating for the two simulation sets, together with their root mean square (rms) scatters (represented by the shaded areas). We note that, even if the disc thickening and heating are higher on average for **MJ16** data, within the rms scatter of the six simulations our results are consistent with those from **MJ16**.

The implications are that the MW disc is similarly excited if a population of DM-only satellites or hybrid satellites is used. Since the selection of satellites from **MJ16** was made based on their dynamical effect on the MW disc (i.e.
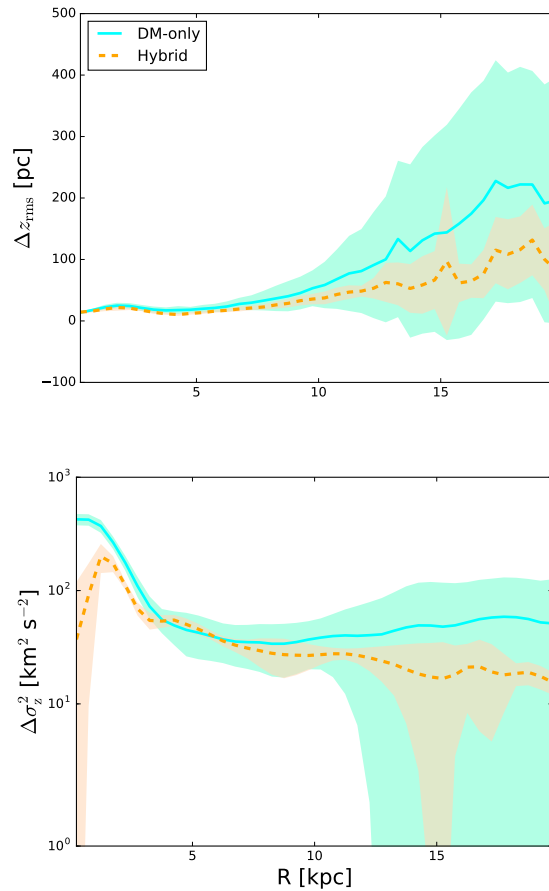
Figure 3.3: Top and bottom panels: Radial profiles of disc thickening and disc heating, respectively. The cyan full line represents the data from **MJ16** simulations; the orange dashed line represents the data from our simulations.

based on a mass cut), having a population of satellites with similar mass range (see Figure 3.1) implies that the effects on the disc are similar and weakly dependent on the presence of only DM or of additional stars as well. The thicker scatter in **MJ16** data is due to the F2 case, where a massive satellite of more than 10^{10} M$_\odot$ is strongly interacting with the MW disc.

3.2 Section 3. from Mazzarini et al.(2020): Results

3.2.1 Stripping of matter

We now show how much stellar and DM debris are stripped by the MW and their distribution in the Galactic environment. For each satellite we calculated its density centre at every snapshot in order to define its position in time. We then used the tidal radius calculation of Equation (3.2), approximating the orbit of the particle to a circular orbit, i.e. interpreting the magnitude of the velocity vector as the magnitude of the velocity pointing in the tangential direction of the orbit. The total, initial satellite mass was used at the numerator

of Equation (3.2). At each snapshot we checked what fraction of total satellite stars and DM was found outside of the tidal radii of the satellites. We show the result in Figure 3.4. The fraction of tidally stripped stellar debris increases to a maximum of 30% of the total initial stellar satellite mass. Instead, the satellite DM is stripped up to 80% of the total initial mass. We also plot the results of our analysis on the data from **MJ16**. DM-only satellites also lose most of their DM, up to 70% of the initial DM mass.

In order to interpret these results, we focus on the properties and orbital distribution of the satellites in our simulations. These satellites were modelled as N-body objects made of star particles, mostly found in their core region, and DM particles, which distribute into shallower and more extended density profiles. Thus, DM can be stripped more easily and larger fractions of its mass, originally residing in the satellites, can end up as debris in the MW environment. Instead, stars are mostly confined in the inner regions of the satellites and significant stripping of this matter only occurs when the satellites closely approach the MW.
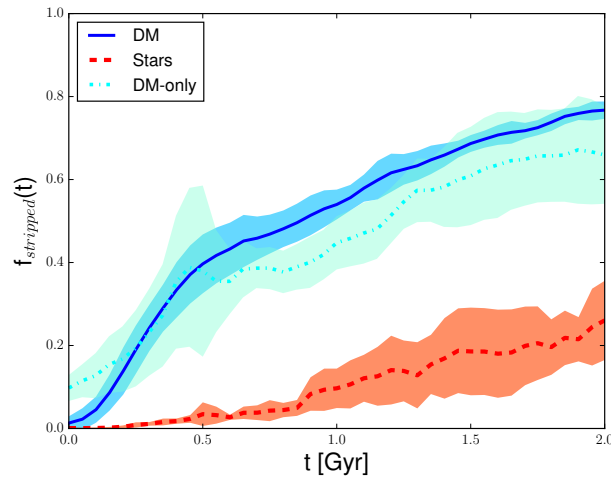
Figure 3.4: Fraction of the satellite matter stripped out of the tidal radii of all the satellites as a function of time. Colour-coding and lines: dashed red for stars, full blue for DM, and dot-dashed cyan for DM-only satellites from the **MJ16** simulations. For each colour, the lines are the average over the six simulations, and the shaded areas represent the rms scatter.

3.2.2 Radial distribution of the debris

We wanted to know whether there is any difference in the final distribution of the stellar and DM debris in the MW environment. We addressed this by calculating the probability distribution function P_{stripped} of the debris (normalised by the total debris mass within the virial radius of the MW, $r_{200} = 242.8$ kpc; all the debris out of this radius is considered lost) that ends at a given GCd from the MW centre, as a function of the GCd. The radial bins have a width of ~ 6 kpc. P_{stripped} is a measure of how much mass out of the total debris ends in a given spherical shell. In the top panel of Figure 3.5 we plot the results of this

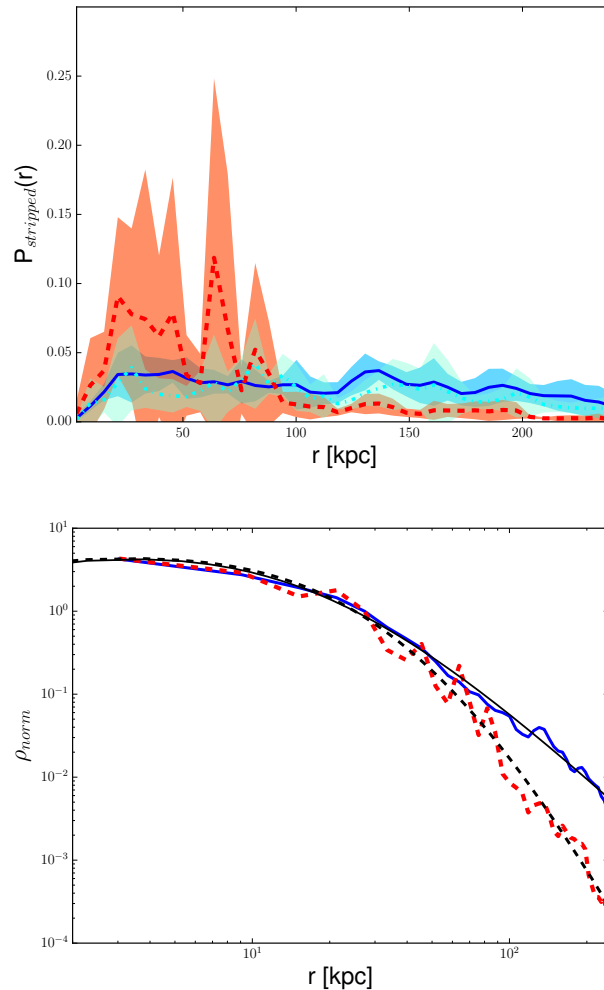calculation. The distribution of the DM debris is quite smooth and uniform

Figure 3.5: *Top panel*: Radial profile of P_{stripped} for the stripped debris mass deposited at a given spherical shell, normalised by the total debris mass of stars and DM, respectively. Colour and line codes as in Figure 3.4. *Bottom panel*: Radial matter density profile of the debris in log-scale. Colour and line codes as in Figure 3.4. The DM-only satellite data from **MJ16** are not plotted here. The full black and dashed black line are the best-fit profiles for the DM and stellar debris, respectively. All profiles are normalised by the corresponding density values at $r \sim 25$ kpc.

throughout all radii up to the MW virial radius with some deficit in the inner-most region. In the stellar distribution there are some prominent peaks in the inner 100 kpc which correspond to more confined stellar streams of satellites close to pericentre passage. In the outer MW halo, significantly lower fractions of stellar debris are found. We note that the DM-only satellites debris and the hybrid satellites DM debris suffer similar tidal stripping and have similar values of P_{stripped}.

In the bottom panel of Figure 3.5 we show the radial density profiles of the DM and stellar debris in the MW halo, and their best-fitting functions, for the simulations with the hybrid satellites. The radial density profiles were cal-

Table 3.3: Best-fit parameters for the fitting curves of the density profiles of the DM and stellar debris in Figure 3.5.

Debris component	ρ_0 $(\mathrm{M_\odot\ kpc^{-3}})$	r_s (kpc)	α	β
DM	1.62×10^5	15.34	-0.66	2.94
Stars	7.15×10^1	47.51	-0.44	6.17

culated dividing the values of P_stripped by the spherical-shell volumes of the corresponding bins. To fit the data, we chose the generalised NFW profile as a function of GCd:

$$\rho(r) = \frac{\rho_0}{\left(\frac{r}{r_\mathrm{s}}\right)^\alpha \left(\frac{r}{r_\mathrm{s}} + 1\right)^{\beta-\alpha}} \ . \tag{3.8}$$

Here, ρ_0 is the scale density, r_s is the scale radius, α controls the inner slope, and β controls the outer slope. The best-fit parameters are given in Table 3.3. For both debris components we found that the inner slope is positive ($\alpha < 0$) describing the mass deficit inside ~ 5 kpc for DM and for stars. The profile scale radius is higher for stars, reaching ~ 45 kpc against the ~ 15 kpc of the DM debris profile. The outer slope of the DM debris is very close to that of a standard NFW profile. In contrast, the stellar debris shows a much steeper drop at large radii.

This picture points to the fact that at large radii fewer stars are stripped, and the stars stripped in the inner halo are on more circular orbits. This also explains the inner peaks of stellar mass fractions in Figure 3.5. DM debris can be released at any distance and the contribution to its radial distribution comes from both inner and outer satellites, thus the probability distribution function of the DM debris is radially more uniform and its density profile is less steep. Calculating the cumulative fraction of the stellar debris as a function of GCd, we find that $\sim 30\%$ of the total stellar debris is inside 30 kpc and $\sim 50\%$ is within 60 kpc of GCd. For comparison, the MW NFW halo scale radii in these MW models range between 15 kpc and 30 kpc (see Table 3.1).

3.2.3 Shape of the debris

We now consider the geometrical distribution of the tidal debris in the inner MW region. We focused on the inner 25 kpc of GCd in order to see what the impact of the local MW environment is on the debris. We wanted to understand the following points: *a)* Does the debris finally show a spherical or flat geometry? *b)* What is the orientation of the debris distribution? *c)* Is there any difference between the DM and stellar debris?

In order to answer these questions, we introduced the Second Order Momenta Tensor (hereafter SOMT) in our analysis. The SOMT is a rank-2 tensor

for which the jk entry is calculated as

$$I_{jk} = \sum_{i=1}^{N} m_i x_{i,j} x_{i,k} \, , \tag{3.9}$$

where i indicates the i-th particle (out of N particles), m_i is its mass, and $x_{i,j}$ and $x_{i,k}$ are its Cartesian coordinates (**BT08**, Polyachenko et al. 2016). In our case N is the total number of particles that fall in a given sphere centred on the MW GC. The definition employed here for the SOMT addresses the global geometrical distribution of the debris, no matter how sub-structured it is. An indicator of the flattening of the matter distribution is represented by the ratio c/a between the SOMT semi-minor and semi-major axes c and a, whereby c and a are the square roots of the eigenvalue with the smaller and larger magnitude, respectively.

We focused on the inner 25 kpc in the MW halo since we were interested in the behaviour of the debris in the local halo environment. Specifically, for each simulation we calculated the tensor for the debris falling in each sphere centred on the GC. We chose a radial binning of 5 kpc to minimise the noise due to low number statistics and to smooth the contribution of single streams. For each simulation we calculated c/a at each sphere, and then for each sphere we averaged the ratio over the six simulations. In Figure 3.6 we show the radial profile of c/a for the stellar and DM debris together with the rms scatter. From
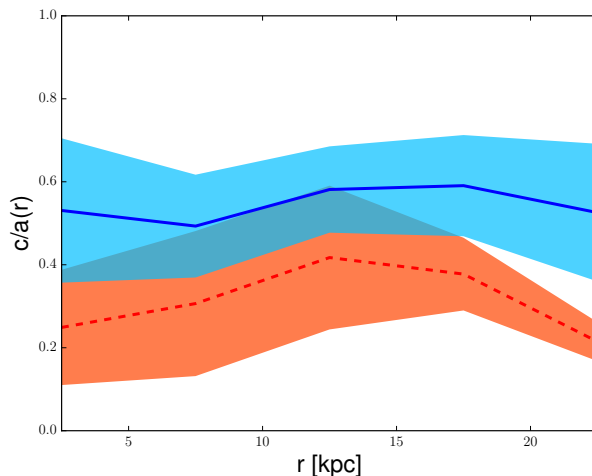
Figure 3.6: Radial profile of the c/a ratio for the SOMT of the stellar (red) and DM (blue) debris at $t = 2$ Gyr. Colour and line codes as in Figure 3.4. For each profile, the central line is the average profile over the six simulations, and the shaded area represents the rms scatter.

Figure 3.6 it is evident that the stellar and DM debris are both geometrically flat, but with a significant scatter. For the DM debris we found $c/a \sim 0.55$, whereas the stellar debris is flatter by a factor of two. The flattening depends only weakly on the size of the sphere.

We now discuss the spatial orientation of the flattening, which is defined by the direction of the shortest eigenvector e_c of the SOMT corresponding to the

eigenvalue c^2. We calculated this orientation in the $\theta - \phi$ (latitude-azimuth) angles-space for the DM and stellar debris at each radius and for each simulation separately. In Figure 3.7 we plot the distribution of the directions of e_c in the angles-space at different GCds, using a Mollweide projection. If e_c was defined at any point with negative z corresponding to $\theta < 0$, we changed its sign in order to have it with positive values of z. This was done to avoid ambiguities in the interpretation of the direction of the minor axis in the angles-space since every eigenvector allows taking both orientations along its direction, with a difficult interpretation in the Mollweide projection[2].
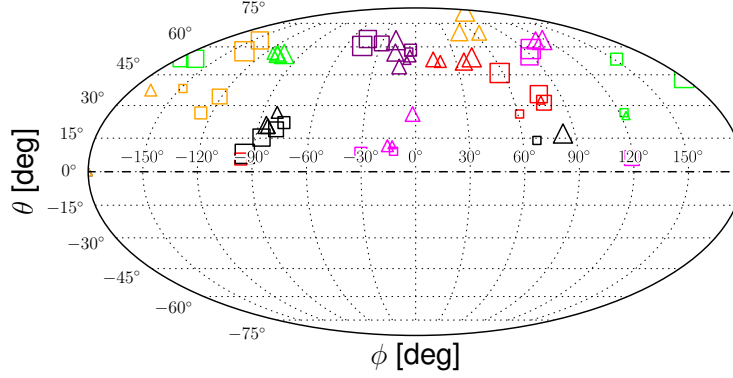
Figure 3.7: Mollweide projection of the distribution of the orientation of the semi-minor axis c. The azimuth ϕ changes horizontally, while the latitude θ changes vertically. Squares represent DM, triangles represent stars. Smaller markers are for inner radii, larger markers are for outer radii. Colours are black, lime, purple, red, magenta and orange for the Aq-A2 to Aq-F2 set-up, in order. The horizontal dot-dashed line indicates the Galactic plane.

The orientations of the short axis in the different simulations (different colours) are distributed over a wide region in the angles-space. This suggests that there is not a huge impact of the disc on the final distribution of the debris. Additionally, there is a large variation in the orientation with increasing GCd (size of symbols) as a sign of strong substructures in the debris. Furthermore, squares (DM) and triangles (stars) of the same simulation (same colour) do not occupy the same region in the angles-space. We interpret this as an indication that the DM and stellar debris show significantly different distributions and structures.

We wanted to quantify how big the differences in ϕ and θ are between the short axis of the stellar and DM debris tensor. To do this, we calculated the

---

[2]In fact, the opposite of a vector in this kind of projection is not simply represented as the symmetric opposite in the map with respect to $(\phi, \theta) = (0, 0)$.

great-circle distance (GCircD) $\Delta\alpha$ at each sphere between DM and stars as

$$\Delta\alpha(\mathrm{DM}, *) = \arccos\left[\sin\theta_{\mathrm{DM}}\sin\theta_* + \cos\theta_{\mathrm{DM}}\cos\theta_*\cos\Delta\phi\right], \qquad (3.10)$$

where $\phi_{\mathrm{DM}}, \theta_{\mathrm{DM}}$ are the angles of e_c for the DM debris SOMT as a function of the radius r of the sphere; ϕ_*, θ_* are the same angular quantities for the stellar debris; and $\Delta\phi = \phi_{\mathrm{DM}} - \phi_*$. We show these results in Figure 3.8. The average difference in angular distribution between DM and stars is no more than $10 - 20^\circ$ in the central part of the halo (the first few kpc), whereas it reaches up to 40° going out towards 15-20 kpc, where the scatter around the average is very high. This indicates that it is not possible to find a simple systematic correlation between the DM and stellar debris orientations in the environment around the MW. This is reinforced by the different c/a and the different radial distribution of the debris seen in Figure 3.5 and Figure 3.6. The DM and stellar debris do not share the same geometry once they are stripped from their satellite progenitors. Observationally, this means that it is not possible to track the distribution of the DM debris from the distribution of the stellar debris directly.
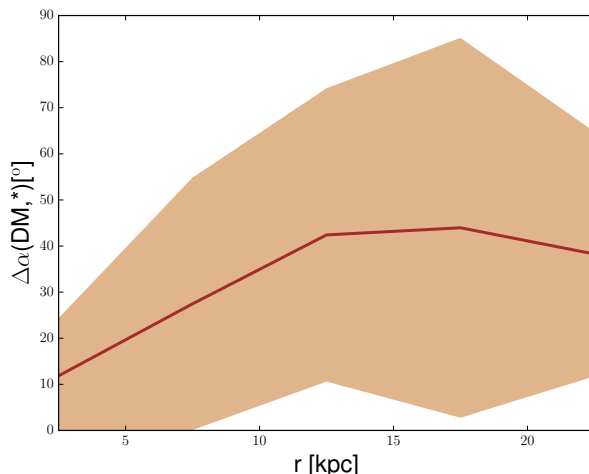
Figure 3.8: Average radial profile of the GCircD between DM and stellar debris as a function of spherical radius r. The shaded area represents the rms scatter.

It is important at this point to understand if the disc can have any impact at all on the final distribution of the debris, or if this depends on the initial distribution of the satellites only. To test this, we ran another set of six simulations, each corresponding to one of the six previous simulations. For each simulation set-up, we rotated the initial relative position and velocity of the disc particles by 90° around the y-axis resulting in a disc in the yz-plane rotating around the x-axis[3]. We ran these six new simulations for 2 Gyr.

At the end of the simulations, we analysed the final angular distribution of the debris, always within 25 kpc of GCd. If the disc were mainly responsible for

---

[3]This effective rotation transforms the x-axis to the $-z$-axis, the z-axis to the x-axis, and leaves the y-axis unchanged.

the flattening of the satellite debris, we would expect the minor axis distribution of the SOMT to be rotated approximately similarly to the disc by $\sim 90^\circ$. As can be seen in Figure 3.9, the final Mollweide projection of the debris is mostly overlapping the same region of the debris distribution in the original set of simulations, and shows no systematic rotation with respect to it. This confirms that the ICs of the satellites have a larger effect than the disc orientation on the final debris distribution.
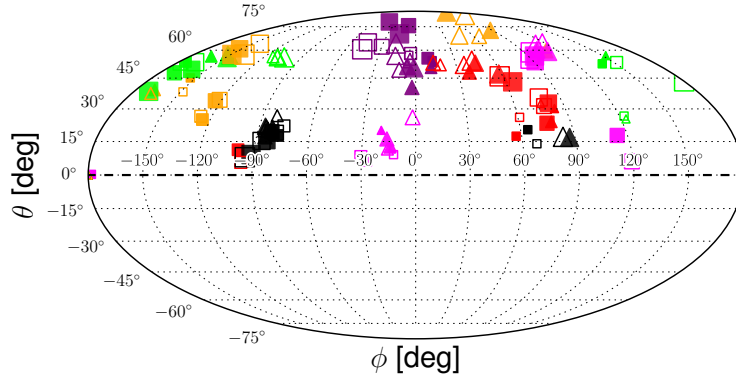
Figure 3.9: Mollweide projection of the distribution of the debris c axis in the angles-space, for the rotated and non-rotated disc simulations. Data from Figure 3.7 are re-plotted as empty markers. Solid markers are for the rotated disc simulations. Colour codes as in Figure 3.7.

We then quantified the GCircD at each sphere between the debris in the new set of simulations and the debris from the original set of simulations,

$$\Delta\alpha(\mathrm{rot}, 0) = \arccos\left[\sin\theta_{\mathrm{rot}}\sin\theta_0 + \cos\theta_{\mathrm{rot}}\cos\theta_0\cos\Delta\phi\right], \qquad (3.11)$$

where in this case $\phi_{\mathrm{rot}}, \theta_{\mathrm{rot}}$ are the angles of the c minor axis for the SOMT within the given spherical radius r for the debris from the second set of simulations with rotated disc orientation; ϕ_0, θ_0 are the same angular quantities for the original set of simulations; and $\Delta\phi = \phi_{\mathrm{rot}} - \phi_0$.

In Figure 3.10 we can see that on average $\Delta\alpha(\mathrm{rot}, 0) \sim 10^\circ$ for DM, while at the outer radii it reaches values of up to $\Delta\alpha(\mathrm{rot}, 0) \sim 20^\circ$ for stars. So, the rotation of the disc ICs produces a limited, yet not completely negligible rotation of the final distribution of the debris, which implies that the disc may have a moderate impact on the final distribution of the local satellite debris.
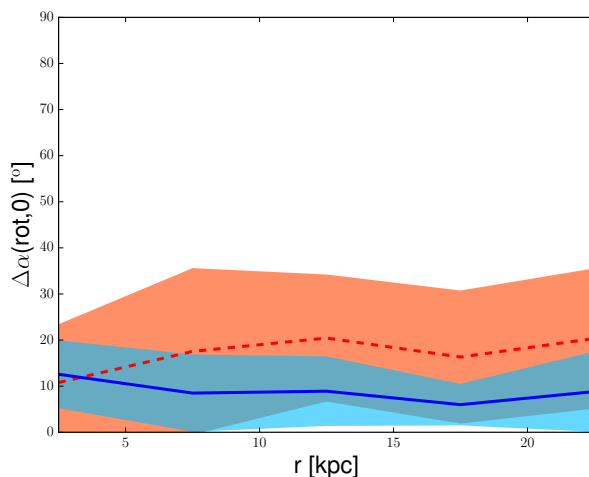
Figure 3.10: Radial profile of the GCircD $\Delta\alpha$ of the rotated disc simulations compared to the corresponding original simulations, for the short axis orientation of the stellar and DM debris. Colour and line codes as in Figure 3.4. The shaded areas are the rms scatter.

3.3 Section 4. from Mazzarini et al.(2020): Additional investigation: fraction of surviving satellites and dark-matter-to-stellar mass ratio

In addition to the final distribution of the debris in the MW halo, we checked the fraction of satellites that survived after $2\,\mathrm{Gyr}$. To determine whether a satellite survived stripping, we chose a threshold fraction of 10% of its total initial mass. A satellite that has a final tidal mass higher than 10% of its initial mass is considered to have survived. Otherwise, it is counted as dissolved. In Figure 3.11, top panel, we show the fractions of the surviving satellites for our six simulations and for the **MJ16** simulations. The error bar around each data point is the scatter between the six simulations of the same set.

In all simulations more than $\sim 65\%$ of all satellites survive after $2\,\mathrm{Gyr}$. The averages of the six simulations for both cases are reported as a full cyan line (DM-only) and a dashed orange line (hybrid). We also plot the area of the rms scatter between them with the same colour-coding. We found $f_{\mathrm{survived}} \sim 0.8 \pm 0.1$ for both sets of simulations, thus we confirm the similarity of results between them with no systematic differences.

We also looked at the ratio between DM and stellar mass inside the satellites at the beginning and at the end of the hybrid simulations, to understand the evolution of the matter content inside the satellites. This result is plotted in the bottom panel of Figure 3.11 in logarithmic values. The best-fit value $(M_{\mathrm{tot}}/M_*)_{\mathrm{best}} = 768^{+217}_{-301}$ at the final epoch is also shown. For all the satellites that survived, the ratio of DM to stellar matter, though still much higher than the cosmic ratio, decreased in time. This is a consequence of what was shown in Figure 3.4 where more DM than stars is stripped from the satellites.

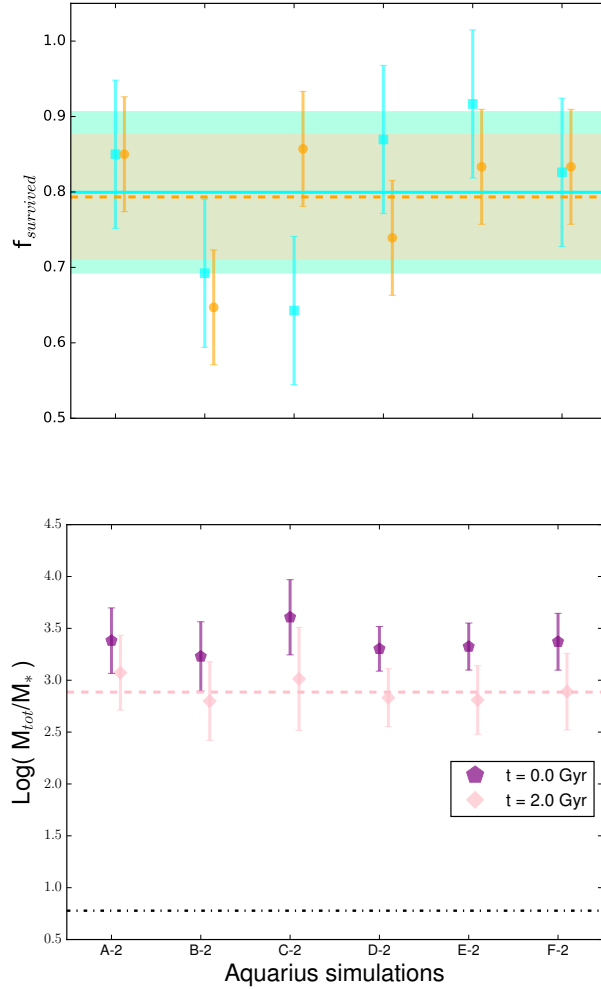For comparison, we give the cosmic ratio of all matter to baryons from the

Figure 3.11: *Top panel*: Fraction of surviving satellites, with 10% of their initial mass adopted as the threshold to determine their survival, in the Aq-A2 to Aq-F2 simulations. Colour codes as in Figure 3.3. The orange and cyan error bars are the rms scatter for our set of simulations and for the **MJ16** simulations, respectively. *Bottom panel*: Logarithm of the ratio of total mass to stellar mass in the satellites in the Aq-A2 to Aq-F2 simulations, $\log\left(M_{\mathrm{tot}}/M_*\right)$, for the initial and final snapshot. Purple pentagons are the average of each corresponding simulation for the initial data at $t = 0\,\mathrm{Gyr}$; pink diamonds are instead for the final data at $t = 2\,\mathrm{Gyr}$. The purple and pink error bars are the rms scatter for all the satellites in each corresponding simulation (initial and final snapshot, respectively). The dot-dashed black line is the density ratio $\Omega_{\mathrm{m}}/\Omega_{\mathrm{bar}}$ of all matter to baryonic matter. The pink dashed line represents the best fit for the final ratios $(M_{\mathrm{tot}}/M_*)_{\mathrm{best}}$. Only the satellites that survive the stripping process are employed to calculate the average and the standard deviation in each simulation.

WMAP-7 (Seven-year Wilkinson Microwave Anisotropy Probe) results (see Komatsu et al. 2011), $\Omega_{\mathrm{m}}/\Omega_{\mathrm{bar}} \sim 6.0$, being much lower than the initial ratio in our simulations. It appears that the DM-to-star ratio is subject to two phases. As argued in **M17**, in the first phase, before they strongly interact with the MW, the satellite galaxies lose large quantities of gas; therefore, their total-matter–to–baryons ratio increases (so they start in our simulations with a high total-matter–to–stars ratio). In a second phase (i.e. in more recent epochs), strong

tidal interactions with the MW deplete the satellite dwarf galaxies of more DM than stars and drive the total-matter–to–stars ratio towards lower values by a factor of $2 - 4$ on average.

Assuming a stellar mass-to-light ratio of two in solar units, the satellites in our simulations fall in the regime $1.2 \times 10^3 \, \mathrm{L_\odot} - 4 \times 10^6 \, \mathrm{L_\odot}$ corresponding to UFDs (Simon 2019)[4]. The mass-to-light ratios, which correspond to the tidal
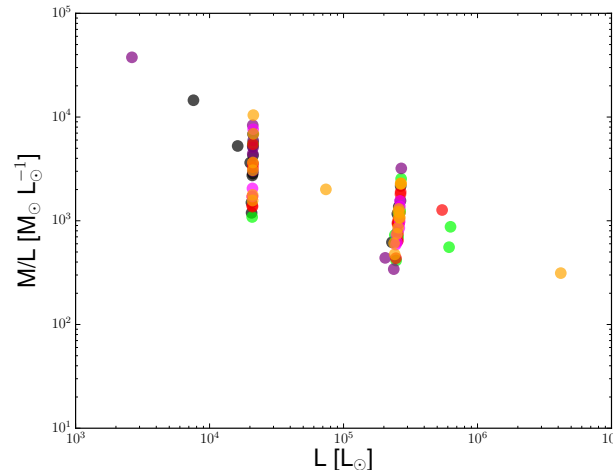

Figure 3.12: Distribution of the surviving satellites in the $L - M/L$ plane for the six simulations adopting a stellar mass-to-light ratio of two. Colour codes as in Figure 3.7.

mass-to-light ratios, of all our surviving satellites are shown as a function of luminosity in Figure 3.12. The tidal mass-to-light ratio was estimated for the first time by Faber & Lin (1983) for seven dwarf spheroidal galaxies, finding a much lower value than our mass-to-light ratio of $(M/L)_{\mathrm{best}} \sim (1.5 \times 10^3)^{+434}_{-606} \, \mathrm{M_\odot}$ $\mathrm{L_\odot^{-1}}$. Simon (2019) showed that M/L inside the half-light radius R_{h} decreases with increasing luminosity from ~ 1000 (with a large scatter) for $L = 10^3 \, \mathrm{L_\odot}$ to ~ 10 for $L = 10^7 \, \mathrm{L_\odot}$, which is similar to the values of Errani et al. (2018) inside $1.8 \, R_{\mathrm{h}}$. We found the same trend of mass-to-light ratios as a function of luminosity, but our values are systematically higher by a factor of a few. This offset is expected because the tidal radius is larger than $2 \, R_{\mathrm{h}}$ in most cases.

3.4 Extract from the paper Mazzarini et al.(2020): 5. Conclusions and discussion

3.4.1 Conclusions

We have performed a set of N-body simulations to investigate the general properties of the satellite debris distribution in the MW environment. For the first

---

[4]There is one satellite in our simulation from the Aq-F2 set-up that ends with L= $50 \, \mathrm{L_\odot}$, but it is below the range considered in Figure 4 of Simon (2019).

time, we took advantage of a set of satellite galaxy models taken from cosmological high-resolution hydrodynamical simulations, placed in initial orbits derived from the results of N-body cosmological simulations of structure formation, and of a full high-resolution N-body MW host model taken from the literature, consisting of live disc, bulge, and halo. For a statistical analysis, the ICs of six Aquarius simulations were used. Following the approach of **MJ16**, all satellites with tidal masses higher than 10^8 M$_\odot$ and with a pericentre passage closer than 25 kpc were taken into account. We ran each simulation for 2 Gyr.

We investigated the general properties of the debris of satellite galaxies in the global and local MW environment. We focused on the differences in the distribution of stellar and DM debris. Based on our findings, we can state the following:

- The stellar component in the satellite galaxies is much more tightly bound than the DM component and cannot be deduced from DM-only simulations;

- The stripping process acting on satellite DM is more efficient than on satellite stars and releases more DM debris than stellar debris in the MW environment (80% compared to 30%);

- The radial density profile of the DM debris covers the whole host halo and shows a standard NFW slope in the outer region; the stellar debris is confined to the inner 50 kpc with a steep cutoff outside; both profiles show a deficit in the inner 5 kpc;

- The stellar debris shows more prominent peaks of the radial probability distribution function than the DM debris, pointing to a more confined structure of individual streams in the inner part of the MW halo;

- The debris of DM and stars distribute with some degree of flatness ($c/a \sim 0.55$ and 0.3, respectively); the orientation of the minor axis is very different for the different simulations and shows no obvious correlation to the MW disc plane; the orientation of the DM and the stellar debris is not well correlated in each simulation, thus it is not possible to reconstruct DM debris and streams directly from observed stellar streams;

- Changing the orientation of the disc by $90º$ has a small effect on the distribution of the satellite debris; this confirms that the structure of the DM and stellar debris of satellite galaxies is mainly determined by the ICs of the satellites; the flattened potential of the disc only plays a minor role;

- The tidal total-to-stellar mass ratio of the satellites decreases by a factor of $2-4$ during the simulations and shows at the end mass-to-light ratios that are consistent with observations of the Local Group UFDs.

In conclusion, we can state that the stellar and DM components of the satellites are subject to different stripping efficiencies and different redistributions in the MW environment, thus they are not strongly correlated. As a consequence,

observed stellar streams cannot directly be converted to the distribution of the DM debris. Furthermore, we showed the importance of cosmological ICs as well as the realistic structure of satellite galaxies in determining the final distribution of the satellite streams around the MW.

3.4.2 Discussion

The fact that the debris (particularly the stellar debris) has some degree of flatness shows that with a cosmologically motivated initial set-up (e.g., in our case, from Aquarius simulations data) it is possible to obtain a flat spatial distribution of the debris. On the other hand, our debris does not show any distribution on a unique plane, as can be seen from Figure 3.7, where within different radii the debris tensor seems to occupy different regions in the angles-space in the same simulation and for each individual component (DM and stars). This contrasts with what was stated by Pawlowski et al. (2012), that was in favour of the formation of a plane of debris. Furthermore, since our results predict no systematic orientation of the stellar and DM debris, this means that other techniques may be needed to trace the distribution of DM streams other than addressing the distribution of the stellar streams alone.

Regarding the mass loss of the satellites in our simulations, Simon (2019) stated that tidal stripping affects the luminosity but not the metallicity of the stellar populations of satellites, and since the luminosity-metallicity relation is satisfied for the observed UFDs, then the stripping of stars acting on satellites must be moderate. This conclusion is in line with what we obtained for the stripped fraction of stars, which is not high for stellar satellite matter. Simon (2019) found the result in agreement with previous estimates, such as from Kirby et al. (2013).

When considering the fraction of surviving satellites, regardless of whether the satellites are DM-only or hybrid, this is not the feature that determines their survival. In fact, no systematic differences were found between the MJ16 simulation sample and our simulation sample. The inner properties of the satellites, as previously stated, differ in the shape of their density profiles, shallower for DM in hybrid satellites than in DM-only satellites. However, the difference in slope of these profiles is limited, and the energy distribution of DM particles is similar for DM-only and hybrid satellites. Instead, it seems that other drivers, such as the satellite ICs of our simulations, determine the survival probability of the satellites; therefore, this is related to their orbital parameters and intrinsic structure.

The fact that the tidal stripping exerted by the MW is not strongly efficient on its satellite galaxies seems to be compatible with what Peñarrubia et al. (2008) found in their simulations. In particular, they found that even after 99% of the stars are stripped from a satellite, the King profile (King 1966) of the remaining stellar component remains unchanged. Furthermore, they found that the stripping of stars is efficient only when the satellites approach their orbital periapsis, i.e. when they get closer to the MW centre. Previous work from Bullock & Johnston (2005) that has investigated the effect of MW–satellite in-

teractions in the past epochs has underlined the importance of these mergers to form the stellar halo. However, they adopted a combination of methods and semi-analytical models to address their study. The MW, for instance, was added only analytically as a time-evolving potential. Here we have taken advantage of full N-body simulations, and the live evolution of the gravitational potential of the MW, with effects such as dynamical friction (Chandrasekhar 1943) being naturally incorporated, however without secular long-term growth. Furthermore, our analysis is different from that of Bullock & Johnston (2005) in the sense that it focuses on the current distribution of the residual debris coming from recently accreted satellite structures rather than focusing on the build-up of the MW halo from past accretion processes.

3.5 Estimating the approximation done with the tidal radius calculation

The satellites tidal radii were calculated at each snapshot with Equation (3.2), where for the potential Φ I employed the DM halo Hernquist potential

$$\Phi_{\text{hern}}(r) = -G\frac{M_{\text{tot}}}{(r + a_{\text{hern}})}, \tag{3.12}$$

with M_{tot} the total halo mass and with a_{hern} the halo scale radius (Hernquist 1990). By doing this, the contributions of the disc and of the bulge to the total potential are neglected. However, the Galactic disc and bulge are dynamically dominating in the few inner kpc. An estimate of how large the approximation of neglecting them is[5], and of how much the inclusion of the disc and bulge potentials would impact, can be obtained by means of the relative difference

$$\frac{|\Delta r_{\text{tid}}|}{r_{\text{tid}}} = \frac{|r_{\text{tid,Hern+stellar}} - r_{\text{tid,Hern}}|}{r_{\text{tid,Hern}}}(r). \tag{3.13}$$

Here, $r_{\text{tid,Hern+stellar}}$ is the tidal radius estimated by taking into account the second derivative of the stellar potential as well, and $r_{\text{tid,Hern}}$ is the tidal radius estimated by only calculating the second derivative of the DM Hernquist halo potential. The stellar potential is calculated as

$$\Phi_{\text{star}}(r) = -G\Big(\frac{M_{\text{d}}}{r + a_{\text{d}}} + \frac{M_{\text{b}}}{r + a_{\text{b}}}\Big), \tag{3.14}$$

where $a_{\text{d}} = 2.8$ kpc and $a_{\text{b}} = 0.35$ kpc are the disc scale length and bulge scale radius, respectively. Here, the assumption and approximation is that the disc and the bulge are treated as spherical components, with a non-Keplerian distribution and with a scale radius, similar to a Hernquist-like profile.

---

[5]As already said, the other approximation is that the whole velocity modulus of the satellite was considered for the calculation of the corresponding angular velocity appearing in the tidal radius in Equation (3.2), thus approximating the orbit as circular.

In Figure 3.13 I show the second derivatives of the MW potential, both with and without including the stellar potential (top panel), the corresponding tidal radii (central panel) and their relative difference following Equation (3.13) (bottom panel), as functions of GCd. For the case of the tidal radius and of its relative difference, I plot the data for different values of satellite angular speed ω, ranging from 0 to 10^3 km s^{-1} kpc^{-1} (colours from red to grey). The calculation of the tidal radius is the same as in Equation (3.2). The example represented in the figure is for a satellite of mass $M_{\rm sat} = 10^9$ M$_\odot$ and for Aq-D2 only, since Aq-D2 is the simulation set-up from **MJ16** where the MW model presented intermediate, average properties among all the six set-ups.

First, as can be seen in the top panel of Figure 3.13, the potential second derivatives strongly diverge approaching the MW centre for the case where the stellar potential is included. Second, the tidal radius decreases by increasing ω (central panel), because ω appears at the denominator in Equation (3.2). However, when including the stellar potential in the calculation of the tidal radius, the second derivatives of the disc and of the bulge potential dominate the denominator of Equation (3.2), and the variation of the tidal radius close to the MW centre is stronger in this case, with no relevant dependence on ω.

Last, looking at the bottom panel of Figure 3.13, the fact that the two calculated potentials (with full stellar contribution and without any stellar contribution) are closer to each other at large radii implies a smaller relative difference between the corresponding tidal radii (relative difference down to 3×10^{-2} at $r = 100$ kpc). Instead, close to the MW centre, the tidal radius calculated with the additional full stellar contribution approaches zero, therefore the relative difference approaches ~ 1.

In conclusion, the larger is the approach to the MW centre, the larger is the divergence of the tidal radius calculation when employing the full potential with respect to the case of the Hernquist DM halo potential only. The error however is large ($\sim$ an order of magnitude or more) only in proximity of the MW centre (within few kpc). Given the random distribution of the satellites orbits in the six simulations and that in general the satellites are not expected to transit always so close to the MW centre in the simulations, the final result on the satellite stripped debris is not expected to be strongly affected by the approximation that we have done on the second derivatives of the MW potential when calculating the tidal radii of the satellites.
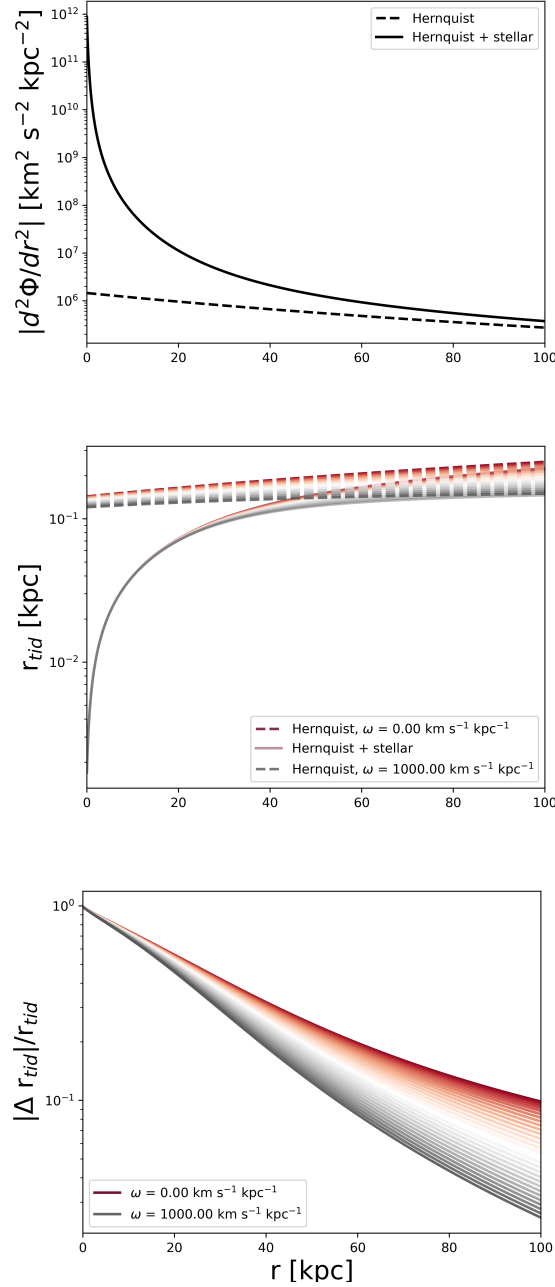
Figure 3.13: *Top panel*: potential second derivative for the case of the halo Hernquist potential only (dashed line) and for the case with the stellar potential included (full line), as functions of GCd. *Central panel*: tidal radius dependence on GCd for different angular velocities ω (from lower to higher ω, red to grey lines), for the case of the halo Hernquist potential only (dashed lines) and for the case with the stellar potential included (full lines). *Bottom panel*: relative difference between the tidal radii plotted in the central panel. Only the case of Aq-D2 is represented in all the three panels.

Chapter 4

A numerical study on the Milky Way bar

In this chapter, I present the collaborative research carried with Elena D'Onghia (University of Wisconsin, Madison WI, USA), Jose Alfonso Lopez Aguerri (Instituto de Astrofísica de Canarias, Tenerife, Spain) and Benoit Famaey (Observatoire Astronomique de Strasbourg, Strasbourg, France). The goal of this collaboration was to investigate the process of bar formation and the properties of the Galactic bar in a MW N-body model that is faithful to the observations of the Galaxy. Also, part of the goal was checking if there is any presence of vertical buckling instabilities and of the X-shape in the bar, and if there is any correlation between them.

In order to address the properties of the bar, we first needed to perform a Fourier analysis of the MW disc. In Section 4.1, I first introduce the principles of the Fourier analysis, useful to understand our study of the bar in the MW model. In the subsequent sections I then present the simulation and the results obtained so far in this collaboration.

As I already pointed out, the MW models employed for my numerical investigations in Chapter 2 and in Chapter 3 were the ones from **MJ16**. These MW models are stable against bar formation, while on the contrary the bar is observed in our Galaxy. The reasons for testing a MW model that matches the observational constraints of our Galaxy are different:

1. Improving the properties of the MW models from **MJ16** in order to reproduce bar formation;

2. Creating a new MW model with higher resolution that can be competitive against the MW-like galaxies formed in the state-of-the-art cosmological simulations;

3. Studying the formation and evolution of the bar in the MW, to understand how, given a MW model compatible with observations, the bar is predicted to develop and how it is predicted to impact on the surrounding environment;

4. Addressing the process of vertical buckling of the Galactic bar and if it has any correlation with the formation of the X-shape.

In particular, point 2) is understandable in the line of the increasing resolution that cosmological simulations of formation and evolution of MW-like galaxies are achieving, combined with the implemented refined baryonic physics prescriptions, as already discussed in Section 1.4.1. Here, the computational resources are not spent in the refined cosmological and baryonic recipes, but are spent for the detailed sampling of the mass distribution in the MW.

High resolution is important to properly address the resonances between MW halo particles and disc particles, that in turn are playing a role in the formation of instabilities like the Galactic bar. Another advantage of this kind of simulations is the possibility of focusing on ad-hoc models set to match the specific observational constraints of the MW, instead of dealing with the randomness of statistical samples of MW-like objects from large cosmological boxes.

4.1 Bar instability and buckling instability: Fourier analysis

I now summarise the methods to study the bar formation and the bar buckling instability via Fourier analysis.

4.1.1 Fourier transform

In the Fourier analysis, a function $f(x)$ of a continuous variable x can be expressed in terms of an infinite series of wave functions $\exp(-ikx)$, by integrating on all the wave numbers (or modes) k, with $k = 2\pi/x$, so that

$$f(x) = \frac{1}{\sqrt{2\pi}} \int_x \hat{f}(k)e^{-ikx}dk \,. \tag{4.1}$$

The element $\hat{f}(x)$ is the weight that the mode k has in reconstructing the signal $f(x)$. $\hat{f}(k)$ is the FT of $f(x)$, $\hat{f} \equiv F(f)$, evaluated on the frequency k, and $1/\sqrt{2\pi}$ is the normalisation factor. The FT of the FT is the function itself,

$$f(x) = F(F(f)) = F(\hat{f}). \tag{4.2}$$

4.1.2 Fourier analysis of numerical MW-like discs

The disc of a numerical MW model is a discrete distribution of particles. Each i-th particle P_i carries a quantity of matter m_i, and it is described by its position vector $\vec{R}_i$[1]. This distribution can be described by means of a kernel function,

$$W(\vec{R}) = \sum_i m_i \delta(\vec{R} - \vec{R}_i) \,, \tag{4.3}$$

---

[1]Where $\vec{R} = \sqrt{x^2 + y^2}$, since the disc lies on first approximation in the xy-plane.

where the function W is non-null only where $\vec{R}$ corresponds to any of the positions $\vec{R}_i$ of the particles. This is because of the convolution properties of the Dirac delta functional δ,

$$\int f(x)\delta(x - x_0)dx = f(x_0).$$ (4.4)

If we divide the disc in radial bins, each one being a radial ring centred on GCd R, we can define a function of polar coordinates (R, ϕ), where $\vec{R} \equiv (R, \phi)$, such that

$$W(\vec{R}) \equiv W(R, \phi) = \sum_{i,R} m_{i,R}\delta(\phi - \phi_{i,R}) \equiv W_R(\phi),$$ (4.5)

where the dependence on the radius vector is replaced by the dependence, at a fixed radius R, on the azimuth ϕ only. Here the index i, R is running on all the particles inside the radial bin centred on R and the terms $m_{i,R}$ are the masses of the particles inside the bin.

For each radial bin of centre R, we can decompose the signal $W_R(\phi)$ into an infinite series of wave functions of different modes. Each wave function represents a mode k of the FT of the mass distribution of the disc in that bin. Since the angle ϕ has periodicity 2π on the disc, then we can consider a infinite number of discrete modes $k = 0, 1, 2, ...$ For each of these modes, we can determine, along the whole disc, a function $A_k(R)$ such that

$$A_k(R) = C_k \int_0^{2\pi} W_R(\phi)e^{-ik\phi}d\phi = \hat{W}_R(k)$$ (4.6)

is the discrete FT of W, evaluated at the discrete mode k, and C_k is the corresponding normalisation constant. By substituting Equation (4.5) in Equation (4.6), then

$$A_k(R) = C_k \int_0^{2\pi} \sum_{i,R} m_{i,R}\delta(\phi - \phi_{i,R})e^{-ik\phi}d\phi =$$

$$C_k \sum_{i,R} m_{i,R} \int_0^{2\pi} \delta(\phi - \phi_{i,R})e^{-ik\phi}d\phi = C_k \sum_{i,R} m_{i,R}e^{-ik\phi_{i,R}}.$$ (4.7)

If $k = 0$, Equation (4.7) becomes

$$A_0(R) = C_0 \sum_{i,R} m_{i,R} = C_0 M_R,$$ (4.8)

where M_R is the total mass of the bin centred on R. Thus, the mode $k = 0$ is associated to the total disc mass in the ring. By imposing that the mode A_0 is normalised to unity, we have $C_0 = 1/M_R$. For modes $k > 0$, the contribution of the terms $e^{-ik\phi_{i,R}}$ in each radial bin is such that

$$\sum_{i,R} |m_{i,R}e^{-ik\phi_{i,R}}| \leq \sum_{i,R} m_{i,R} = M_R$$ (4.9)

for each particle $P_{i,R}$. Therefore, by imposing the same condition on the constants C_k for $k > 0$, i.e. $C_k = 1/M_R$, we obtain that the corresponding Fourier terms are $A_k \leq A_0$, i.e. we can normalise the higher order modes to equal or less than unity.

4.1.3   Bar instability

Galactic bars are axisymmetric structures. The mode that describes these structures and other features like spiral arms by means of the Fourier analysis is the mode $k = 2$ (**BT08**). Following Equation (4.7), the corresponding FT defined at GCd R has the form

$$A_2(R) = \frac{1}{M_R} \sum_{i,R} m_{i,R} e^{-i2\phi_{i,R}} . \tag{4.10}$$

For each $i-$th particle, the exponential term in Equation (4.10) is a complex number, and can be rewritten as the sum of a real part and an imaginary part,

$$e^{-i2\phi_{i,R}} = \cos(2\phi_{i,R}) + i \sin(2\phi_{i,R}) . \tag{4.11}$$

Let $\mathrm{Re}_2(R)$ and $\mathrm{Im}_2(R)$ be the sums over all the real parts and all the imaginary parts,

$$\begin{cases} \mathrm{Re}_2(R) = \sum_{i,R} \cos(2\phi_{i,R}) \\ \mathrm{Im}_2(R) = \sum_{i,R} \sin(2\phi_{i,R}) . \end{cases} \tag{4.12}$$

Then,

$$\begin{cases} |A_2(R)| = \frac{1}{M_R} \sqrt{\mathrm{Re}_2^2(R) + \mathrm{Im}_2^2(R)} \\ \Phi_2(R) = \mathrm{atan2}(\mathrm{Im}_2(R), \mathrm{Re}_2(R)) , \end{cases} \tag{4.13}$$

where $|A_2(R)|$ is the magnitude of $A_2(R)$ in the bin R and $\Phi_2(R)$ is the corresponding phase angle[2].

For the case of the bar, then, $\Phi_2(R)$ is the angular orientation of the semi-major axis of the bar in the given bin centred on R. The bar strength is the maximum value of $|A_2(R)|$, and I indicate it here as $A_{2,\mathrm{max}}$. R_{max} is the corresponding radius of maximum $|A_2(R)|$. Also, I indicate simply with Φ the bar phase angle at the radius R_{max}, as the phase angle representative of the whole bar orientation in the Galactic disc.

As an additional note, the same Fourier term $A_2(R)$ cannot disentangle different modes at the same radius, and the coefficient $A_2(R)$, for instance, can be sensible to both bar and spiral features. However, different features and instabilities evolve with different pattern speeds and survive on different timescales. Thus, in order to disentangle the different contributions to the coefficient, it is helpful to do a time-dependent analysis of $A_{2,\mathrm{max}}$. Another aspect that helps the analysis of the bar growth shown below is that I focused on the region within 5 kpc of GCd, i.e on the region where the bar dominates after forming. This helped rule out external perturbations that could have contaminated further the signal in the Fourier analysis and in the study of the bar properties.

---

[2]The function $\mathrm{atan2}(\mathrm{Im}_2(\mathrm{R}), \mathrm{Re}_2(\mathrm{R}))$ is the arctangent $\arctan(\mathrm{Im}_2(\mathrm{R})/\mathrm{Re}_2(\mathrm{R}))$ evaluated to extend the angle at any quadrant. The angle is returned in radians in the range $[-\pi, +\pi]$. An example of numerical implementation of the function in C++ can be found in the page https://en.cppreference.com/w/cpp/numeric/math/atan2.

4.1.4 Buckling instability

Buckling instabilities in a bar appear in the form of vertical bendings that alter the symmetry of its distribution with respect to the Galactic plane. If we centre a coordinate frame on the disc, and we rotate the coordinate frame by the angle Φ that the bar forms with the $x-$axis, the new x-axis lies then on the direction of the bar major axis, the new y-axis lies on the direction orthogonal to it, always on the disc plane, and the z-axis always lies orthogonal to the disc plane.

Projecting all the particle coordinates on this new coordinate frame, we can now perform another Fourier analysis, this time on the new xz-plane, in order to catch the bar buckling instability. Since the buckling instability is a vertical asymmetry in the distribution of the bar with respect to the Galactic plane, the Fourier coefficient corresponds to the first mode $k = 1$ of the matter distribution in the xz-plane, in the form

$$B(R_{xz}) = \frac{1}{\pi M_{R_{xz}}} \sum_{i,R_{xz}} m_{i,R_{xz}} e^{-i\theta_{i,R_{xz}}} \ , \tag{4.14}$$

as in Martinez-Valpuesta & Athanassoula (2008). Here, R_{xz} is the radius in the xz-plane, $R_{xz} = \sqrt{x^2 + z^2}$, and i, R_{xz} is the index running on all the particles inside the ring-like bin in the xz-plane with central radius R_{xz}. Also, $\theta_{i_{R_{xz}}}$ is the corresponding angle of the particle, calculated on the xz-plane from the positive x-axis, and $M_{R_{xz}} = \sum_{i_{R_{xz}}} m_{i_{R_{xz}}}$ is the total mass in the bin centred on radius R_{xz}.

Again, being $B(R_{xz})$ a complex coefficient, its magnitude (i.e the intensity of the bar buckling) at each ring-like bin is $|B(R_{xz})|$, similarly to the first of the Equations (4.13). I will simply call B the intensity of the buckling.

A second way of calculating B is using Equation (4.14), summing on all particles inside a parallelepipedic region elongated on the direction of the bar semi-major axis (Martinez-Valpuesta et al. 2006; Martinez-Valpuesta & Athanassoula 2008). This parallelepipedic region is chosen to enclose the bar, avoiding contamination in the FT from particles outside of it. This calculation of the coefficient B can be used as indicative of the intensity of the buckling in the whole bar region. We opted for this second approach, as I will show below.

4.2 Bar evolution in a MW model

4.2.1 Milky Way: numerical set-up and initial conditions

A high-resolution N-body MW model, with a disc of 24M particles, a bulge of 8.4M particles, and a DM halo of 60M particles, was realised by E. D'Onghia. This is the N-body model that we used in order to address the evolutionary properties of the MW bar and to check its impact on the local Galactic disc.

The model was realised using the package makeNewGal of V. Springel (see Springel et al. 2005a), in a similar way to the MW models of **MJ16** employed in Chapter 2 and in Chapter 3. The MW model parameters are originally reported in D'Onghia & Aguerri (2020). These parameters were chosen in order

to match the observational properties of the MW described in **BHG16**. In Table 4.1 I show the relevant parameters of the model.

Table 4.1: Relevant parameters of the MW model realised by E. D'Onghia. From top to bottom: halo mass, Hernquist scale radius, maximum circular velocity, radius of maximum circular velocity, disc mass, disc scale length, disc scale height, bulge mass, bulge scale radius, number of disc, bulge and halo particles.

M_{h}	$9.50 \times 10^{11}\ \mathrm{M_\odot}$
a	30 kpc
v_{max}	233.65 km s^{-1}
r_{max}	7.39 kpc
M_{d}	$4.83 \times 10^{10}\ \mathrm{M_\odot}$
h	2.67 kpc
z_0	0.32 kpc
M_{b}	$8.06 \times 10^{9}\ \mathrm{M_\odot}$
a_{b}	0.120 kpc
N_{d}	24M
N_{b}	8.4M
N_{h}	60M

The DM halo was built again with the best-matching Hernquist profile having a similar inner density cusp as the corresponding NFW profile. The Hernquist total mass is compatible with the value of mass enclosed within r_{200} estimated by **BHG16**, $M_{200} = (1.1 \pm 0.3) \times 10^{12}\ \mathrm{M_\odot}$. Thus, the halo has a Hernquist density profile as in Equation (1.4) and its scale radius is related to the corresponding NFW scale radius according to Equation (1.8). The bulge follows a Hernquist density profile as well. The disc density has an exponential profile like in Equation (1.1) and again with $P = 1$.

In Figure 4.1 I show the initial projected mass surface density map of the disc (the central panel, the top panel and the right panel correspond to the xy-, the xz- and the yz-projections, respectively). The ICs model, as can be seen, is axisymmetric and shows no bar and no spiral features. This map (and the ones in Figure 4.4 for the subsequent snapshots) was created with square bins of 0.1 kpc side each and by imposing a lower mass cut-off of $2 \times 10^4\ \mathrm{M_\odot}$ in each bin (i.e. with at least 10 particles in each bin), in order to avoid the contamination from the noise, that below this mass threshold would become increasingly relevant. As can be seen later in Figure 4.4, this threshold is also enough to show the different structures developing in the disc: the bar, the symmetric vertical X-shape of the bar, the spiral features and the ring-like density waves.

The initial MW rotation curve, calculated as in Equation (1.3), is shown in the left panel of Figure 4.2 with a full line. Here the total circular velocity enclosed within a GCd R is coming from the contribution of three terms: the disc mass (dot-dashed line), the bulge mass (sequence of triangles) and the DM halo mass (dotted line). For the calculation of the contribution of the disc to the circular velocity, $V_{\mathrm{circ,d}}$, I used the approximation that the disc is spherically distributed within each radius R.
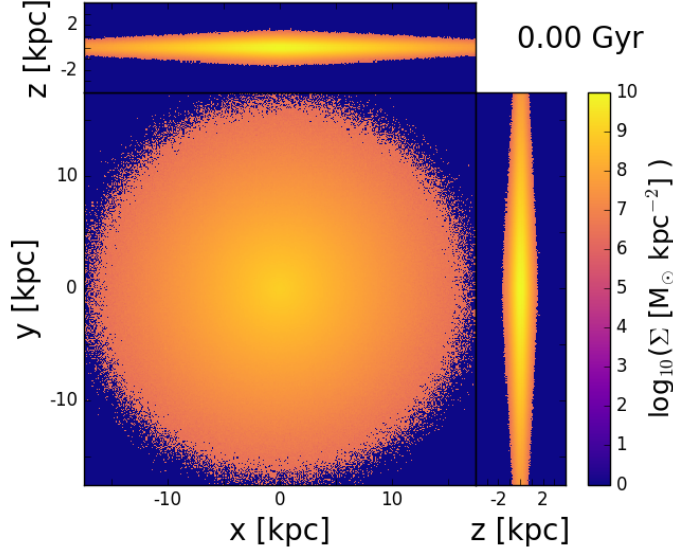
Figure 4.1: Surface density map of the ICs MW disc. The central, top and right maps correspond to the xy-, xz- and yz-projections of the disc mass surface density. Colour codes as in the colour bar.

The right panel of Figure 4.2 is a zoom of the left panel into the first 20 kpc of GCd. In the right panel I have also added the mean tangential velocity profile of the disc particles, v_ϕ, as a dashed line. For comparison with the total MW rotation curve that I have calculated, I additionally plotted (red dashed line) the initial MW rotation curve where I considered for the disc its actual exponential density profile (Freeman 1970), and not the spherical density profile approximation. Following Springel et al. (2005a), in fact, the square circular velocity coming from the contribution of the disc exponential profile is

$$V_{\mathrm{circ,exp}}^2(R) = \frac{2GM_{\mathrm{d}}}{h}\left(\frac{R}{2h}\right)^2\left[I_0K_0 - I_1K_1\right],\qquad(4.15)$$

with I_0, K_0, I_1, K_1 being the Bessel functions evaluated at $(R/2h)$. Therefore, having assumed a spherical density distribution for the disc mass in the calculation of the rotation curve by means of Equation (1.3), we have obtained an approximation of the actual V_{circ}.

Having used the disc spherical mass in the calculation of $V_{\mathrm{circ,d}}$, we underestimate the actual peak of $V_{\mathrm{circ,exp}}$ by a fraction 15% of its value (**BT08**). However, the relative difference of the total rotation curve V_{circ} (black line in the right panel of Figure 4.2), calculated with the spherical disc assumption, to the actual rotation curve calculated including the effective disc exponential density profile (red dashed line), is of no more than $\sim 10-11\%$ in the first kpc of GCd, and it drops immediately to less than 6% at less than one disc scale length. Thus, though not representing the actual rotation curve, the assumption of a spherical distribution of the disc in Equation (1.3) returns a good approxima-

tion of V_{circ}. I therefore refer to our approximated estimate of the rotation curve simply as V_{circ}.

At large radii (up to the virial radius), the circular velocity is dominated by the DM halo. The disc dominates the region within the first ~ 5 kpc of GCd, while the bulge is relevant only within the first kpc of GCd.

The tangential velocity is much lower than V_{circ} in the first few kpc, where the difference reaches up to $\sim 60 - 70$ km s^{-1}. This is because of the bulge, that imposes non-circular and radial orbits in the centre of the MW, due to its spherical potential. For the rest of the disc extent, the fact that the circular and tangential velocities are similar is indicative of an initially low asymmetric drift (**BT08**) in the model. At a GCd $R_0 = 8.2$ kpc, that **BHG16** used as the GCd of the Sun, our value of $V_{\mathrm{circ}} \sim 230$ km s^{-1} is compatible with their value, that is $V_{\mathrm{circ},R_0} = 238 \pm 15$ km s^{-1}.
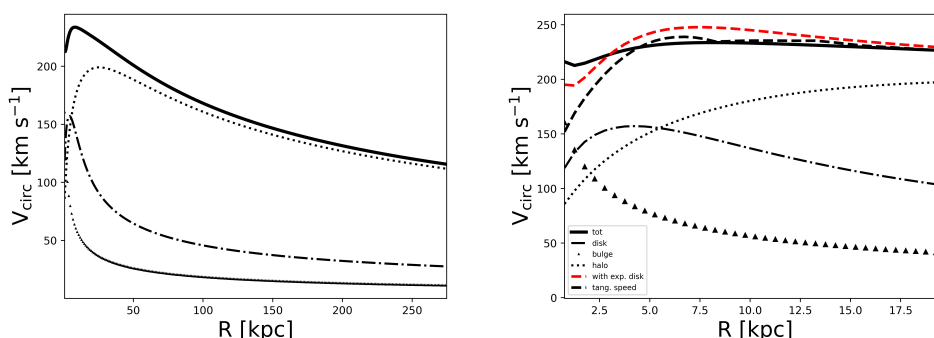
Figure 4.2: *Left panel*: rotation curve at the beginning of the simulation. The full line is the circular velocity profile resulting from the contribution of all the three components (disc, bulge, and halo). The dot-dashed line is the profile resulting from the contribution of the disc, the sequence of triangular markers represents the contribution of the bulge and the dotted line is the contribution of the halo. The radial bins have 0.5 kpc thickness. *Right panel*: zoom in the first 20 kpc. The additional black dashed line is the initial disc tangential velocity profile. The additional red dashed line instead is the initial actual total circular velocity, calculated considering the actual distribution of an exponential disc and not using the spherical mass distribution approximation for it.

The spherical bulge employed here to construct the IC has a lower mass than in **BHG16** ($\sim 8 \times 10^9$ M$_\odot$ in this model versus $\sim 1.6 \times 10^{10}$ M$_\odot$ from literature). This bulge can be considered a classical bulge. This is in accordance with the fact that the classical bulge mass estimated from literature is smaller than the total measured bulge mass, as I recalled in Section 1.2.2.

The fact that we started already with a classical bulge in the simulation is justified by the fact that this initial set-up is not directly coming from a cosmological simulation, but it is made with the purpose of building an isolated model, where the disc can easily develop instabilities and fragmentation if it is massive enough like in this case (see for instance Toomre 1964). In this sense, the presence of the bulge has a stabilising effect on the disc. Additionally, D'Onghia & Aguerri (2020) noted that the bulge in this model does not rotate, contributing to slow down the bar and to increase its exchange of angular momentum with the environment.

4.2.2 Numerical simulation

The simulation[3] was run by E. D'Onghia for a total of $4\,\mathrm{Gyr}$[4] at the La Palma supercomputer centre [5]. It was run with the code GADGET-3 using 225 CPUs in parallel, again adopting `MPI` prescriptions for the parallelisation of the code. Snapshots were taken every $5\,\mathrm{Myr}$, in order to track all the evolutionary steps of the bar with a high temporal resolution, small enough to catch any possible vertical buckling event. More information about the simulation parameters is found in D'Onghia & Aguerri (2020).

For each snapshot, before analysing the properties of the disc and of the bar, I first calculated the MW density centre, then I rescaled the disc particle coordinates and velocities to the ones of the MW density centre, and I rotated them to have the total disc angular momentum vector lying in the z-direction. This procedure is the same as the one employed in Chapter 2 and in Chapter 3 before analysing the corresponding simulations.

4.2.3 Radial density waves in the Milky Way model

As a final consideration on the construction of the numerical MW models described here and in the previous chapters of this thesis, let us consider again the radial propagation of ring-shaped density waves in the numerical Galactic disc. For the case of the MW model employed in this chapter, these density waves can be observed in the xy-projected surface density maps of the disc in Figure 4.4 and in the evolution of the disc surface density profile in Figure 4.8. As I already noticed in Chapter 2, these density waves are found also in the isolated evolution of the MW model of **MJ16**.

At least comparing the numerical set-up of **MJ16** and the one discussed here, it appears that the production of these density waves is independent from the presence of the bar in the disc. In fact, in the models of **MJ16** no bar forms. Thus, this comparison indicates that the ring-shaped density waves most likely are a numerical artefact of the ICs, and they are an effect of the relaxation of the numerical MW disc, that moves to a new equilibrium DF, starting from the ICs equilibrium DF, and independently from the gravitational instabilities that the disc develops.

The presence of these waves poses some problems related to the construction of MW numerical models with discs in an initial equilibrium DF. This requires future investigation, either checking for proper modifications to the algorithms employed in the codes `GalIC` and `makeNewGal`, or alternatively understanding under which conditions and selections of parameters the MW models generated with these two packages do not develop these radial density waves.

---

[3]The simulation was named GALAKOS by D'Onghia & Aguerri (2020), after the ancient Greek for "Galaxy".

[4]I was able to access the data corresponding to the first $3.84\,\mathrm{Gyr}$. However, for the sake of the discussion in this chapter, these $3.84\,\mathrm{Gyr}$ are way enough to show the relevant evolutionary properties of the MW disc and of the bar.

[5]Information about the cluster can be found at http://www.iac.es/en/science-and-technology/technology/technical-facilities/lapalma-supercomputer.

4.3 Bar: evolutionary properties

First, I discuss the process of bar growth and evolution. This is useful to understand the impact of bar growth on the secular evolution of the inner disc kinematics and dynamics.

4.3.1 Bar formation and growth

To quantify the growth of the bar, I calculated $A_{2,\max}$ in the disc as a function of time, from the beginning of the simulation to $t = 3.84$ Gyr. In the left panel of Figure 4.3, I show the evolution of $A_{2,\max}$ in time. For each snapshot, I smoothed $A_{2,\max}$ by averaging it together with the previous and subsequent snapshot. $A_{2,\max}$ shows an exponential increase from the beginning of the simulation up to $t = 0.5$ Gyr, where it reaches the value $A_{2,\max} \sim 0.2$, entering the strong bar regime. Afterwards, the bar slowly grows and steadily persists in the disc until the end, as can be seen also from the xy-projected density maps of the MW disc in Figure 4.4. From now on, I adopt $t = 0.5$ Gyr as the initial time of secular bar evolution.

In the right panel of Figure 4.3, I show the evolution of $R_{\max}$ in time. For each snapshot, I smoothed $R_{\max}$ like I did with $A_{2,\max}$. The $A_2(R)$ coefficient is sensitive to other disc perturbations, such as spiral structures. Therefore, particularly at the first epochs and until $t \sim 1$ Gyr, the fact that $R_{\max}$ is placed at $\sim 4 - 5$ kpc, even if the bar is still not fully developed, may reflect the contamination of other, more external perturbations in the disc. After the first Gyr, anyway, when the bar grows significantly the evolution of $R_{\max}$ is more regular and $R_{\max}$ slowly increases from ~ 1.5 kpc to a final value of ~ 2.5 kpc. The peaks of minimum $R_{\max}$ that are visible at $t \sim 0.7$ Gyr and $t \sim 1.1$ Gyr may be due to noise in the signal of the forming bar, as I will discuss when addressing the bar pattern speed and the corotation radius (Section 4.3.2).
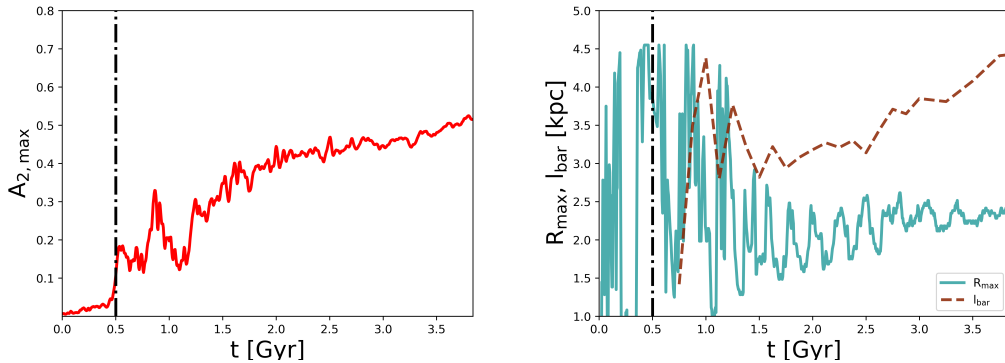
Figure 4.3: *Left panel*: Evolution in time of the bar strength $A_{2,\max}$ (left panel). *Right panel*: Evolution in time of the radius of maximum strength $R_{\max}$ (full dark cyan line) and of the bar length l_{bar} (dashed brown line). In both panels the vertical dot dashed black line marks the epoch of bar formation at $t = 0.5$ Gyr.

Always in the right panel of Figure 4.3 I show the bar length l_{bar}, that was

calculated by J. A. L. Aguerri[6], following the prescriptions of Aguerri et al. (2000). For the bar length, I took data every 125 Myr until $t = 3$ Gyr, and then every 250 Myr, to display it as regularly as possible, given the fewer data points that I was provided. However, they are still enough to capture the general evolution of l_{bar}. The first peak of bar length, $l_{\text{bar}} \sim 4.4$ kpc, appears at $t \sim 1.0$ Gyr, while R_{max} is ~ 4.5 kpc already at 0.5 Gyr. This confirms that other perturbations in the disc may influence the early growth of $A_{2,\text{max}}$ until the bar does not overcome their strength in the subsequent epochs.

Another feature to note is that, after $t \sim 1$ Gyr, i.e. after the bar has started to dominate in the disc, the value of l_{bar} is always higher than R_{max}, reaching a final ratio $l_{\text{bar}}/R_{\text{bar}} \sim 2$. This is a confirmation that the maximum of $A_2(R)$ falls inside the bar range, i.e. this maximum is due to the contribution in strength of the bar.

For comparison, in Figure 4.4 I show the evolution of the disc mass surface density, visualised through maps as in Figure 4.1. At a time $t = 0.5$ Gyr (top left map), the bar is still not developed in the centre of the disc, with corresponding low levels of mass density (see the corresponding xy-projection). Thus, the bar seed is still small in terms of dominance in the disc. Instead, visible spiral features have already developed by that time. Subsequently, the bar increases in strength and length (top right map and all the maps below; higher density values in the centre of the corresponding xy-projection and visibly higher extent of the bar feature). Already at $t = 1.0$ Gyr the spirals are a fading feature, in comparison to the bar.

To sum up, the presence of the spiral patterns at $t = 0.5$ Gyr extending further than the bar can offer an explanation for the higher value of l_{bar} and R_{max} obtained at early epochs, while the bar is still small. The $A_{2,\text{max}}$ coefficient is first influenced by spiral features and around 1.0 Gyr the bar dominates the contribution to $A_{2,\text{max}}$, that grows to its final value of ~ 0.5 and falls inside the bar region.

4.3.2 Bar pattern speed and corotation radius

Pattern speed

The bar pattern speed Ω_{bar} was calculated at each time t as

$$\Omega_{\text{bar}}(t) = \frac{\Phi(t + \Delta t) - \Phi(t)}{\Delta t} \, , \tag{4.16}$$

with Δt being the time difference between the snapshot at time t and the subsequent snapshot. In this case, $\Delta t = 0.005$ Gyr. In Figure 4.5 I show the bar phase angle Φ (left panel) and the pattern speed Ω_{bar} (right panel) as functions of time[7]. The values of Φ and Ω_{bar} were smoothed again like for the case

---

[6]J. A. L. Aguerri gently allowed me to plot and show the bar length evolution in time.

[7]I performed the calculation of Φ with two Matlab routines, `bar_fit.m` and `fit_ellipse.m`, gently provided by Evgeny Polyachenko (Institute of Astronomy of the Russian Academy of Sciences, Moscow, Russian Federation). These routines require as input the projected matter
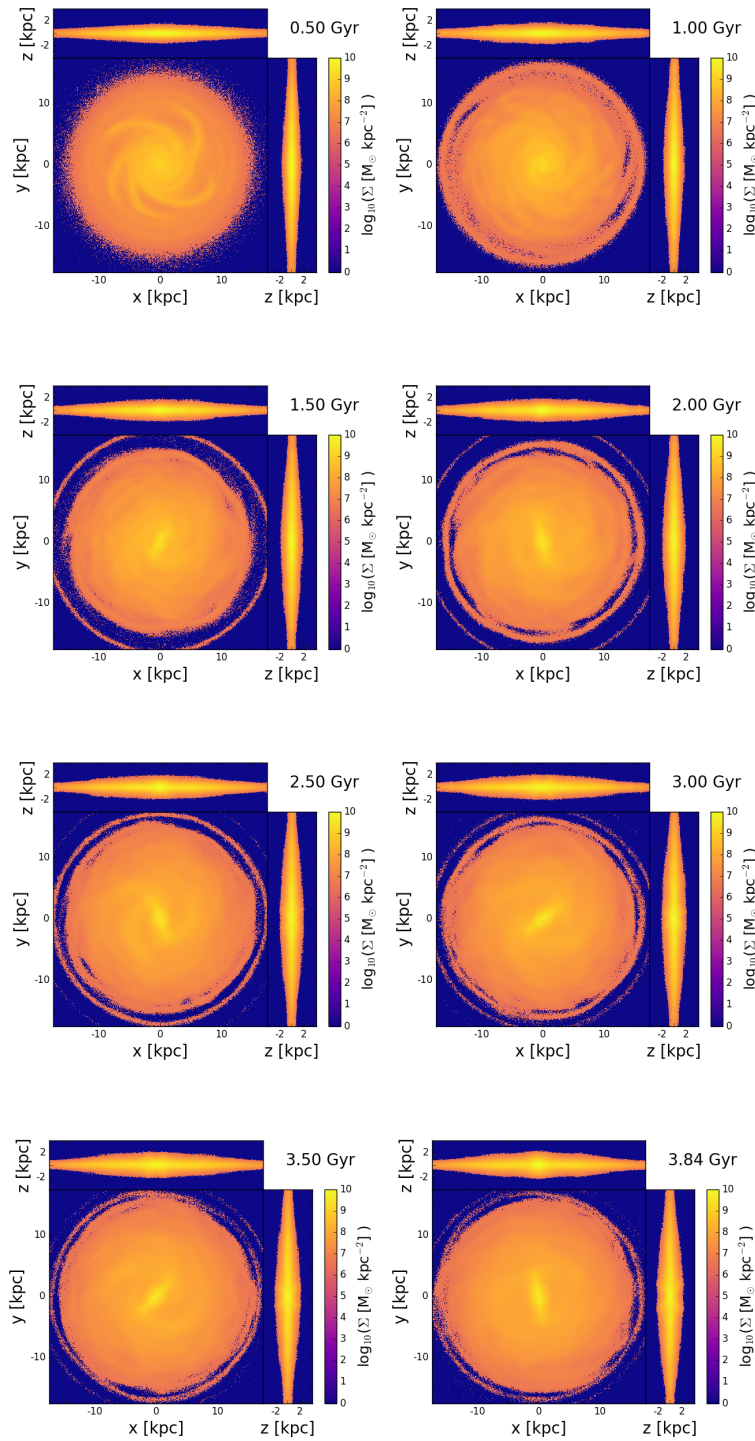
Figure 4.4: Maps showing the evolution of the disc surface density, every 0.5 Gyr from $t = 0.5$ Gyr until $t = 3.5$ Gyr (top to bottom line, left to right column for each line) and with the addition of the map taken at $t = 3.84$ Gyr (bottom right panel). For each plot, the projections are as in Figure 4.1 and the colour codes are as in the corresponding colour bars.

distribution of the disc in the xy-plane and return elliptical contours that fit this matter distri-

of $A_{2,\mathrm{max}}$, i.e. averaging each value at every time with the previous and following values.
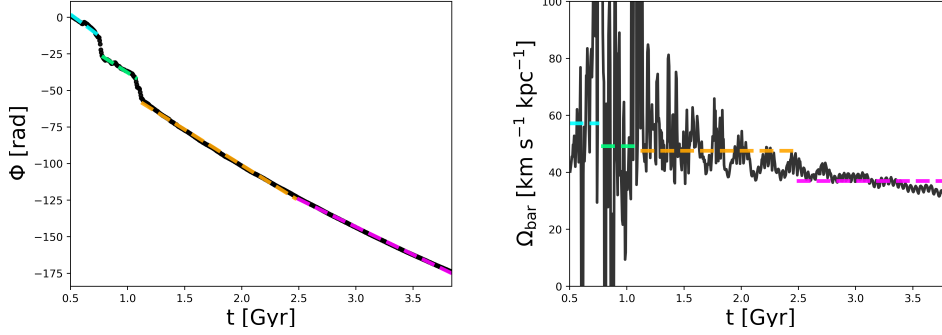
Figure 4.5: *Left panel*: bar phase angle as a function of time. The black dots mark the corresponding values of phase angle Φ at the given times. The four coloured dashed lines (cyan, spring green, orange and magenta) represent the corresponding best-fit linear functions to Φ as functions of time, during the corresponding time intervals. *Right panel*: bar pattern speed Ω_{bar} as a function of time (full black line). The four characteristic bar pattern speeds of the four time intervals, obtained from the corresponding best-fit linear functions, are plotted as horizontal dashed lines with the same colours as in the left panel.

Excluding a few data points, the evolution of Φ can be distinguished in four separate time intervals, each characterised by a linear increase of the angle in time, i.e. characterised by constant Ω_{bar}. Therefore, I calculated the corresponding linear functions that better fit the values of Φ in these four regions. Between the first and second period of time, and between the second and third period of time, there are some jumps in Φ (see below the discussion on the early sources of noise). I skipped the times around these jumps, to better fit the data in the four time intervals. The third and fourth time interval are connected, with no jump in Φ in between.

Each best-fit linear function has the form

$$\Phi(t) = \dot{\Phi} \times (t - t_{\mathrm{i}}) + \Phi_0 \,, \tag{4.17}$$

where t_{i} represents the initial time of the corresponding interval, Φ_0 represents the phase angle at the time $t = t_{\mathrm{i}}$, and the value $\dot{\Phi} \equiv \Omega_{\mathrm{bar}}$ represents the characteristic angular speed in the corresponding time interval. In the left panel of Figure 4.5 these four best-fit functions are plotted as cyan, spring green, orange and magenta dashed lines, in order of corresponding time interval.

In Table 4.2 I report the best-fit parameters for the linear interpolation of the data in the four epochs, including the rotational period of the bar in the corresponding time intervals, where the rotational period is defined as $T = 2\pi/\Omega_{\mathrm{bar}}$. The angular speed was inverted in sign, in order to orient it positively with the bar rotation verse. The average bar pattern speeds are decreasing from the beginning of the simulation, starting with a maximum $\Omega_{\mathrm{bar}} = 57.26$ km s^{-1} kpc^{-1} and reaching a minimum $\Omega_{\mathrm{bar}} = 37.04$ km s^{-1} kpc^{-1} after $t = 2.5$ Gyr.

bution, as well as the parameters that describe these ellipses, including the phase angles.

Table 4.2: Best-fit parameters of the linear functions representing the bar pattern speed in the four time intervals. From left to right, time interval, bar pattern speed $\dot{\phi} \equiv \Omega_{\mathrm{bar}}$, bar phase angle Φ_0 at the beginning of the given time interval, bar rotational period T.

Time interval (Gyr)	Ω_{bar} (km s^{-1} kpc^{-1})	Φ_0 (deg)	T (Myr)
$[0.5, 0.76]$	57.26	115.47	107.54
$[0.77, 1.1]$	49.29	281.98	124.94
$[1.13, 2.51]$	47.64	263.60	129.26
$[2.51, 3.94]$	37.04	105.13	166.25

In the right panel of Figure 4.5, I show (black full line) the evolution of the bar pattern speed as a function of time. I also plotted the four rotation speeds corresponding to the four time intervals, with the same colours as in the left panel.

I focused on the range of angular velocities 0 km s^{-1} kpc^{-1} $< \Omega < 100$ km s^{-1} kpc^{-1}, since the high-speed and low-speed/negative-speed peaks appearing out of this range are most probably due to noise, as I said before when considering the corresponding minima in R_{max}. Specifically the high-speed peaks at $t \sim 0.7$ Gyr and $t \sim 1.1$ Gyr are associated with the rapid variation of bar angle seen in the left panel of Figure 4.5. These high peaks in Ω_{bar}, given the corresponding minima in R_{max}, may be due to noisy features temporarily developing in the still weak bar. Instead, the low-speed/negative-speed peak of Ω_{bar} at $t \sim 0.85$ Gyr (not fully visible because of the cut in the plot) may be due to noisy, external perturbations, given that at the same time R_{max} has a local maximum (see again the right panel of Figure 4.3). These are connected to the small decrease in bar phase angle at $t \sim 0.85$ Gyr (again, left panel of Figure 4.5).

Therefore, in the right panel of Figure 4.5 it is confirmed that the first epoch (i.e. until ~ 1 Gyr) is dominated by oscillations in Ω, because of the mixed contribution of the already discussed early spirals and features in the disc and of occasional noisy signals. When the bar becomes dominant, these sources do not affect anymore Ω, that is then clearly associated to Ω_{bar} and decreases until the end of the simulation.

Comparing Figure 4.5 and Figure 4.3, an additional thing can be noticed. After $t = 1$ Gyr the values of R_{max} and the values of Ω_{bar} start to oscillate on similar timescales, in the range $\sim 200 - 300$ Myr.

In their analysis of the evolution of the bar in MW-like numerical models, Hilmi et al. (2020) showed that there is coupling between the oscillations in Ω_{bar} and the oscillations in l_{bar}, and that this is due to the interaction of the bar with the spiral structures in the disc. Though the spiral-like features fade after $t \sim 1$ Gyr, in the disc of our model there are still sub-dominant, external features at later times (see the features visible in the density maps of Figure 4.4 corresponding to the times $t > 1$ Gyr), and they can possibly explain these oscillations in R_{max}. Also, Hilmi et al. (2020) distinguished the effects of the bar-spirals coupling for the case of fast bars, where the oscillations in l_{bar} happen

with peaks distant ~ 60 Myr in time, and the case of slow bars, where the peaks are distant ~ 200 Myr in time. For our bar, these oscillations have a timescale that increases from ~ 200 Myr at $t = 1.5 - 2.0$ Gyr to ~ 300 Myr towards the end, putting our bar in line with the classification of slow bars of Hilmi et al. (2020), though with a higher timescale of the oscillations in our case. This increase in the timescale of the oscillations could be due to the fact that, as the bar becomes stronger, its coupling with the external disc features becomes negligible. This may also explain the decreasing amplitude of the oscillations towards the end of the simulation (where by "amplitude" I indicate the difference between the crests and troughs in the value of an oscillating parameter).

In order to test if this kind of coupling explains the oscillations in the bar parameters, we need to track the detailed evolution of l_{bar} in all the snapshots, and to check for possible oscillations in l_{bar} as in Hilmi et al. (2020). The current sampling of the bar length reported in this chapter is incomplete for this goal and requires further analysis. Therefore, future work must be done to give a complete answer to the oscillations in R_{max}, Ω_{bar} and l_{bar}.

Corotation radius

In the top left panel of Figure 4.6 I show the results of the calculation of the corotation radius R_{corot}, i.e. the radius at which the bar pattern speed equals the angular speed of the disc. In addition to calculating R_{corot} using the average tangential velocity profile in the disc (results showed with a red dashed line), for comparison I also calculated it making use of the V_{circ} profile (results showed with a full blue line).

The value of R_{corot} is very similar in both cases and it increases in time. At the end of the simulation, it has increased enough to reach ~ 7 kpc. This is a consequence of the bar slowing down and matching the disc tangential velocity and V_{circ} at increasing radii. The oscillations in R_{corot} observable at $t > 1.5$ Gyr are due to the oscillations in Ω_{bar} and I refer to the above analysis of the bar pattern speed for their explanation.

The two minima of R_{corot} at $t \sim 0.7$ Gyr and $t \sim 1.1$ Gyr are connected to the corresponding high values of Ω_{bar}. The two high peaks of corotation radius between $t \sim 0.85$ and $t \sim 1.0$ Gyr are instead connected to the low-speed/negative-speed noisy features associated with the correspondingly high peak of R_{max}.

Thus, to sum up the discussion on these early minima and maxima in Ω_{bar}, R_{max} and R_{corot}, two high-speed noisy features develop inside the bar at $t \sim 0.7$ Gyr and $t \sim 1.1$ Gyr, and they move R_{max} and R_{corot} temporarily towards values of minimum. Instead, the low-speed/negative-speed noisy features, external to the bar, temporarily determine a maximum in R_{max} and R_{corot} at $t \sim 0.85$ Gyr.

As an example of comparison of the pattern speed of the bar with the disc tangential velocity and rotation curve, in the top right panel of Figure 4.6 I show the profile of tangential angular velocity Ω_{tan} (dashed line), as well as the profile of angular velocity Ω_{circ} calculated from V_{circ} (full line), at $t = 3$ Gyr. I also show the bar pattern speed at $t = 3$ Gyr corresponding to the fourth time
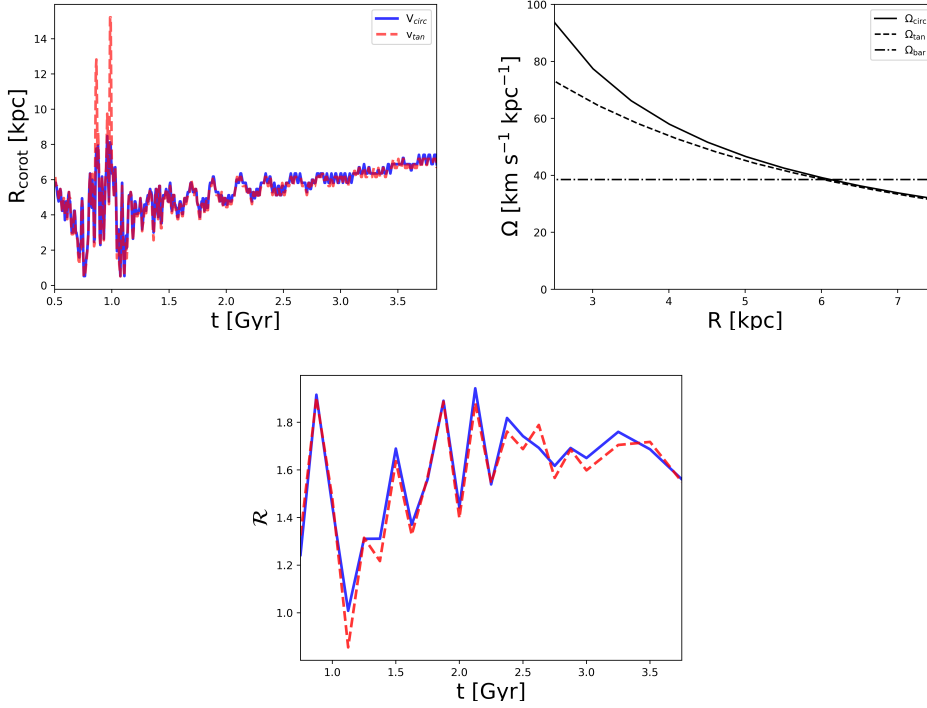
Figure 4.6: *Top left panel*: Bar corotation radius R_{corot} as a function of time. The full blue line is for the case of comparison of the bar pattern speed with the angular velocity associated to V_{circ}. The red dashed line is for comparison with the angular velocity associated to the disc tangential velocity. *Top right panel*: Radial profile of the tangential angular velocity (dashed black line) and the angular velocity associated to V_{circ} (full black line) at $t = 3.0$ Gyr, in comparison with the value of bar pattern speed of the third time interval (dot-dashed horizontal line, see again Table 4.2). *Bottom panel*: Ratio $\mathcal{R}$ between R_{corot} and l_{bar} as a function of time. Colour codes as in the top left panel.

interval in Table 4.2 (horizontal dot-dashed line in the plot).

The tangential velocity is always smaller than V_{circ} for the first few kpc of GCd. However, their values get similar at larger GCds, like at 6-7 kpc of GCd, where the tangential velocity is slightly larger than V_{circ}. This explains the fact that, for some snapshots, using the tangential velocity profile returns a higher R_{corot} than using V_{circ}.

However, with reference to the right panel of Figure 4.2, the actual initial circular velocity of the MW model is everywhere higher than the mean tangential velocity of the disc particles. Since V_{circ} is an underestimation of the rotation curve, using the actual rotation curve would probably return always a slightly higher value of R_{corot} than using the tangential velocity, though probably a similar one again - given the similarities of the initial tangential velocity and V_{circ} profiles with the actual rotation curve.

Last, in the bottom panel of Figure 4.6, I plot the ratio $\mathcal{R} = R_{\mathrm{corot}}/l_{\mathrm{bar}}$, i.e. the ratio between the bar corotation radius and the bar length. I used the same snapshots that I used to calculate l_{bar}. Again, I plotted $\mathcal{R}$ for both the cases of the corotation radius calculated using V_{circ} and using the tangential velocity. The result is that $\mathcal{R}$ overall increases from ~ 0.9 at $t \sim 1.0$ Gyr to ~ 1.6 at

$t = 3.25$ Gyr. For the early peaks I refer to the discussion above on the early noisy signals.

Our final values of $R_{\text{corot}} \sim 7$ kpc compare similarly to the ones found in **P15**, in the range $R_{\text{corot}} \sim 7.2 - 8.4$ kpc (see Section 1.5). At the same time, we obtained a value of $\mathcal{R} \sim 1.6$, which is in line with their estimate of $\mathcal{R} \sim 1.5 - 1.8$, and puts our MW in the group of the slow rotators, that **P15** claimed are not commonly found among external galaxies (see references therein). The result that the MW in our model is a slow rotator is also in line with the result from Polyachenko et al. (2016), where however they found higher final values of $\mathcal{R}$, i.e. $\mathcal{R} > 2$.

4.4 Bar: effects on the local MW kinematics and dynamics

In this section, I describe the impact of the bar on the MW disc, both considering dynamical effects on the disc mass distribution and effects on the MW kinematics. This is important to understand how relevant is the presence of the bar to determine the evolution of the disc.

4.4.1 Impact on the rotational kinematics and dynamics

We first evaluated the effects of the bar on the disc kinematics and dynamics, with particular focus on the disc tangential velocity profile and on the MW circular velocity profile. I chose a timestep of 0.5 Gyr for this analysis. This choice is adequate to get the main steps in the secular evolution of the disc, given that the typical dynamical timescale for the evolution of galaxies like the MW is of order $0.1 - 0.2$ Gyr.

I used again Equation (1.3) to calculate V_{circ}, with steps of 0.5 kpc in R. For the calculation of the tangential velocity v_{ϕ}, I divided the disc in radial bins of thickness 0.5 kpc and I calculated the mean tangential velocity of all the particles falling in those bins.

The evolution of V_{circ} and v_{ϕ} is shown in Figure 4.7, as a zoom into the first 20 kpc of GCd. After the bar develops, the inner profiles of V_{circ} and v_{ϕ} diverge in their evolution in the few inner kpc and throughout the simulation. V_{circ} increases in the inner MW as a consequence of the bar strengthening. The growth of the bar, in fact, produces an increase of the disc mass density within the few inner kpc, which translates in an increased dynamical support on V_{circ}. However, the tangential velocity decreases in time in the few inner kpc. This is because the bar imposes eccentric orbits, that are radially elongated and have a small tangential velocity component. This means that the bar has a non negligible effect on the dynamics and kinematics of the local MW after it forms. Towards the end of the simulation the difference between the inner profiles of V_{circ} and v_{ϕ}, while being initially of $\sim 60 - 70$ km s^{-1}, goes up to ~ 150 km s^{-1}.

In Figure 4.8 I show the density profile evolution of the disc (surface density) and of the halo (volume density) in the first 20 kpc of GCd. I chose the
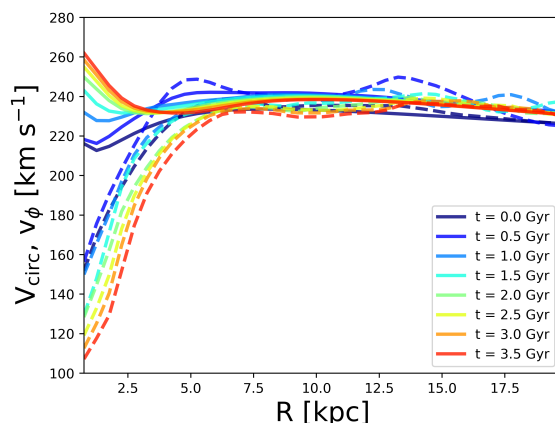
Figure 4.7: Evolution in time of the V_{circ} profile (full lines) and v_ϕ profile (dashed lines). From dark blue to red the lines represent snapshots from the time $t = 0$ Gyr to the time $t = 3.5$ Gyr, with timestep of 0.5 Gyr, as indicated in the label.

same timestep of 0.5 Gyr, starting from $t = 0$ Gyr, until $t = 3.5$ Gyr. For every snapshot, I used again a binning of 0.5 kpc to trace the density distribution of the two components. While the halo density profile remains mostly similar to the initial profile, in the case of the disc different effects are visible.

The first, that was already found in the MW model described in Chapter 2, is the presence of radial perturbations in the disc, that propagate towards the outer disc and make its surface density profile oscillate in time. I have already discussed these features in Section 4.2.3.

Second, in the inner regions, the disc surface density profile bends in time towards an inner peak and a convex knee between 2.5 and 7.5 kpc. This is a reflection of the increasing disc mass in the inner regions of the disc because of the formation of the bar, which makes matter fall towards the centre. Therefore, the major effect of the bar on the local MW dynamics is to increase the inner disc mass and to remove it from the intermediate GCds, shrinking and elongating the orbits to higher eccentricities.

4.4.2 Effects of the bar on the vertical kinematics

I now discuss the evolution of the disc thickness z_{rms}, vertical velocity dispersion σ_z and radial velocity dispersion σ_R, by plotting their profiles as functions of time. This is useful to check if in their evolution there is any signature of the impact of the bar. I show the profiles in Figure 4.9.

The profile of z_{rms} (top left panel) increases in time over all the radial range. However, it is inside the first 5 kpc that the increase is larger. The initial value of z_{rms} inside the first few kpc is of ~ 270 pc (i.e. the initial disc scale height), but raises up to 550 pc at $t = 3.5$ Gyr. Since the bar dominates in these inner few kpc, and since the radial profile of z_{rms} shows otherwise less increase, the inner increase may be a direct effect of the bar. This indicates that the bar is able to thicken the disc by roughly the double its initial scale height. This seems to be also connected to the formation of the X-shape in the centre of the disc, that is
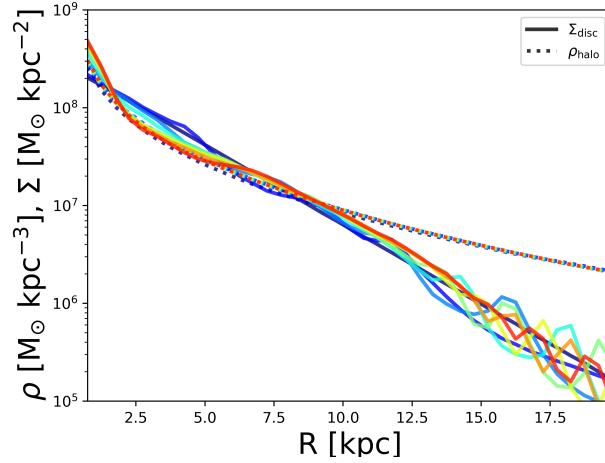
Figure 4.8: Evolution in time of the density profile of the MW disc and halo from the beginning of the simulation to $t = 3.5$ Gyr, with a a timestep of 0.5 Gyr. The full lines are for the disc surface density. The dotted lines are for the halo volume density. Colour codes as in Figure 4.7.
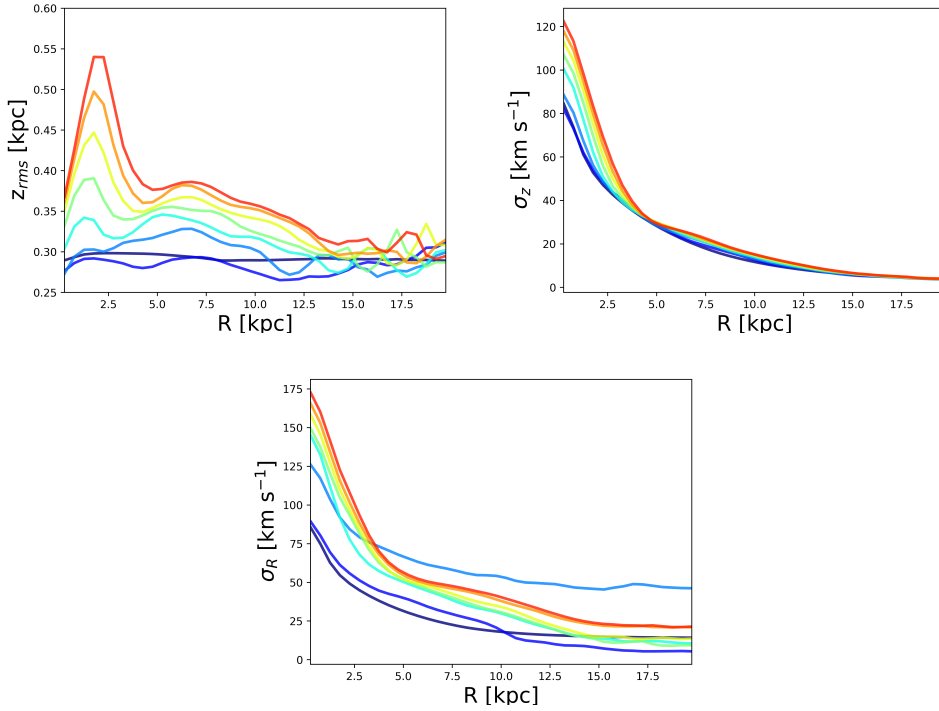
Figure 4.9: Radial profiles of the disc thickness z_{rms} (top left panel), vertical velocity dispersion σ_z (top right panel) and radial velocity dispersion σ_R (bottom panel) as functions of time, from $t = 0$ Gyr to $t = 3.5$ Gyr, with timestep of 0.5 Gyr. Colour codes as in Figure 4.7.

a visible feature in the xz- and yz-projected maps of Figure 4.4.

On the top right panel of Figure 4.9 I show the vertical velocity dispersion profile. It increases during the MW evolution, after $t = 0.5$ Gyr, to reach a peak of ~ 120 km s^{-1} in the inner MW at $t = 3.5$ Gyr. Thus, the presence of the bar

has the effect of heating the inner disc vertically. Instead, the outside regions of the disc are left mostly unchanged, showing only a small heating. The GCd for the change of behaviour is around 5 kpc, which is similar to the maximum value of bar length that I discussed in Figure 4.3. The overall picture points towards non negligible effects of the bar on the thickening and heating of the inner disc.

I now compare the results on disc thickening $\Delta z_{\mathrm{rms}} = z_{\mathrm{rms}}(2\,\mathrm{Gyr}) - z_{\mathrm{rms}}(0\,\mathrm{Gyr})$ and heating $\Delta\sigma_z^2 = \sigma_z^2(2\,\mathrm{Gyr}) - \sigma_z^2(0\,\mathrm{Gyr})$ with the ones for the isolated MW model shown in Figure 21 of **MJ16** (top and bottom panel, respectively). **MJ16** found that in 2 Gyr the values of z_{rms} increase on average of no more than $35 - 50$ pc within 15 kpc of GCd. Considering the scatter between their different simulations, they found that only in the outer disc there is a statistical increase that reaches $\Delta z_{\mathrm{rms}} \sim 70$ pc. Compared to these values, the inner increase of z_{rms} visible in the top left panel of Figure 4.9 is much higher in the centre of the disc. In fact, the final increase is of $\sim 90 - 100$ pc. Moving to the outer regions of the disc, however, the increase of z_{rms} is much more moderate in the case of this model, with no more than ~ 10 pc, even lower than the value of $\sim 50 - 70$ pc that **MJ16** found accounting for the scatter between their different simulations.

Regarding the vertical heating of the inner disc, at $t = 2$ Gyr the increase in σ_z^2 is of the order ~ 3800 km^2 s^{-2}. For comparison, the model of **MJ16** shows a final average increase of the inner σ_z^2 of only ~ 400 km^2 s^{-2}, or ~ 500 km^2 s^{-2} accounting for the statistical scatter between the simulations. This is much lower than our value. In the outer regions of the disc the increase is similar in the two models, of order ~ 20 km^2 s^{-2} for both cases.

To sum up, the bar thickens and heats up the inner disc in an efficient way with respect to an isolated MW model that does not develop bar instabilities. However, in the outer regions of the disc the effects are comparable in the two models and z_{rms} is even lower in our case than in the case of **MJ16**.

As an additional consideration, in the bottom panel of Figure 4.9 I show the radial profile of σ_R, and how it is affected by the bar in time. Again from this plot it is visible that there is a different evolution of the kinematics inside the bar and outside the bar: at the end of the simulation, σ_R increases of ~ 90 km s^{-1} inside the disc, while at $17.5 - 20.0$ kpc of GCd it increases only of ~ 20 km s^{-1}. At time $t = 1.0$ Gyr I note that the profile of σ_R shows a significantly higher momentary increase, that may be due to the ring-like density waves that propagate outwards during the evolution of the disc, and that are visible in the disc around that time (e.g. see the maps in Figure 4.4).

This analysis, including the comparison with the results on vertical thickening and heating in the isolated model of **MJ16**, shows that the impact of the bar on the disc kinematics is limited to its inner regions, while outside there are less visible effects. Also, it shows that the local impact on the kinematics does not invest only the vertical stellar motions but, as expected from the elongated orbits in the bar, also the radial stellar motions.
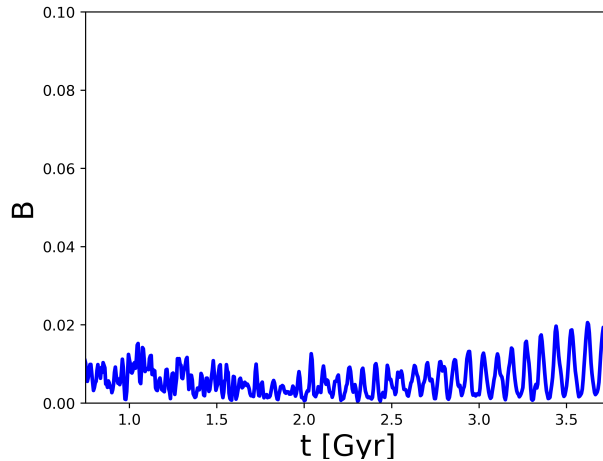
Figure 4.10: Bar buckling intensity B in our MW model as a function of time.

4.5   Buckling instability

Having calculated for each snapshot the bar phase angle Φ, I rotated all the disc particles by Φ, in order to have the x-axis now corresponding to the semi-major axis of the bar. I then calculated the bar buckling intensity B taking the magnitude of the Fourier coefficient of Equation (4.14) . I calculated B inside a parallelepipedic region around the bar in the xz-plane, accounting also for the bar thickness in the y- and z-directions, as explained in Martinez-Valpuesta et al. (2006) and in Section 4.1.4 of this thesis. The semi-thickness in the x-direction was set to 5 kpc to encapsulate the maximum bar length shown in Figure 4.3. The semi-thickness along the y- and z-directions was set to 1.5 kpc. This range is more conservative than the ranges -2 kpc $< y < 2$ kpc and $-\infty < z < \infty$ chosen by Martinez-Valpuesta et al. (2006), and it was chosen to exclude the contribution of particles out of the bar region.

The resulting evolution of B is shown in Figure 4.10 as a function of time. The time-evolution of B was smoothed like for the case of $A_{2,\mathrm{max}}$, i.e. for each snapshot the value of B was averaged together with the previous and subsequent ones.

The evolution of B in time shows that the bar buckling is almost negligible in this model. In fact we found that $B < 0.02$ at all times.

In Figure 5 of Martinez-Valpuesta et al. (2006) and in Figure 2 of Martinez-Valpuesta & Athanassoula (2008), the authors found always a first distinct, relevant peak of vertical buckling, of value $\sim 0.08 - 0.11$, followed by a second smaller, yet recognisable peak of value $\sim 0.03 - 0.04$. The rest of the signal is below ~ 0.01 and represents the noise regime, where no other relevant episode of buckling is found. For comparison, in the simulation discussed here I found that there is no distinct peak appearing in the profile of B, and that the values of buckling are always dominated by the noise regime, i.e. $B < 0.02$ almost at any time.

Additionally, I notice that after $t \sim 2$ Gyr, the pattern of B presents os-

cillations that appear with a periodicity of ~ 80 Myr. I checked for possible correlations of this periodicity with the rotational period of the bar. However, looking at values of the bar rotational periods in Table 4.2 for $t \geq 2$ Gyr, there is no systematic correlation with the oscillations in B (though after 2.5 Gyr the rotational period of the bar is around two times the oscillation period of the coefficient B) over all the time range $[2., 3.84]$ Gyr. To the present date, further investigation needs to be done to understand if, for instance, there is any connection of these oscillations in B with any other mechanism in the bar.

In conclusion, this MW model develops no sensible vertical buckling, that consequently is not expected to play any role in the evolution of the bar and of the surrounding MW disc. Given this result, there is an important implication on the origin of the X-shape of the MW bar, that I discuss in Section 4.6.

4.6   The X-shape in the bar

The bar present in this model develops a B/P feature, or X-shape feature. This is evident from a visual inspection of the xz- and yz-projections in the density maps of Figure 4.4. The X-shape rotates with the bar potential. After developing around $\sim 1.2 - 1.3$ Gyr, the X-shape increases its strength and survives for the subsequent ~ 2.7 Gyr, i.e. until the end of the simulation.

I first discuss the origin of the particles in the X-shape. At the snapshot corresponding to $t = 3.0$ Gyr, I rotated the coordinates by Φ to have the new x-axis corresponding to the direction of the bar semi-major axis. Then, I rotated the obtained coordinate frame by 45° in the new xz-plane (i.e. I estimated an inclination $\sim 45^\circ$ of the arms of the X-shape with respect to the Galactic plane, from visual inspection of the maps in Figure 4.4), so that the final x-axis and z-axis are aligned with the two arms of the X-shape.

In this rotated final coordinate frame I then selected a group of particles falling in the X-shape. In order to delimit the X-shape volume, I took a cross-shaped region with y-thickness 0.6 kpc centred on the xz-plane and with an extension of both arms from the GC (i.e. a semi-extension) equal to 1.5 kpc. Then, I traced these particles back using their unique IDs returned by the simulation, and I also checked their final distribution in the disc.

The result is shown in Figure 4.11, where from top to bottom I plot the xy-projections, the xz-projections and the yz-projections of the distribution of these selected particles at different times. For each projection, I show in the left panel the initial distribution of the particles and in the central panel the distribution of the particles in the X-shape at $t = 3$ Gyr. In the right panel, I show the final distribution of the same particles at $t = 3.84$ Gyr. This was done to check whether the particles persist orbiting inside the X-shape or if they just happen to cross the X-shape for a limited amount of time. The colours are used to distinguish particles originally belonging to different GCds (from blue to red means from smaller to higher initial GCds, respectively).

The first thing to notice is that all the particles selected inside the X-shape come originally from a range of radial extensions around the GC, distributed until $4 - 5$ kpc of GCd. Given that the bar length reaches at most $\sim 4 - 5$ kpc,
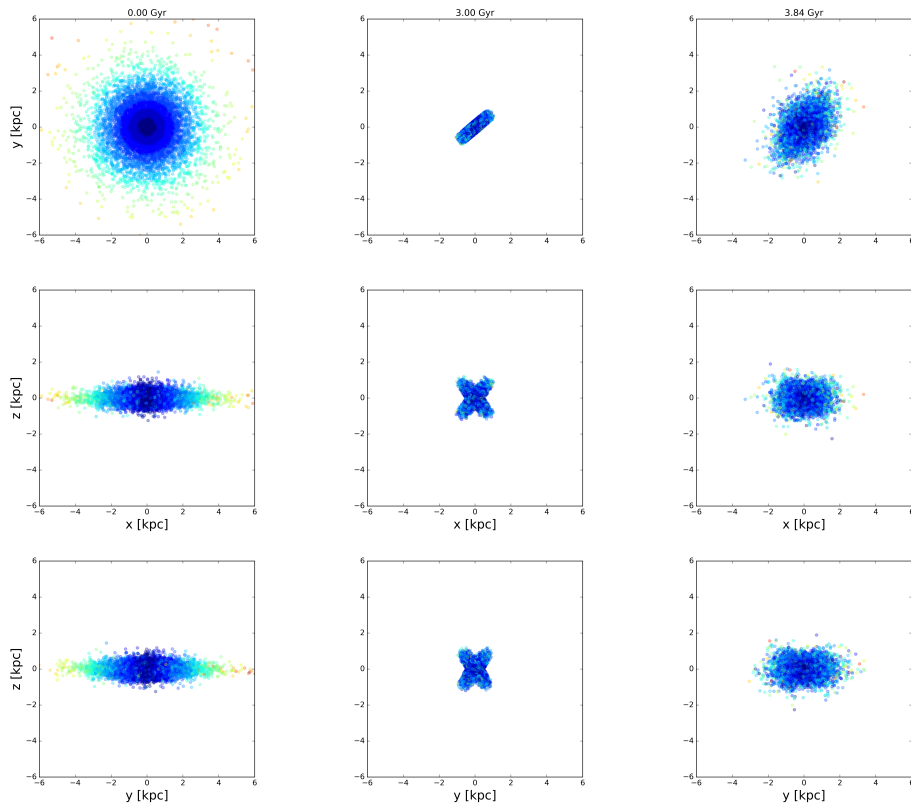
Figure 4.11: From top to bottom: xy-, xz- and yz-projections of the distribution of the particles that end in the X-shape at $t = 3$ Gyr. From left to right, particle distributions at $t = 0$, 3.0 and 3.84 Gyr. Colour codes, from blue to red, represent stars initially belonging to different GCds, going from smaller to larger GCds, in order.

then it is clear that these stars are the ones that contribute to the bar formation and to its orbits. Thus, the bar captures first the stars within 5 kpc of GCd and traps them into its orbits, shrinking their distribution to $2 - 3$ kpc of GCd at most. Later on, these particles are driven into resonant orbits that support the structure of the X-shape. Further investigation needs to be done on this model to determine which of the orbits discussed already in Section 1.5.1 are responsible for the formation of the X-shape.

The second thing to notice is that there is no systematic distribution of the selected stellar particles by initial GCd (i.e. by colour-code) in the X-shape. The orbits of the stellar particles enter the X-shape, mixing between themselves. Thus, the information about the original distribution of the particles is lost once their orbits enter the X-shape potential.

Last, from the right panels of Figure 4.11 it is evident that the particles are more spread than the X-shape volume at the end of the simulation. This is most likely a reflection of the fact that the orbits supporting the X-shape may be more extended than the volume that I adopted to sample the X-shape at $t = 3$ Gyr. If different orbits contribute to the X-shape, like the brezel and fish-brezel orbits, then since they have different $\Omega_x \colon \Omega_z$ ratios they can produce a mixed spatial distribution of the particles that populate them, explaining the mixed projection of these same particles in the right panels of Figure 4.11.

117
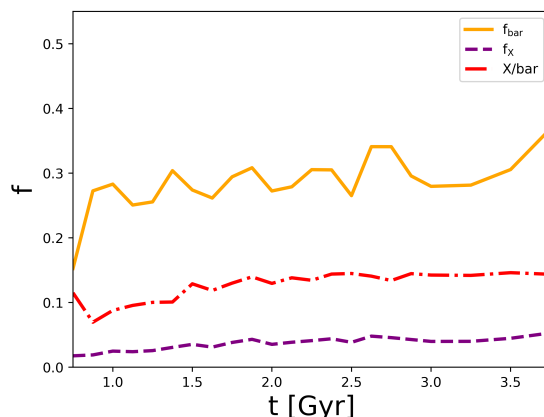
Figure 4.12: Evolution in time of the fraction of disc particles in the bar (full orange line), of the fraction of disc particles in the X-shape (dashed purple line) and of their relative ratio (dot-dashed red line).

In Figure 4.12 I show the fraction of disc particles ending in the bar, f_{bar}, the fraction of disc particles ending in the X-shape, f_X, and their relative ratio, as functions of time. In order to calculate the number of particles ending in the bar, I employed the same bar length data that I plotted in Figure 4.3, in order to define, at the corresponding snapshots, the rectangular regions with major length equal to two times the bar length and inside which all the particles are considered belonging to the bar. The semi-thickness in y and z assumed for the bar is again 1.5 kpc.

The results confirm that the bar mass grows in time (similarly to what I showed before from the analysis of $A_{2,\text{max}}$), and that the X-shape increases its total mass as well. The total mass of the bar is in the end $\sim 1.8 \times 10^{10}$ M$_\odot$, that is up to $\sim 40\%$ of the disc mass. However, the X-shape grows to a final mass of $\sim 2.5 \times 10^9$ M$_\odot$, i.e. no more than $\sim 5\%$ of the total disc mass. The X-shape is a much lighter feature in comparison with the bar. However, the ratio of the X-shape mass to the bar mass is going towards a final, constant value of ~ 0.13, after having slightly increased in time, thus indicating that in the final stages of the evolution of this MW model the X-shape grows proportionally to the bar. This result is in line with the proportional growth of the X-shape and the bar strength in in numerical simulations, reported by Athanassoula (2008).

4.6.1   Correlation of the X-shape with the buckling instability

We wanted to understand if there is any correlation between the development and growth of the X-shape, the growth of the bar, and its buckling instability. To do this, let us consider the results of Figure 4.12 in the light of the results on bar buckling from Figure 4.10. I briefly recall that in this simulation the buckling intensity B is always dominated by the noise regime or characterised by very small values, i.e. no sensible buckling develops in the bar.

In Figure 4.12 we can observe that, while not growing strongly, the X-shape increases its strength from $t = 0.5$ Gyr to the end of the simulation, in correla-

tion with the bar strength. Thus, in this Galactic model the X-shape does not correlate with any relevant buckling event, yet it grows in time.

This result is in line with what Quillen et al. (2014) stated for barred galaxies, i.e. that in general bar buckling is not the only process responsible for the formation of the X-shape. It also shows a different behaviour than the bar studied in Martinez-Valpuesta et al. (2006), where the second buckling episode was followed by the subsequent development of the X-shape. In the specific case of this model, that was built to match the observational properties of the MW, this brings to the conclusion that the buckling is not responsible for the formation of the X-shape in the MW.

Other mechanisms, such as the growth of resonant orbits in the bar potential, may be the cause of the formation of the X-shape in the MW. These mechanisms require further investigation in the context of this collaboration, before having conclusive results on this point.

4.7   Summary and remarks

In this chapter, I presented the results of a collaboration to study the properties of an N-body MW model that matches the observations of our Galaxy (**BHG16**), in order to address the problem of bar formation in the MW disc and of its impact on the local disc. I could determine that this full N-body MW model forms a bar and that the bar grows until it reaches more than a third of the MW disc mass.

This strong bar slows down in time, and this is expected in the light of what was discussed in Chapter 1 (and, for instance, also in D'Onghia & Aguerri 2020): the exchange of angular momentum of the bar with the MW components strengthens the bar and slows it down. This exchange of angular momentum is possible because of the presence of both an N-body DM halo and an N-body stellar disc in the simulation. The additional presence of a non-rotating bulge favours this mechanism. However, as D'Onghia & Aguerri (2020) stated, the fact that the bulge does not rotate is a limitation of the numerical set-up of this model, because it fastens the decrease of the bar pattern speed. The bar presented in this study would have reached a final pattern speed $\lesssim 40$ km s^{-1} on a larger timescale than $\sim 3 - 4$ Gyr if the bulge was rotating.

The bar strongly affects the inner MW disc kinematics and dynamics, provoking the divergence of the inner profiles of V_{circ} and tangential velocity. It also thickens and heats the inner disc in the vertical and radial directions.

The X-shape is most likely a consequence of the orbits developing in the rotating bar potential. The determination of these orbits requires more investigation, which is part of the next steps of the collaboration.

Last, the bar does not suffer any relevant event of vertical buckling. The X-shape grows almost in correlation with the bar strength, and is not correlated with any bar buckling. Therefore it is expected that the Galactic bar did not suffer any significant buckling in the past few Gyr of evolution.

Chapter 5

Thesis summary, final discussion, and future outlook

5.1   Summary of the research and final discussion

In this thesis I have explored a variety of N-body simulations of Galactic and stellar dynamics, in order to address the distribution of the MW satellite tidal debris in the Galactic environment and in order to study the properties of the bar in a model that matches to the observations of the Galaxy.

First, in Chapter 2, using high-resolution ICs from previous literature (**MJ16**), I investigated with a benchmark how different N-body codes reproduce the evolution of the MW in isolation and in interaction with its satellite galaxies, comparing also the accuracy and speed of these codes. I found that the family of GADGET codes has good candidates for running simulations of the MW environment, and that specifically GADGET-4 shows a good momentum conservation at an optimal computational speed.

Having chosen GADGET-4 as the best code, I employed it (Chapter 3) to explore the distribution of the satellite tidal debris in the MW environment, using the same high-resolution N-body MW models of **MJ16**, as well as realistic hybrid dwarf galaxy models (**M17**) placed in cosmologically motivated ICs (**MJ16**, Springel et al. 2008).

Within this realistic and cosmologically motivated framework, stars are found to be less stripped than DM from the satellites in the MW environment, where the stellar and DM debris distribute differently. Specifically, the stellar debris is more focused in the inner MW halo and has a different orientation than the DM debris within 25 kpc of GCd. The fact that tilting the disc impacts only weakly on the final distribution of the local debris points towards the importance of the satellites ICs in determining the final distribution of the local debris.

The last part of the research, described in Chapter 4, was a collaboration to use a high-resolution MW model (simulated by E. D'Onghia) that matches the observational constraints of our Galaxy and improves the MW models of **MJ16**, since it develops a bar, a feature that we observe in our Galaxy. In this simula-

tion the bar grows strongly, and towards the end it rotates slowly, with a final pattern speed below 40 km s^{-1} kpc^{-1}. The bar is dominant in terms of mass in the disc (more than $1/3$ of the disc mass) and presents no sign of relevant vertical buckling instabilities. Therefore, the X-shape that the bar develops is formed without the need of a vertical buckling.

The results presented in this thesis were obtained by means of N-body-only simulations, with SPH and stellar evolution recipes being switched off in the codes. However, the numerical set-up for the simulations of the MW satellite debris distribution described in Chapter 3 would have not been possible without recipes that distinguished stars from DM in the dwarf galaxies of **M17**.

As I mentioned at the end of Chapter 3, the fact that the DM and stellar debris have a different distribution and orientation in the MW environment means that it is not possible to track the distribution of the DM streams from the distribution of the observed stellar streams in the sky. While baryons are important to model the formation and evolution of structures in the Universe, if this different distribution of stellar and DM debris finds confirmation by future detections of DM in the MW halo, then the combination of realistic cosmological ICs (that include the effects of baryons on shaping structure formation and evolution until redhisft $z = 1$) and the solely gravitational interaction of the MW satellites with our Galaxy in the last few Gyr provide all the ingredients to model the distribution of the debris in the MW halo.

On the other hand, if including baryonic physics in the simulations of the satellite debris produces different results on the final distribution of the stellar and DM debris with respect to the N-body-only case, then future detections of DM are important to rule out one of the cases (negligible contribution or significant contribution of the baryonic physics in determining the local debris distribution). The argumentation presented in Section 3.1.3 already points towards neglecting the role of baryonic physics in shaping the local distribution of the debris at the current epoch, making it relevant only until $z \sim 1$. However, more investigation needs to be done on this point in the future.

The simulations presented in Chapter 3 and in Chapter 4 are N-body-only high-resolution simulations of the MW and its environment. As mentioned before in this thesis, one advantage of having N-body-only simulations with no cosmological integration is that all the computational effort can be spent in enhancing the resolution of the simulated galaxies to study in detail the evolution of their components. The other advantage is that these models can be initially set following specific observational constraints.

In this sense, the fact that the bar of the MW model studied in Chapter 4 has similar properties to the bars of models tailored to the observations of the MW or that reproduce the typical dynamics of MW-like galaxies (**P15**, Polyachenko et al. 2016; Abbott et al. 2017, among the works cited in this thesis), suggests that the approach of constructing ad-hoc MW models, even if with no cosmological ICs, is still valid in the scope of understanding the current and recent properties of our Galaxy.

Regarding the X-shape in the model of Chapter 4, the final value of the B/P

mass that we found is 2.5×10^9 M$_\odot$, a much lighter feature than the B/P mass from literature reported in Chapter 1. Thus, there are two possibilities: 1) the bar needs to increase more and the X-shape has not reached the final value of $\sim 1.2 - 1.6 \times 10^{10}$ M$_\odot$, or 2) we underestimated the mass in the X-shape of this model, e.g. due to the choice of too small volumes where to integrate the mass.

If case 1) is true, then more Gyr of simulation are needed, and the bar may have an age higher than 3.5 Gyr, going in favour of the age estimated by Cole & Weinberg (2002) rather than Polyachenko et al. (2016). However, if case 2) is true, then future work is needed to investigate the effects of increasing the estimated X-shape volume on the calculation of its mass, comparing our results with other mass calculation methods, like for instance the combination of unsharp masked images with the integration of B/P orbits as in Abbott et al. (2017).

5.2 Future outlook

Being the MW a rich environment, inclusive of many satellites, of their stripped debris that dissolves in the halo, and of a variety of other structures (e.g. bar and spirals in the Galactic disc), there is natural space for the prosecution and expansion of the projects described in this thesis.

As we mentioned in the conclusions to **MM20** , though our simulations of MW-satellites interaction have full N-body MW models that allow the natural inclusion of such effects like dynamical friction, other mechanisms like the secular growth of the disc and the halo, that are a consequence of the bottom-up formation process of galaxies like the MW, are missing in our description. There are available projects, like the already mentioned NIHAO of Wang et al. (2015), where many galaxies in a range of scales (from the mass of the MW, down to much smaller halo masses) are studied and described in detail, with the inclusion of their formation and evolution histories. A natural extension of the work presented in Chapter 3 could be using these MW-like models from Wang et al. (or from equivalent literature), extracting the information about the secular growth of their disc and of their halo, and simulating again the distribution of the tidally stripped satellite debris in the MW environment, this time with a MW time-evolving live potential.

The secular mass growth of the MW can be achieved by properly modifying the code (GADGET-4 in this case) to increase the disc and halo particle masses, at a pace determined by the MW accretion history extracted from Wang et al. or equivalent literature. The outcome of these simulations would allow to evaluate the long-term effects of the secular MW growth on the distribution of the satellite debris, in comparison with the results of Chapter 3, that were focused on studying the debris distribution in the last epochs only (i.e. $z \sim 0$).

As for the collaborative project on the MW model of Chapter 4, the results on the bar evolution show that there is a number of aspects that require further investigation. In fact, it is essential to understand which orbits and which resonant frequencies are at play in determining the formation of the X-shape. The

fact that recent literature is changing the view that x1 orbits are the main ones responsible for the formation of the X-shape in the MW bar (e.g. Pfenniger & Friedli 1991; Quillen et al. 2014) in favour of the view that a variety of orbits contribute to the formation of the X-shape (Portail et al. 2015b; Abbott et al. 2017) poses a challenge to our MW model. The analysis of the orbits inside the bar in our MW model can give a great help to validate the old view or the emerging, recent view about the contribution of the different orbits. This is important for our understanding of the stellar dynamics behind the formation of the Galactic B/P bulge.

Additionally, the study of the frequencies characterising the stellar orbits in the bar of this model may be of help to understand the interplay between the bar and other disc features. This could offer a more complete answer to the oscillations in the radius of maximum A_2, in the bar speed, and in the corotation radius.

Last, the availability of the MW high-resolution model of Chapter 4, that describes the formation of a strong bar, could represent the base for the next step in the study of the distribution of the satellite debris in the MW. Repeating one of the simulations described in Chapter 3 with this bar-forming MW model in place of the MW models of **MJ16**, and with the same initial positions and velocities of the hybrid satellites of **M17** as described in **MM20**, will allow to investigate whether the presence of the bar potential in the MW disc can impact the distribution and orientation of the stellar and DM debris.

Being its mass a third of the total disc stellar mass, all concentrated in a small region (within ~ 5 kpc of GCd), the bar can potentially change the distribution of the local debris. The outcome of this analysis may be compared to the results on the debris distribution in presence of a growing MW potential, to determine which of the two processes (bar formation or secular growth of the MW potential) is impacting the most on the debris distribution, and to compare the effects of the two processes.

Acknowledgements

Bibliography

Abbott C. G., Valluri M., Shen J., Debattista V. P., 2017, MNRAS, 470, 1526

Abolfathi B., et al., 2018, Astrophysical Journal Supplement, 235, 42

Aguerri J. A. L., Muñoz-Tuñón C., Varela A. M., Prieto M., 2000, Astronomy and Astrophysics, 361, 841

Ahn C. P., et al., 2012, Astrophysical Journal Supplement, 203, 21

Alcock C., et al., 1995, The Astrophysical Journal, 445, 133

Allgood B., Flores R. A., Primack J. R., Kravtsov A. V., Wechsler R. H., Faltenbacher A., Bullock J. S., 2006, MNRAS, 367, 1781

Amôres E. B., López-Corredoira M., González-Fernández C., Moitinho A., Minniti D., Gurovich S., 2013, Astronomy and Astrophysics, 559, A11

Appel A. W., 1985, SIAM Journal on Scientific and Statistical Computing, 6, 85

Athanassoula E., 2002, The Astrophysical Journal Letters, 569, L83

Athanassoula E., 2003, MNRAS, 341, 1179

Athanassoula E., 2008, Astrophysics and Space Science Proceedings, 4, 47

Athanassoula E., Martinez-Valpuesta I., 2009, Astrophysics and Space Science Proceedings, 8, 77

Athanassoula E., Fady E., Lambert J. C., Bosma A., 2000, MNRAS, 314, 475

Barnes J., Hut P., 1986, Nature, 324, 446

Barnes J. E., Hut P., 1989, Astrophysical Journal Supplement, 70, 389

Bechtol K., et al., 2015, The Astrophysical Journal, 807, 50

Belokurov V., et al., 2006, The Astrophysical Journal Letters, 642, L137

Bennett C. L., et al., 2003a, The Astrophysical Journal Supplement Series, 148, 1

Bennett C. L., et al., 2003b, The Astrophysical Journal, 583, 1

Berger M. J., Colella P., 1989, Journal of Computational Physics, 82, 64

Berger M. J., Oliger J., 1984, Journal of Computational Physics, 53, 484

Besla G., Martínez-Delgado D., van der Marel R. P., Beletsky Y., Seibert M., Schlafly E. F., Grebel E. K., Neyer F., 2016, The Astrophysical Journal, 825, 20

Bien R., Brandt T., Just A., 2013, MNRAS, 428, 1631

Binney J., Tremaine S., 2008, Galactic Dynamics: Second Edition. Princeton: Princeton University Press

Bland-Hawthorn J., Gerhard O., 2016, Annual Review of Astronomy and Astrophysics, 54, 529

Blitz L., Spergel D. N., 1991, The Astrophysical Journal, 379, 631

Blumenthal G. R., Faber S. M., Primack J. R., Rees M. J., 1984, Nature, 311, 517

Boggess N. W., et al., 1992, The Astrophysical Journal, 397, 420

Bovy J., 2017, MNRAS, 468, L63

Boylan-Kolchin M., Bullock J. S., Kaplinghat M., 2011, MNRAS, 415, L40

Bromm V., Coppi P. S., Larson R. B., 1999, The Astrophysical Journal Letters, 527, L5

Brooks A. M., Kuhlen M., Zolotov A., Hooper D., 2013, The Astrophysical Journal, 765, 22

Buck T., Dutton A. A., Macciò A. V., 2016, MNRAS, 460, 4348

Buck T., Macciò A. V., Dutton A. A., Obreja A., Frings J., 2019, MNRAS, 483, 1314

Bullock J. S., Johnston K. V., 2005, The Astrophysical Journal, 635, 931

Bullock J. S., Kravtsov A. V., Weinberg D. H., 2000, The Astrophysical Journal, 539, 517

Burton W. B., Gordon M. A., 1978, Astronomy and Astrophysics, 63, 7

Camarillo T., Mathur V., Mitchell T., Ratra B., 2018, Publications of the Astronomical Society of the Pacific, 130, 024101

Capuzzo-Dolcetta R., Spera M., Punzo D., 2013, Journal of Computational Physics, 236, 580

Cervantes-Cota J. L., Smoot G., 2011, AIP Conference Proceedings, 1396, 28

Chandrasekhar S., 1943, The Astrophysical Journal, 97, 255

Christensen C., Quinn T., Governato F., Stilp A., Shen S., Wadsley J., 2012, MNRAS, 425, 3058

Cole A. A., Weinberg M. D., 2002, The Astrophysical Journal Letters, 574, L43

Cui X.-Q., et al., 2012, Research in Astronomy and Astrophysics, 12, 1197

Curtis H. D., 1917, Publications of the Astronomical Society of the Pacific, 29, 206

D'Onghia E., Aguerri J. A. L., 2020, The Astrophysical Journal, 890, 117

D'Onghia E., Fox A. J., 2016, Annual Review of Astronomy and Astrophysics, 54, 363

Davis M., Efstathiou G., Frenk C. S., White S. D. M., 1985, The Astrophysical Journal, 292, 371

De Bernardis P., et al., 2000, Nature, 404, 955

Deason A. J., Mao Y.-Y., Wechsler R. H., 2016, The Astrophysical Journal, 821, 5

Deason A. J., Belokurov V., Sanders J. L., 2019, MNRAS, 490, 3426

Debattista V. P., Sellwood J. A., 2000, The Astrophysical Journal, 543, 704

Debattista V. P., Gerhard O., Sevenster M. N., 2002, MNRAS, 334, 355

Dehnen W., 2000, The Astrophysical Journal Letters, 536, L39

Diaz J., Bekki K., 2011, MNRAS, 413, 2015

Dicke R. H., Peebles P. J. E., Roll P. G., Wilkinson D. T., 1965, The Astrophysical Journal, 142, 414

Diemand J., Kuhlen M., Madau P., Zemp M., Moore B., Potter D., Stadel J., 2008, Nature, 454, 735

Djorgovski S., Davis M., 1987, The Astrophysical Journal, 313, 59

Draine B., 2003, Annual Review of Astronomy and Astrophysics, 41, 241

Drlica-Wagner A., et al., 2015, The Astrophysical Journal, 813, 109

Durier F., Dalla Vecchia C., 2012, MNRAS, 419, 465

Efstathiou G., Gratton S., 2020, MNRAS, 496, L91

Eilers A.-C., Hogg D. W., Rix H.-W., Ness M. K., 2019, The Astrophysical Journal, 871, 120

Einstein A., 1915, Sitzungsberichte der Königlich Preußischen Akademie der Wissenschaften (Berlin), pp 844–847

Englmaier P., Gerhard O., 1999, MNRAS, 304, 512

Ernst A., Just A., 2013, MNRAS, 429, 2953

Errani R., Peñarrubia J., Walker M. G., 2018, MNRAS, 481, 5073

Faber S. M., Lin D. N. C., 1983, The Astrophysical Journal Letters, 266, L17

Fellhauer M., Kroupa P., Baumgardt H., Bien R., Boily C. M., Spurzem R., Wassmer N., 2000, New Astronomy, 5, 305

Feng J. L., 2010, Annual Review of Astronomy and Astrophysics, 48, 495

Freeman K. C., 1970, The Astrophysical Journal, 160, 811

Friedmann A., 1922, Zeitschrift fur Physik, 10, 377

Frieman J. A., Turner M. S., Huterer D., 2008, Annual Review of Astronomy and Astrophysics, 46, 385

Frings J., Macciò A., Buck T., Penzo C., Dutton A., Blank M., Obreja A., 2017, MNRAS, 472, 3378

GRAVITY Collaboration et al., 2018, A&A, 615, L15

Gaia Collaboration et al., 2018, Astronomy and Astrophysics, 616, A1

Garrison-Kimmel S., et al., 2017, MNRAS, 471, 1709

Genel S., Genzel R., Bouché N., Naab T., Sternberg A., 2009, The Astrophysical Journal, 701, 2002

Genel S., et al., 2014, MNRAS, 445, 175

Gerhard O., 2002, in Da Costa G. S., Sadler E. M., Jerjen H., eds, Astronomical Society of the Pacific Conference Series Vol. 273, The Dynamics, Structure & History of Galaxies: A Workshop in Honour of Professor Ken Freeman. p. 73 (arXiv:astro-ph/0203109)

Gerhard O., Wegg C., 2015, in Freeman K., Elmegreen B., Block D., Woolway M., eds, Lessons from the Local Group: A Conference in honor of David Block and Bruce Elmegreen. Springer, Cham, p. 43, doi:10.1007/978-3-319-10614-4_4

Gillessen S., Eisenhauer F., Fritz T. K., Pfuhl O., Ott T., Genzel R., 2013, in de Grijs R., ed., IAU Symposium Vol. 289, Advancing the Physics of Cosmic Distances. pp 29–35, doi:10.1017/S1743921312021060

Gilmore G., Reid N., 1983, MNRAS, 202, 1025

Gingold R. A., Monaghan J. J., 1977, MNRAS, 181, 375

Graczyk D., et al., 2014, The Astrophysical Journal, 780, 59

Grand R. J. J., et al., 2017, MNRAS, 467, 179

Grebel E. K., Gallagher III J. S., Harbeck D., 2003, Astronomical Journal, 125, 1926

Greengard L., Rokhlin V., 1997, Journal of Computational Physics, 135, 280

Griv E., Gedalin M., Jiang I.-G., 2019, MNRAS, 484, 218

Guedes J., Callegari S., Madau P., Mayer L., 2011, The Astrophysical Journal, 742, 76

Helmi A., White S. D. M., de Zeeuw P. T., Zhao H., 1999, Nature, 402, 53

Helmi A., Babusiaux C., Koppelman H. H., Massari D., Veljanoski J., Brown A. G. A., 2018, Nature, 563, 85

Hernquist L., 1990, The Astrophysical Journal, 356, 359

Hernquist L., Katz N., 1989, Astrophysical Journal Supplement, 70, 419

Herschel W., 1785, On the Construction of the Heavens. By William Herschel, Esq. F. R. S.. Vol. 75, The Royal Society, https://royalsocietypublishing.org/doi/10.1098/rstl.1785.0012

Hilmi T., et al., 2020, MNRAS, 497, 933

Hinshaw G., et al., 2013, Astrophysical Journal Supplement, 208, 19

Holmberg J., Nordström B., Andersen J., 2009, Astronomy and Astrophysics, 501, 941

Hopkins P. F., 2013, Pressure-Entropy SPH: Pressure-entropy smooth-particle hydrodynamics (ascl:1305.006)

Hubble E., 1929a, Proceedings of the National Academy of Science, 15, 168

Hubble E. P., 1929b, The Astrophysical Journal, 69, 103

Ibata R. A., Gilmore G., Irwin M. J., 1994, Nature, 370, 194

Jeans J. H., 1902, Philosophical Transactions of the Royal Society of London Series A, 199, 1

Jetley P., Gioachin F., Mendes C., Kale L. V., Quinn T., 2008, in 2008 IEEE International Symposium on Parallel and Distributed Processing. pp 1–12, doi:10.1109/IPDPS.2008.4536319

Jetley P., Wesolowski L., Gioachin F., Kalé L. V., Quinn T. R., 2010, in SC '10: Proceedings of the 2010 ACM/IEEE International Conference for High Performance Computing, Networking, Storage and Analysis. pp 1–11, doi:10.1109/SC.2010.49

Jurić M., et al., 2008, The Astrophysical Journal, 673, 864

Just A., Jahreiß H., 2010, MNRAS, 402, 461

Kalberla P. M., Kerp J., 2009, Annual Review of Astronomy and Astrophysics, 47, 27

Kapteyn J. C., 1922, The Astrophysical Journal, 55, 302

Katz N., 1992, The Astrophysical Journal, 391, 502

Katz N., Weinberg D. H., Hernquist L., 1996, Astrophysical Journal Supplement, 105, 19

Keller B. W., Wadsley J., Benincasa S. M., Couchman H. M. P., 2014, MNRAS, 442, 3013

Kennicutt Jr. R. C., 1998, Annual Review of Astronomy and Astrophysics, 36, 189

Kent S. M., 1986, Astronomical Journal, 91, 1301

Kihara T., Sakai K., 1970, Publications of the Astronomical Society of Japan, 22, 1

King I. R., 1966, Astronomical Journal, 71, 64

Kirby E. N., Cohen J. G., Guhathakurta P., Cheng L., Bullock J. S., Gallazzi A., 2013, The Astrophysical Journal, 779, 102

Klypin A., Kravtsov A. V., Valenzuela O., Prada F., 1999, The Astrophysical Journal, 522, 82

Komatsu E., et al., 2011, Astrophysical Journal Supplement, 192, 18

Koppelman H. H., Helmi A., Massari D., Roelenga S., Bastian U., 2019, Astronomy and Astrophysics, 625, A5

Kormendy J., Ho L. C., 2013, Annual Review of Astronomy and Astrophysics, 51, 511

Kuijken K., 1996, in Buta R., Crocker D. A., Elmegreen B. G., eds, Astronomical Society of the Pacific Conference Series Vol. 91, IAU Colloq. 157: Barred Galaxies. p. 504 (arXiv:astro-ph/9508132)

Kunder A., et al., 2012, Astronomical Journal, 143, 57

Kunder A., et al., 2017, Astronomical Journal, 153, 75

Landau L. D., Lifshitz E. M., 1987, Fluid Mechanics. Second Edition. Pergamon, Oxford

Lemaître G., 1927, Annales de la Société Scientifique de Bruxelles, 47, 49

Li Z.-Y., Shen J., 2012, The Astrophysical Journal Letters, 757, L7

Li T. S., et al., 2018, The Astrophysical Journal, 857, 145

Liddle A., 2003, An introduction to modern cosmology; 2nd ed.. Wiley, Chichester

Lisanti M., Spergel D. N., 2012, Physics of the Dark Universe, 1, 155

Łokas E. L., 2019, Astronomy and Astrophysics, 629, A52

Long R. J., Mao S., Shen J., Wang Y., 2012, MNRAS, 428, 3478

Lora V., Grebel E. K., Sánchez-Salcedo F. J., Just A., 2013, The Astrophysical Journal, 777, 65

Lucy L. B., 1977, Astronomical Journal, 82, 1013

Lütticke R., Dettmar R. J., Pohlen M., 2000, Astronomy and Astrophysics, 362, 435

Macciò A. V., Kang X., Fontanot F., Somerville R. S., Koposov S., Monaco P., 2010, MNRAS, 402, 1995

Macciò A. V., Frings J., Buck T., Penzo C., Dutton A. A., Blank M., Obreja A., 2017, MNRAS, 472, 2356

Marrese P. M., Marinoni S., Fabrizio M., Altavilla G., 2019, Astronomy and Astrophysics, 621, A144

Martínez-Delgado D., Gómez-Flechoso M. Á., Aparicio A., Carrera R., 2004, The Astrophysical Journal, 601, 242

Martinez-Valpuesta I., Athanassoula E., 2008, in Bureau M., Athanassoula E., Barbuy B., eds, IAU Symposium Vol. 245, Formation and Evolution of Galaxy Bulges. pp 103–106 (`arXiv:0710.4054`), doi:10.1017/S1743921308017390

Martinez-Valpuesta I., Gerhard O., 2011, The Astrophysical Journal Letters, 734, L20

Martinez-Valpuesta I., Shlosman I., Heller C., 2006, The Astrophysical Journal, 637, 214

Mathewson D. S., Cleary M. N., Murray J. D., 1974, The Astrophysical Journal, 190, 291

Matsumoto T., Hayakawa S., Koizumi H., Murakami H., Uyama K., Yamagami T., Thomas J. A., 1982, in Riegler G. R., Blandford R. D., eds, American Institute of Physics Conference Series Vol. 83, The Galactic Center. pp 48–52, doi:10.1063/1.33493

Mazzarini M., Just A., Macciò A. V., Moetazedian R., 2020, Astronomy and Astrophysics, 636, A106

McConnachie A. W., 2012, Astronomical Journal, 144, 4

McWilliam A., Zoccali M., 2010, The Astrophysical Journal, 724, 1491

Menon H., Wesolowski L., Zheng G., Jetley P., Kale L., Quinn T., Governato F., 2015, Computational Astrophysics and Cosmology, 2, 1

Mihos J. C., Hernquist L., 1996, The Astrophysical Journal, 464, 641

Misner C. W., Thorne K. S., Wheeler J. A., 1973, Gravitation. San Francisco: W.H. Freeman and Co.

Moetazedian R., Just A., 2016, MNRAS, 459, 2905

Monaghan J. J., 1992, Annual Review of Astronomy and Astrophysics, 30, 543

Monaghan J. J., Lattanzio J. C., 1985, Astronomy and Astrophysics, 149, 135

Mróz P., et al., 2019, The Astrophysical Journal Letters, 870, L10

Nataf D. M., Udalski A., Gould A., Fouqué P., Stanek K. Z., 2010, The Astrophysical Journal Letters, 721, L28

Navarro J. F., Frenk C. S., White S. D. M., 1995a, MNRAS, 275, 56

Navarro J. F., Frenk C. S., White S. D. M., 1995b, MNRAS, 275, 720

Navarro J. F., Frenk C. S., White S. D. M., 1996, The Astrophysical Journal, 462, 563

Nelson D., et al., 2019, MNRAS, 490, 3234

Newberg H. J., et al., 2002, The Astrophysical Journal, 569, 245

Newberg H. J., Yanny B., Cole N., Beers T. C., Re Fiorentin P., Schneider D. P., Wilhelm R., 2007, The Astrophysical Journal, 668, 221

Newton O., Cautun M., Jenkins A., Frenk C. S., Helly J. C., 2018, MNRAS, 479, 2853

Nidever D. L., Majewski S. R., Butler Burton W., Nigra L., 2010, The Astrophysical Journal, 723, 1618

Nitadori K., Makino J., 2008, New Astronomy, 13, 498

Oort J. H., 1927, Bulletin of the Astronomical Institutes of the Netherlands, 3, 275

Palicio P. A., et al., 2018, MNRAS, 478, 1231

Pawlowski M. S., Pflamm-Altenburg J., Kroupa P., 2012, MNRAS, 423, 1109

Peñarrubia J., Navarro J. F., McConnachie A. W., 2008, The Astrophysical Journal, 673, 226

Penzias A. A., Wilson R. W., 1965, The Astrophysical Journal, 142, 419

Perlmutter S., et al., 1999, The Astrophysical Journal, 517, 565

Pfenniger D., Friedli D., 1991, Astronomy and Astrophysics, 252, 75

Pietrzyński G., et al., 2013, Nature, 495, 76

Pillepich A., Madau P., Mayer L., 2015, The Astrophysical Journal, 799, 184

Pillepich A., et al., 2019, MNRAS, 490, 3196

Planck Collaboration et al., 2018, arXiv e-prints, p. arXiv:1807.06209

Polyachenko E. V., Berczik P., Just A., 2016, MNRAS, 462, 3727

Pontzen A., Governato F., 2012, MNRAS, 421, 3464

Portail M., Wegg C., Gerhard O., Martinez-Valpuesta I., 2015a, MNRAS, 448, 713

Portail M., Wegg C., Gerhard O., 2015b, MNRAS, 450, L66

Power C., Navarro J. F., Jenkins A., Frenk C. S., White S. D. M., Springel V., Stadel J., Quinn T., 2003, MNRAS, 338, 14

Quillen A. C., Minchev I., Sharma S., Qin Y.-J., Di Matteo P., 2014, MNRAS, 437, 1284

Quinn T., Katz N., Stadel J., Lake G., 1997, arXiv e-prints, pp astro–ph/9710043

Rich R. M., Reitzel D. B., Howard C. D., Zhao H., 2007, The Astrophysical Journal Letters, 658, L29

Riess A. G., et al., 1998, Astronomical Journal, 116, 1009

Rix H.-W., Bovy J., 2013, The Astronomy and Astrophysics Review, 21, 61

Robertson H. P., 1927, Transactions of the American Mathematical Society, 29, 481

Rodriguez-Fernandez N. J., Combes F., 2008, Astronomy and Astrophysics, 489, 115

Romero-Gómez M., Athanassoula E., Antoja T., Figueras F., 2011, MNRAS, 418, 1176

Rubin V. C., Ford W. Kent J., 1970, The Astrophysical Journal, 159, 379

Rubin V. C., Ford W. K. J., Thonnard N., 1980, The Astrophysical Journal, 238, 471

Ryden B., 2003, Introduction to cosmology. San Francisco :Addison-Wesley

Saadeh D., Feeney S. M., Pontzen A., Peiris H. V., McEwen J. D., 2016, Physical Review Letters, 117, 131302

Santos-Santos I. M., Domínguez-Tenreiro R., Pawlowski M. S., 2019, arXiv e-prints, p. arXiv:1908.02298

Sawala T., et al., 2016, MNRAS, 457, 1931

Sawala T., Pihajoki P., Johansson P. H., Frenk C. S., Navarro J. F., Oman K. A., White S. D. M., 2017, MNRAS, 467, 4383

Schwarzschild M., 1979, The Astrophysical Journal, 232, 236

Scoccimarro R., Frieman J., 1996, Astrophysical Journal Supplement, 105, 37

Seager S., Sasselov D. D., Scott D., 2000, Astrophysical Journal Supplement, 128, 407

Shen S., Wadsley J., Stinson G., 2010, MNRAS, 407, 1581

Sijacki D., Vogelsberger M., Genel S., Springel V., Torrey P., Snyder G. F., Nelson D., Hernquist L., 2015, MNRAS, 452, 575

Silk J., 1968, The Astrophysical Journal, 151, 459

Silk J., 2003, MNRAS, 343, 249

Simon J. D., 2019, Annual Review of Astronomy and Astrophysics, 57, 375

Simpson C. M., Grand R. J. J., Gómez F. A., Marinacci F., Pakmor R., Springel V., Campbell D. J. R., Frenk C. S., 2018, MNRAS, 478, 548

Slipher V. M., 1913, Lowell Observatory Bulletin, 1, 56

Sofue Y., Honma M., Omodaka T., 2009, Publications of the Astronomical Society of Japan, 61, 227

Springel V., 2005, MNRAS, 364, 1105

Springel V., 2010a, Annual Review of Astronomy and Astrophysics, 48, 391

Springel V., 2010b, MNRAS, 401, 791

Springel V., Hernquist L., 2002, MNRAS, 333, 649

Springel V., Hernquist L., 2003, MNRAS, 339, 289

Springel V., Yoshida N., White S. D. M., 2001, New Astronomy, 6, 79

Springel V., Di Matteo T., Hernquist L., 2005a, MNRAS, 361, 776

Springel V., et al., 2005b, Nature, 435, 629

Springel V., et al., 2008, MNRAS, 391, 1685

Stadel J. G., 2001, PhD thesis, University of Washington, Seattle, WA, USA

Stanek K. Z., Mateo M., Udalski A., Szymanski M., Kaluzny J., Kubiak M., 1994, The Astrophysical Journal Letters, 429, L73

Stanek K. Z., Udalski A., SzymaŃski M., KaŁuŻny J., Kubiak Z. M., Mateo M., KrzemiŃski W., 1997, The Astrophysical Journal, 477, 163

Stinson G., Seth A., Katz N., Wadsley J., Governato F., Quinn T., 2006, MNRAS, 373, 1074

Sutherland R. S., Dopita M. A., 1993, Astrophysical Journal Supplement, 88, 253

Tasker E. J., Brunino R., Mitchell N. L., Michielsen D., Hopton S., Pearce F. R., Bryan G. L., Theuns T., 2008, MNRAS, 390, 1267

The GRAVITY Collaboration et al., 2019, A&A, 625, L10

Tomozeiu M., Mayer L., Quinn T., 2016, The Astrophysical Journal, 827, L15

Toomre A., 1964, The Astrophysical Journal, 139, 1217

Torrealba G., Koposov S. E., Belokurov V., Irwin M., 2016, MNRAS, 459, 2370

Torrealba G., et al., 2018, MNRAS, 475, 5085

Vogelsberger M., et al., 2014a, MNRAS, 444, 1518

Vogelsberger M., et al., 2014b, Nature, 509, 177

Wadsley J. W., Stadel J., Quinn T., 2004, New Astronomy, 9, 137

Wadsley J. W., Veeravalli G., Couchman H. M. P., 2008, MNRAS, 387, 427

Wadsley J. W., Keller B. W., Quinn T. R., 2017, MNRAS, 471, 2357

Wang L., Dutton A. A., Stinson G. S., Macciò A. V., Penzo C., Kang X., Keller B. W., Wadsley J., 2015, MNRAS, 454, 83

Wang J., Hammer F., Yang Y., Ripepi V., Cioni M.-R. L., Puech M., Flores H., 2019, MNRAS,

Wannier P., Wrixon G. T., 1972, The Astrophysical Journal Letters, 173, L119

Wegg C., Gerhard O., 2013a, The Messenger, 154, 54

Wegg C., Gerhard O., 2013b, MNRAS, 435, 1874

Wegg C., Gerhard O., Portail M., 2015, MNRAS, 450, 4050

Weiland J. L., et al., 1994, The Astrophysical Journal Letters, 425, L81

Weisz D. R., Dolphin A. E., Skillman E. D., Holtzman J., Gilbert K. M., Dalcanton J. J., Williams B. F., 2014, The Astrophysical Journal, 789, 147

Wetzel A. R., Hopkins P. F., Kim J.-h., Faucher-Giguère C.-A., Kereš D., Quataert E., 2016, The Astrophysical Journal Letters, 827, L23

White M., 2014, MNRAS, 439, 3630

White S. D. M., Rees M. J., 1978, MNRAS, 183, 341

Wilson J. C., et al., 2010, in McLean I. S., Ramsay S. K., Takami H., eds, Vol. 7735, Ground-based and Airborne Instrumentation for Astronomy III. SPIE, pp 554 – 567, doi:10.1117/12.856708

Wright E. L., 2006, Publications of the Astronomical Society of the Pacific, 118, 1711

Wyse R. F. G., 2009, in Mamajek E. E., Soderblom D. R., Wyse R. F. G., eds, IAU Symposium Vol. 258, The Ages of Stars. pp 11–22 (arXiv:0907.0415), doi:10.1017/S1743921309031664

Yadav J. K., Bagla J. S., Khandai N., 2010, MNRAS, 405, 2009

Yoshida N., Abel T., Hernquist L., Sugiyama N., 2003, The Astrophysical Journal, 592, 645

Yurin D., Springel V., 2014, MNRAS, 444, 62

Zel'Dovich Y. B., 1970, Astronomy and Astrophysics, 500, 13

Zoccali M., Cassisi S., Frogel J. A., Gould A., Ortolani S., Renzini A., Rich R. M., Stephens A. W., 2000, The Astrophysical Journal, 530, 418

Zolotov A., et al., 2012, The Astrophysical Journal, 761, 71